New Approaches to Modeling Statistics of the Large-scale Structure in the Universe

by

Nuala McCullagh

A dissertation submitted to The Johns Hopkins University in conformity with the requirements for the degree of Doctor of Philosophy.

Baltimore, Maryland

May, 2014

Abstract

The spatial distribution of matter in the universe is a powerful probe of cosmology due in large part to the Baryon Acoustic Oscillation (BAO) feature in the 2-point correlation function, which provides a standard ruler that allows us to measure the properties of dark energy. Current and future galaxy surveys promise to deliver vast amounts of data and systematic errors will become dominant over statistical errors in determining cosmological parameters from galaxy surveys. Accurate theoretical models of systematics such as nonlinear gravitational evolution and redshift-space distortions are necessary to extract cosmological information from the statistics of large-scale structure.

First, we present a configuration-space approach to perturbation theory. We show how this can be used to calculate the nonlinear contribution to the 2-point correlation function, and verify the result both analytically and numerically. We then extend this approach to include the effects of redshift-space distortions. Our results indicate that a configuration-space approach to perturbation theory simplifies the mathematics of the nonlinear and redshift-space statistics of the matter distribution.

ABSTRACT

Next, we consider the effects of density transformations on the bias of the BAO peak in the 2-point correlation function. Using configuration-space perturbation theory, we model the nonlinear correlation functions of various transformed fields and find that a logarithmic transform, which results in a more Gaussian distribution, provides a less biased peak position at low redshift. Such a transform could improve constraints on dark energy parameters.

Because the nonlinear density field is non-Gaussian, information resides in higher-point statistics of the distribution. The 3-point statistics of the galaxy density field contain information about inflation, structure formation, and galaxy bias. Extracting this information requires accurate modeling of nonlinearity and redshift-space distortions. We discuss the challenges associated with theoretical and numerical modeling of the bispectrum on nonlinear scales, and test current models in various regimes. We then show how a configuration-space approach can be used to model the redshift-space 3-point correlation function in a simple way.

By modeling nonlinearity and redshift-space distortions in the statistics of the matter distribution we can better constrain cosmological parameters from galaxy surveys.

Primary Reader: Alexander S. Szalay

Secondary Reader: Marc Kamionkowski

Acknowledgments

This thesis would not have been possible without the guidance of my advisor, Alexander S. Szalay. I feel very lucky to have had the opportunity to work with him. His wisdom, enthusiasm, and encouragement have been essential to my development as a scientist. I am also grateful to Marc Kamionkowski for being an excellent teacher and for allowing me to crash his group meetings. His curiosity and insights have inspired me to ask more questions. I am thankful to my thesis advisory committee members, Rosemary Wyse and Brice Ménard, for keeping me on track these past few years. I have also greatly benefitted from interactions with my collaborators: Donghui Jeong, Mark Neyrinck, István Szapudi, and Bridget Falck. Their guidance and intuition have helped shape my understanding of cosmology.

I am very grateful to my friends at JHU, particularly Nikolaus Hartman and Daniel Allan, with whom I have spent countless hours doing physics homework, discussing research, eating lunch, and drinking beer. My time at JHU would not have been nearly as fun without them.

I am eternally indebted to my parents, Rosa and Peter McCullagh, and to my

siblings, Emma, Martin, and Ellen, for always making time to help me and for never letting me doubt myself.

Finally, I am extremely thankful to my fiancé, Stefan Byrd-Krueger, whose endless patience and encouragement have kept me going throughout this process.

Dedication

This thesis is dedicated to my parents, Rosa and Peter McCullagh.

Contents

List of Figures

Chapter 1

Introduction

Cosmologists strive to answer the most fundamental questions about the universe: how did the universe begin? how did it evolve to its present form? is the universe spatially flat, or is it curved? what is the dark matter that holds galaxies together? what is the dark energy that is pulling the universe apart? While the standard cosmological model for the universe has seen many successes in recent years—achieving percent-level accuracy on many of its parameters—we still lack satisfactory answers to these basic questions.

One of the biggest mysteries is the recently-confirmed accelerated expansion of the universe, which has been attributed to dark energy of invisible but otherwise unknown form accounting for about 70% of the energy in the universe today (Riess et al. 1998; Perlmutter et al. 1999). Almost as puzzling is the dark matter, inferred through its gravitational pull, which makes up roughly 85% of the matter in the

universe (Zwicky 1937; Rubin & Ford 1970). It is thought to be a new fundamental particle that interacts only through gravity, but its basic properties, such as its mass, are still unknown. We are also largely ignorant of the mechanism behind inflation, the initial period of exponential expansion of space. These mysteries can be solved in part by comparing precision measurements of cosmological probes with predictions from theory.

The spatial distribution of matter in the universe is one such probe of cosmological information. For example, acoustic waves in the early universe, called Baryon Acoustic Oscillations, produced a statistical feature in the distribution of matter that allows us to measure parameters associated with dark energy (Seo & Eisenstein 2003). In general, the statistics of the matter distribution are sensitive to both the initial conditions and the evolution of the universe and thus can be used to study the dynamics of dark energy, the properties of components such as dark matter and neutrinos, and the nature of inflation (Peebles 1980; Dodelson 2003). Using measured statistics to constrain cosmological parameters requires an accurate theoretical model of the statistics of the large-scale structure in the universe. This Chapter lays out the basic tools needed to construct such a theoretical model.

1.1 The Expanding Universe

In the standard model of cosmology, the universe is assumed to be spatially isotropic, to be expanding isotropically, and to be homogeneous when smoothed over large enough scales. These assumptions are valid on scales larger than about 100 Megaparsecs. This homogeneous, isotropic, expanding space-time can be expressed using the Friedmann-Lemaitre-Robertson-Walker (FLRW) metric:

$$ds^2 = a(t)^2 d\mathbf{x}^2 - c^2 dt^2 \ , \tag{1.1}$$

where c is the speed of light, ds is the space-time separation between the points $(\mathbf{x}, t)$ and $(\mathbf{x} + d\mathbf{x}, t + dt)$, and $d\mathbf{x}$ is a 3-dimensional spatial metric in comoving (non-expanding) coordinates that can have positive, negative, or zero spatial curvature. The scale factor, $a(t)$, describes the expansion of space. It is equal to zero at the time of the big bang ($t = 0$) and is, at least initially, increasing in time.

Einstein's equations relate the evolution of the scale factor to the energy density, $\varepsilon(t)$, of the universe giving us an equation of motion for $a(t)$ that is called the Friedmann Equation:

$$H(t)^2 \equiv \left(\frac{\dot{a}}{a}\right)^2 = \frac{8\pi G}{3}\varepsilon(t) - \frac{kc^2}{a(t)^2} \ , \tag{1.2}$$

where $H(t)$ is the Hubble expansion rate at time t, defined as the logarithmic derivative of the scale factor, a, with respect to time (the time derivative is indicated by the dot). In Equation 1.2, k is the spatial curvature of the universe and can be equal to

-1 (negatively curved), 0 (flat), or $+1$ (positively curved). The Friedmann Equation describes energy conservation in an expanding universe.

The total energy density of the universe is the sum of the contribution of each component of energy, $\varepsilon(t) = \sum_i \varepsilon_i(t)$. We assume that universe is expanding adiabatically, meaning there is no net transfer of heat, and that each component can be modeled as a fluid. The evolution of the energy density of each component can then be described by the following fluid equation:

$$\dot{\varepsilon} + 3\frac{\dot{a}}{a}\left(\varepsilon + \frac{p}{c^2}\right) = 0 \ , \tag{1.3}$$

where p is the pressure of the fluid. Again, the dots refer to derivatives with respect to time. The *equation of state* of each fluid (or component of energy) is the ratio of its pressure to its energy density and is parameterized by w: $p_i = w_i \varepsilon_i c^2$. Each component of energy may obey a different equation of state. The solution to the fluid equation for arbitrary w is: $\varepsilon(t) \propto a(t)^{-3(1+w)}$. We now consider the equations of state of the different components of energy in the universe: matter (ordinary "baryonic" matter and dark matter), radiation (including neutrinos), and dark energy.

Both ordinary matter (protons, neutrons, electrons) and dark matter are non-relativistic throughout most of the history of the universe, meaning their thermal velocities are much smaller than the speed of light. Therefore, the equation-of-state parameter for matter, w_m, is very close to zero and the energy density varies as $a(t)^{-3}$. We arrive at the same result by considering that the volume of the universe is increasing as $a(t)^3$ and the rest-mass energy density of matter is inversely proportional

to the volume.

Electromagnetic radiation and other relativistic species such as neutrinos have an equation-of-state parameter of $w_R = \frac{1}{3}$, so their energy densities vary as $a(t)^{-4}$. The extra factor of a^{-1} compared to matter comes from the fact that radiation becomes stretched as space expands, decreasing its energy as a^{-1}. This phenomenon is known as *redshift*, denoted by z, and it turns out to be a convenient alternative time variable to time (t) or scale factor (a) because it is more directly observable. The redshift of light emitted from rest at scale factor $a(t)$ and observed today ($a(t_0) = 1$) is the ratio of the observed wavelength to the emitted wavelength and is inversely proportional to the scale factor at which the light was emitted:

$$1 + z = \frac{\lambda_{\text{obs}}}{\lambda_{\text{emit}}} = \frac{1}{a} \,, \tag{1.4}$$

where λ is wavelength. From Equation 1.4, we see that the redshift today is zero and it increases to infinity as we look further back in time.

The final component we must consider in Equation 1.2 is the dark energy. While the equation-of-state parameter of dark energy is unknown, we observe that it causes an accelerated expansion of space. One can show that a positive acceleration ($\ddot{a}$) requires that $w < -\frac{1}{3}$. In the simplest model of dark energy, the equation-of-state parameter is -1, giving a constant energy density $\varepsilon(t)$. This is called a *cosmological constant* and is referred to as Λ. The standard model of cosmology—called ΛCDM—assumes dark energy is a cosmological constant. Measurements of w show that it is close to -1, but errors are still at the level of about 20%. Here, we will leave w as an

unknown parameter.

We can now rewrite Equation 1.2 in terms of these components of energy and as a function of redshift (as opposed to time). We define a critical density $\varepsilon_c \equiv 3H_0^2/(8\pi G)$, where $H_0 \equiv H(t_0)$ is the Hubble expansion rate today. The current energy density of each component can then be expressed as a fraction of the critical density, $\Omega_i \equiv \varepsilon_i(t_0)/\varepsilon_c$. Equation 1.2 becomes:

$$H(z)^2 = H_0^2 \left[\Omega_m (1+z)^3 + \Omega_R (1+z)^4 + \Omega_{\rm DE} (1+z)^{3(1+w)} - \frac{kc^2}{H_0^2}(1+z)^2 \right] , \quad (1.5)$$

where Ω_m is the fractional (baryonic + dark) matter density, Ω_R is the fractional radiation density, and $\Omega_{\rm DE}$ is the fractional dark energy density. If we evaluate this equation at $z = 0$ (today), we arrive at the expression: $\Omega_m + \Omega_R + \Omega_{\rm DE} = 1 + \frac{kc^2}{H_0^2}$. This means that for a flat universe ($k = 0$), the total energy density is equal to the critical energy density. Measurements of the geometry of the universe indicate that it is very close to flat, so k is often taken to be zero.

Equation 1.5 shows how the expansion rate of the universe ($H(z)$) is influenced by the nature of the various components (Ω_m, Ω_R, $\Omega_{\rm DE}$, w). Currently, the best-fit ΛCDM model has a matter density of around $\Omega_m = 0.27$, radiation density of $\Omega_R = 8 \times 10^{-5}$, and a cosmological constant ($w = -1$) with a density of $\Omega_{\rm DE} = \Omega_\Lambda = 0.73$. By measuring the Hubble expansion rate at different redshifts, we can constrain the parameters of our cosmological model. Next, we describe one the most powerful methods for measuring $H(z)$.

1.2 Baryon Acoustic Oscillations

In the standard big-bang model, the early universe was made up of a hot, dense plasma consisting of tightly coupled electrons, baryons, and photons. The invisible dark matter was coupled to the plasma through gravitation. Tiny density fluctuations in the plasma density created gravitational potential wells in the slightly denser regions. In these regions, the attractive force of gravity was opposed by photon pressure, setting up acoustic waves in the plasma with a characteristic sound speed of about half the speed of light.

When the universe expanded and cooled sufficiently, about 380,000 years after the big bang ($a(t) \approx 1 \times 10^{-3}$, $z \approx 1100$), photons decoupled from the baryons and the acoustic waves were frozen into the distribution of the baryons. The waves that were generated in over-dense regions in the plasma had traveled about 150 Megaparsecs (in comoving coordinates) by the time the photons decoupled. These waves—called Baryon Acoustic Oscillations (BAO)—are imprinted as an enhancement in the probability of finding over-dense (or under-dense) regions about 150 Megaparsecs from each other, introducing a characteristic length scale in the initial density field after decoupling (Peebles & Yu 1970; Silk 1968; Sunyaev & Zel'dovich 1970; Bond & Efstathiou 1984).

The comoving scale of the BAO is large compared to the scale of structures we observe in the universe. As we will see in the next section, this means that the BAO scale remains (almost) constant over time. The known length scale, or "standard

ruler", on the sky gives us a way to measure distances in the universe.

By measuring the BAO scale at a given redshift, we can calculate the angular diameter distance to that redshift. The angular diameter distance is the ratio of the known scale ($r_{\rm BAO}$) to its observed angular size on the sky ($\Delta\theta$):

$$\begin{aligned} d_A(z) &= \frac{r_{\rm BAO}}{\Delta\theta} \\ &= \frac{1}{1+z}\int_0^z \frac{cdz'}{H(z')} \,. \end{aligned} \tag{1.6}$$

Because the angular diameter distance contains information about the Hubble rate, $H(z)$, we can use it to distinguish between different cosmological models. Figure 1.1 shows the angular diameter distance versus redshift for various models of dark energy. The black line shows the ΛCDM model, which has dark energy equation-of-state parameter $w = -1$. The green dot-dashed line shows a model with $w = -1.5$, and the blue dashed line shows a model with $w = -0.4$. The angular diameter distance is sensitive to different models of dark energy. By measuring the BAO scale over a range of redshifts, we can constrain the dark energy equation-of-state parameter, w (Seo & Eisenstein 2003).

1.3 Statistics of Large-scale Structure

Using the observed BAO signal to learn about dark energy requires a theoretical model of the statistics of the distribution of matter in the universe. We model the spatial distribution of matter by first considering only the dark matter. Because dark

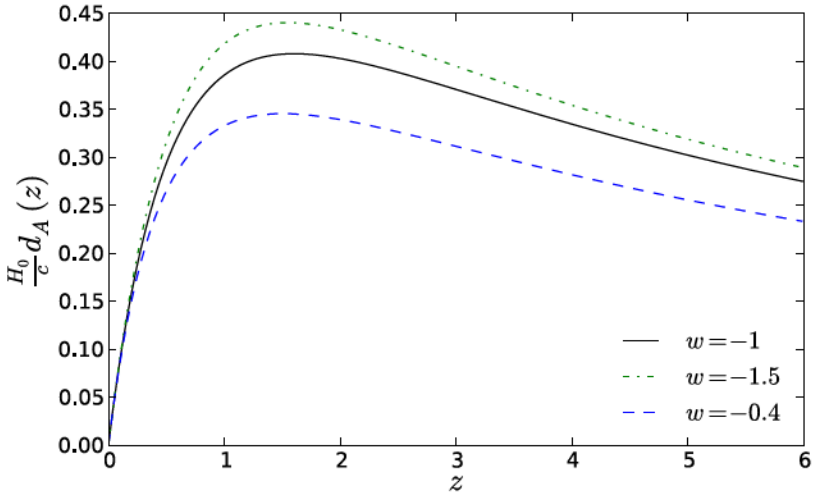

Figure 1.1: The angular diameter distance (scaled by H_0/c) as a function of redshift for different models of dark energy. The black line is for $w = -1$, a cosmological constant.

matter makes up most of the matter in the universe, we assume that the distribution of baryonic matter is governed by that of the dark matter. In other words, the baryonic matter traces the underlying dark matter distribution. This simplifies the picture because in the standard framework, the dark matter only interacts through gravity, and thus the model can ignore complicated baryonic physics such as radiative transfer.

Models of structure formation connect the statistics of the late-time matter distribution to those of the initial density perturbations, which were the seeds for the structure in the universe today. In Section 1.3.2, we review the statistics of the initial density perturbations.

Within the standard framework, the evolution of the dark matter distribution on very large scales is simple to model because the effect of gravity can be treated linearly. We review the linear theory of structure formation in Section 1.3.2. On BAO scales, linear theory begins to break down at low redshifts ($z < 1$). In order to accurately constrain dark energy parameters as measurements become more precise, we must be able to model the low-redshift behavior of the BAO. One way to do this is with numerical N-body simulations. However, this can be computationally expensive because each simulation must resolve a large range of scales, and a new simulation must be run for each set of cosmological parameters considered. A more economical approach is to use approximate analytical expressions that model the dynamics accurately to within the measurement error. In Section 1.3.3, we describe two per-

turbative approaches to modeling the evolution of structure formation analytically. These approaches allow us to go beyond linear theory so that we can predict the BAO signal more accurately.

Finally, we measure distances to galaxies using their redshifts. However, peculiar velocities complicate the relationship between redshift and distance, and the observed galaxy distribution appears anisotropic. Modeling the observed galaxy statistics requires that we include the effects of redshift-space distortions, described in Section 1.3.4.

1.3.1 Initial Conditions

In the standard model, the universe began with a single originating event, called the big bang, followed by an inflationary period during which space expanded exponentially. Tiny quantum fluctuations were amplified during inflation and were the seeds for the structures we observe today.

Although we do not yet fully understand the mechanism behind inflation, most inflation theories make similar predictions about the statistics of the resulting primordial fluctuations. First, most inflation theories predict that the initial fluctuations constitute a stationary and isotropic Gaussian process. Also, the variance of the fluctuations at each scale, otherwise known as the power spectrum of fluctuations, is predicted to be close to scale-invariant (Liddle & Lyth 2000).

These primordial fluctuations seeded perturbations in the matter density with

similarly Gaussian statistics and a power spectrum that depends on cosmological parameters. To quantify the statistics of the initial density perturbations, we consider the over-density, which is the fractional deviation from the mean density (Peebles 1980):

$$\delta(\mathbf{x}) = \frac{\rho(\mathbf{x})}{\bar{\rho}} - 1 \ , \tag{1.7}$$

where $\rho(\mathbf{x})$ is the density of matter at position $\mathbf{x}$ and $\bar{\rho}$ is the mean density of the universe.

The Fourier mode at $\mathbf{k}$ of the over-density is:

$$\hat{\delta}(\mathbf{k}) = \int \delta(\mathbf{x}) e^{-i\mathbf{k}\cdot\mathbf{x}} d^3\mathbf{x} \ , \tag{1.8}$$

where $\hat{\delta}(\mathbf{k})$ is complex and Hermitian, meaning that $\hat{\delta}(\mathbf{k})$ is equal to $\hat{\delta}^*(-\mathbf{k})$, the complex-conjugate of $\hat{\delta}(-\mathbf{k})$.

The inverse Fourier transform is defined as:

$$\delta(\mathbf{x}) = \frac{1}{(2\pi)^3} \int \hat{\delta}(\mathbf{k}) e^{i\mathbf{k}\cdot\mathbf{x}} d^3\mathbf{k} \ . \tag{1.9}$$

Because $\delta(\mathbf{x})$ is a real zero-mean Gaussian random field (i.e. the Fourier modes are uncorrelated), it is fully specified by its power spectrum, $P(k)$, which is related to the expectation value between the Fourier modes $\hat{\delta}(\mathbf{k})$ and $\hat{\delta}(-\mathbf{k}')$:

$$\langle \hat{\delta}(\mathbf{k}) \hat{\delta}^*(\mathbf{k}') \rangle \equiv (2\pi)^3 P(k) \delta_D(\mathbf{k} - \mathbf{k}') \ , \tag{1.10}$$

where δ_D is a 3-dimensional Dirac-delta function. Note that the power spectrum is a function only of the length of the vector $\mathbf{k}$. This is because the field is stationary and isotropic. The wavenumber, k, has units of inverse length.

The inverse Fourier transform of the power spectrum is the 2-point correlation function:

$$\langle \delta(\mathbf{x})\delta(\mathbf{x}+\mathbf{r})\rangle \equiv \xi(r) = \frac{1}{(2\pi)^3}\int P(k)e^{i\mathbf{k}\cdot\mathbf{r}}d^3\mathbf{k}\ . \tag{1.11}$$

The correlation function only depends on the length, r, of the separation vector $\mathbf{r}$.

The power spectrum of initial density perturbations is a function of cosmological parameters and can be predicted by numerically solving for the evolution of perturbations in the early universe (Seljak & Zaldarriaga 1996; Lewis et al. 2000; Dodelson 2003). Figure 1.2 shows the power spectrum and correlation function of the initial matter density distribution in a ΛCDM universe. The units used here (Mpc/h) are distance divided by h, where $h \equiv H_0/(100\text{km/s/Mpc})$. This convention is widely used in cosmology. Historically, h represents our uncertainty in H_0, which is needed to calculate distances in the universe. Current measurements of H_0 indicate that $h \approx 0.7$. Note the BAO peak in the correlation function at about110 Mpc/h, which shows up as wiggles in the power spectrum at around $0.04 < k < 0.3$ h/Mpc.

Now we must connect the statistics of the observed density distribution at late times to those of the initial density field in order to constrain cosmology from large scale structure.

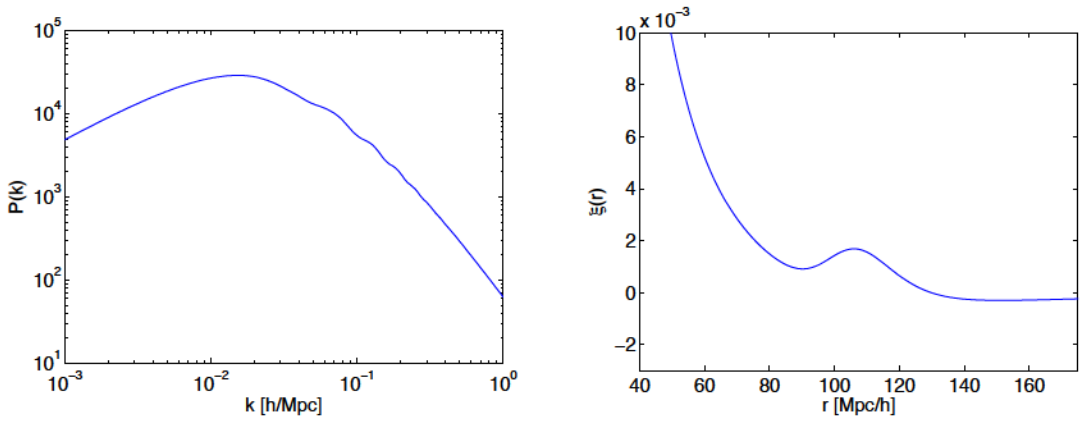

Figure 1.2: The power spectrum (left) and correlation function (right) of the initial matter density distribution in ΛCDM. The amplitudes of both have been normalized to match the large-scale fluctuations in the universe at $z = 0$ (today).

1.3.2 Linear Structure Formation

We model the evolution of the matter distribution after decoupling from photons by assuming that dark matter is a zero-pressure fluid with non-relativistic peculiar velocities. This allows us to use the equations for an ideal fluid in the non-relativistic Newtonian limit. We work in comoving coordinates, $\mathbf{x} \equiv \mathbf{r}(t)/a(t)$, where $\mathbf{r}(t)$ is the physical separation at time t. In these coordinates, the evolution equations of the dark matter fluid are:

$$\frac{\partial \delta}{\partial t} + \frac{1}{a}\nabla \cdot [(1+\delta)\mathbf{v}] = 0 \ , \tag{1.12}$$

$$\frac{\partial \mathbf{v}}{\partial t} + \frac{1}{a}(\mathbf{v}\cdot\nabla)\,\mathbf{v} = -\frac{\dot{a}}{a}\mathbf{v} - \frac{1}{a}\nabla\phi \ , \tag{1.13}$$

$$\nabla^2\phi = 4\pi G a^2 \bar{\rho}\delta \ , \tag{1.14}$$

where $\dot{a} = da/dt$.

To find the solution to these equations in the limit that $\delta, \mathbf{v} \ll 1$, we keep only linear terms in δ and $\mathbf{v}$, and solve for $\delta(t)$. By combining Equation 1.12 and Equation 1.14 with the divergence of Equation 1.13, we arrive at the linearized fluid equation for δ:

$$\frac{\partial^2 \delta}{\partial t^2} + 2\frac{\dot{a}}{a}\frac{\partial \delta}{\partial t} + \frac{3H_0^2\Omega_m}{2a^3}\delta = 0 \ , \tag{1.15}$$

where we have made the substitution $4\pi G\bar{\rho} = \frac{3}{2}H_0^2\Omega_m a^{-3}$ from the Friedmann equation.

In a flat matter-dominated universe ($\Omega_m = 1$, $\Omega_\Lambda = 0$), where the scale factor evolves as $a \propto t^{2/3}$, we find the growing-mode solution to this equation is $\delta(t) \propto a(t)$. In other words, as the universe expands, over-dense regions become more dense and under-dense regions become less dense. The matter-only solution is valid in the era of matter domination ($10^4 > z > 1$), but in the recent universe ($z < 1$) we must also take into account the contribution from dark energy. The growing mode solution in the more general case is $\delta(t) \propto D(a)$ where $D(a)$ is the linear growth function and is defined as (Dodelson 2003):

$$D(a) = \frac{5\Omega_m H(a)}{2H_0}\int_0^a \frac{H_0^2 da'}{\left(a'H(a')\right)^3} \ . \tag{1.16}$$

Figure 1.3 shows the growth function versus scale factor for a standard ΛCDM universe and a matter-dominated universe. Note that for the matter-dominated universe, $D(a) = a$ as expected.

Linear theory states that on large scales, where $\delta \ll 1$, the matter distribution

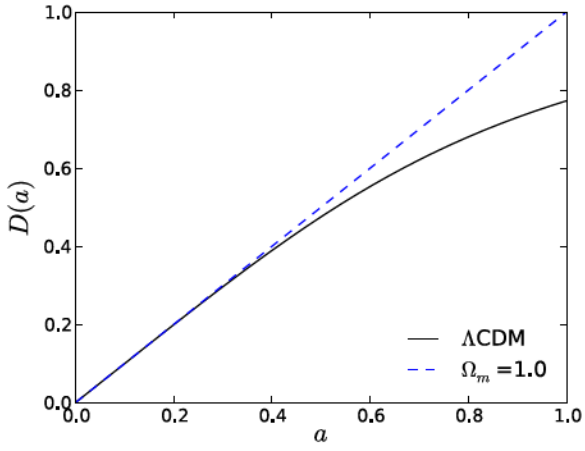

Figure 1.3: The linear growth function versus scale factor for a ΛCDM ($\Omega_m = 0.27$, $\Omega_\Lambda = 0.73$) universe (black line) and a flat, matter-only universe (blue dashed line). In a matter-only universe, the growth function is equal to the scale factor.

evolves as $\delta(\mathbf{x}, t) = D(t)\delta_L(\mathbf{x})$, where $\delta_L(\mathbf{x})$ is the initial (Gaussian) density field at some early time t_i divided by the growth function at that time, $D(t_i)$. This means that the density field on linear scales remains Gaussian, and the 2-point statistics are sufficient for characterizing the distribution. The power spectrum and correlation function at time t are related to the initial statistics simply:

$$P(k, t) = D(t)^2 P_L(k) \ , \tag{1.17}$$

$$\xi(r, t) = D(t)^2 \xi_L(r) \ . \tag{1.18}$$

In the linear regime, the statistics of the density field retain their initial shape, and can thus be directly connected to cosmological information encoded in $P_L(k)$ and $\xi_L(r)$. The BAO feature can be modeled well using linear theory at high redshift ($z >$

1). However, at low redshifts ($z < 1$), nonlinearity has an appreciable effect on the shape and position of the BAO feature. Using linear theory to model the BAO at low redshifts results in errors in the determination of dark energy parameters. To better model the statistics on these quasi-linear scales, we use cosmological perturbation theory.

1.3.3 Nonlinear Structure Formation

There are two distinct approaches to modeling the dynamics of structure formation beyond linear theory. The first is an Eulerian approach, which focuses on the density and velocity fields of the dark matter fluid. The second is a Lagrangian approach, which tracks the positions and velocities of fluid particles. We discuss both approaches here.

Eulerian Perturbation Theory

Linear theory applies in regimes where $\delta \ll 1$, which corresponds to very large scales and high redshift. On small scales, such as galactic scales, the evolution is fully nonlinear, and densities can become much larger than the mean density, $\delta \gg 1$. On an intermediate range of scales, where the over-density is small but not necessarily much smaller than 1, we can use perturbation theory to describe the evolution of the density field. Here we briefly outline the main concepts of Standard Perturbation Theory (SPT). For more details, see Vishniac (1983); Fry (1984); Jain & Bertschinger

(1994); Scoccimarro & Frieman (1996); Bernardeau et al. (2002).

We first combine the divergence of Equation 1.13 with Equation 1.14. We Fourier transform the resulting equation along with Equation 1.12 and rearrange them such that all nonlinear interaction terms are on the right hand side:

$$\frac{\partial\hat{\delta}}{\partial\tau} + \hat{\theta} = -\int d^3\mathbf{k}_1 \int d^3\mathbf{k}_2 \delta_D(\mathbf{k}_1 + \mathbf{k}_2 - \mathbf{k}) \frac{\mathbf{k}\cdot\mathbf{k}_1}{k_1^2} \hat{\theta}(\mathbf{k}_1, \tau)\hat{\delta}(\mathbf{k}_2, \tau) \ , \tag{1.19}$$

$$\frac{\partial\hat{\theta}}{\partial\tau} + \frac{\dot{a}}{a}\hat{\theta} + \frac{3\Omega_m a^2 H^2}{2}\hat{\delta} = -\int d^3\mathbf{k}_1 \int d^3\mathbf{k}_2 \delta_D(\mathbf{k}_1 + \mathbf{k}_2 - \mathbf{k}) \frac{k^2(\mathbf{k}_1\cdot\mathbf{k}_2)}{2k_1^2k_2^2} \hat{\theta}(\mathbf{k}_1, \tau)\hat{\theta}(\mathbf{k}_2, \tau) \ , \tag{1.20}$$

where we have defined the quantity $\theta \equiv \nabla\cdot\mathbf{v}$. We also have converted from coordinate time, t, to conformal time, τ, using the relation $d\tau = dt/a$.

For a matter-dominated universe ($\Omega_m = 1$), this set of equations can be solved perturbatively using the following expansions for $\hat{\delta}(k,\tau)$ and $\hat{\theta}(k,\tau)$:

$$\hat{\delta}(\mathbf{k},\tau) = \sum_{n=1}^{\infty} a^n(\tau)\delta_n(\mathbf{k}) \ , \tag{1.21}$$

$$\hat{\theta}(\mathbf{k},\tau) = \sum_{n=1}^{\infty} \dot{a}a^{n-1}(\tau)\theta_n(\mathbf{k}) \ . \tag{1.22}$$

For an arbitrary cosmology—one with dark energy, for example—the expansion is more complicated, but it turns out that making the substitution $a(\tau) \to D(\tau)$ in Equations 1.21 and 1.22 is a very good approximation (Scoccimarro et al. 1998).

Plugging Equations 1.21 and 1.22 into Equations 1.19 and 1.20 results in recursive

solutions for δ_n and θ_n:

$$\delta_n(\mathbf{k}) = \int d^3\mathbf{q}_1 \cdots \int d^3\mathbf{q}_n \delta_D(\mathbf{q}_1 + \cdots + \mathbf{q}_n - \mathbf{k}) F_n(\mathbf{q}_1, ..., \mathbf{q}_n) \delta_L(\mathbf{q}_1) \cdots \delta_L(\mathbf{q}_n) \ , \tag{1.23}$$

$$\theta_n(\mathbf{k}) = -\int d^3\mathbf{q}_1 \cdots \int d^3\mathbf{q}_n \delta_D(\mathbf{q}_1 + \cdots + \mathbf{q}_n - \mathbf{k}) G_n(\mathbf{q}_1, ..., \mathbf{q}_n) \delta_L(\mathbf{q}_1) \cdots \delta_L(\mathbf{q}_n) \ , \tag{1.24}$$

where δ_D is the 3-dimensional Dirac-delta function. The kernels F_n and G_n are defined recursively, with $F_1 = G_1 = 1$. The recursive formula for the kernels can be found in Appendix A. The symmetrized second-order kernels are:

$$F_2^{(s)}(\mathbf{k}_1, \mathbf{k}_2) = \frac{5}{7} + \frac{2}{7}\frac{(\mathbf{k}_1 \cdot \mathbf{k}_2)^2}{k_1^2 k_2^2} + \frac{(\mathbf{k}_1 \cdot \mathbf{k}_2)}{2}\left(\frac{1}{k_1^2} + \frac{1}{k_2^2}\right) \ , \tag{1.25}$$

$$G_2^{(s)}(\mathbf{k}_1, \mathbf{k}_2) = \frac{3}{7} + \frac{4}{7}\frac{(\mathbf{k}_1 \cdot \mathbf{k}_2)^2}{k_1^2 k_2^2} + \frac{(\mathbf{k}_1 \cdot \mathbf{k}_2)}{2}\left(\frac{1}{k_1^2} + \frac{1}{k_2^2}\right) \ . \tag{1.26}$$

Using the expressions above we can calculate the density power spectrum perturbatively:

$$\begin{aligned} \langle \delta(\mathbf{k}, \tau)\delta(\mathbf{k}', \tau)\rangle &= (2\pi)^3 P(k, \tau)\delta_D(\mathbf{k} + \mathbf{k}') \\ &= D^2(\tau)\langle \delta_1(\mathbf{k})\delta_1(\mathbf{k})\rangle + D^4(\tau)\big[\langle \delta_1(\mathbf{k})\delta_3(\mathbf{k}')\rangle + \langle \delta_1(\mathbf{k}')\delta_3(\mathbf{k})\rangle \\ &\quad + \langle \delta_2(\mathbf{k})\delta_2(\mathbf{k}')\rangle\big] + \cdots \end{aligned} \tag{1.27}$$

The first term in Equation 1.27 is the usual linear power spectrum, proportional to $D^2(\tau)$, as we found in linear theory. The first nonlinear term, proportional to $D^4(\tau)$, can be written as the sum of two terms:

$$P_2(k) = P_{22}(k) + 2P_{13}(k) \ , \tag{1.28}$$

where $P_{22}(k)$ is the contribution from δ_2:

$$P_{22}(k) = 2 \int d^3\mathbf{q} P_L(q) P_L(|\mathbf{k}-\mathbf{q}|) \left[F_2^{(s)}(\mathbf{q}, \mathbf{k}-\mathbf{q})\right]^2 . \tag{1.29}$$

The $P_{13}(k)$ term is the contribution from δ_1 and δ_3, and involves the 3rd order kernel, F_3:

$$P_{13}(k) = 3P_L(k) \int d^3\mathbf{q} P_L(q) F_3^{(s)}(\mathbf{q}, -\mathbf{q}, \mathbf{k}) . \tag{1.30}$$

Note that the nonlinear correction in Equation 1.29 has the form of a convolution in Fourier space. Higher-order corrections become quite complicated as they involve higher degrees of convolutions.

An important consequence of nonlinear structure formation is that the density field becomes non-Gaussian. This means that the 2-point statistics are not sufficient to describe the distribution and higher-point statistics contain non-trivial information. SPT can be used to predict higher-point statistics, such as the bispectrum, perturbatively as will be shown in Chapter 4.

Lagrangian Perturbation Theory

Lagrangian Perturbation Theory (LPT) takes quite a different approach to fluid dynamics. In this formalism, the initial positions of the particles, $\mathbf{q}$, are mapped to their final positions, $\mathbf{x}$ through a displacement field $\mathbf{\Psi}$ (Zel'dovich 1970; Bouchet et al. 1995; Bernardeau et al. 2002):

$$\mathbf{x}(\mathbf{q}, t) = \mathbf{q} + \mathbf{\Psi}(\mathbf{q}, t) . \tag{1.31}$$

The displacement field $\mathbf{\Psi}(\mathbf{q}, t)$ is taken to be small, and can be written perturbatively:

$$\mathbf{\Psi}(\mathbf{q}, t) = \mathbf{\Psi}^{(1)}(\mathbf{q}, t) + \mathbf{\Psi}^{(2)}(\mathbf{q}, t) + \mathbf{\Psi}^{(3)}(\mathbf{q}, t) + \cdots \tag{1.32}$$

Because the perturbation is in the displacement field, there is no requirement that the densities be small in LPT. To find the density at time t we use mass conservation:

$$\bar{\rho} d^3\mathbf{q} = \rho(\mathbf{x}, t) d^3\mathbf{x} \ , \tag{1.33}$$

$$\frac{\rho(\mathbf{x}, t)}{\bar{\rho}} = |J(\mathbf{q}, t)|^{-1} \ , \tag{1.34}$$

where J is the Jacobian of the transformation from $\mathbf{q}$ to $\mathbf{x}$:

$$J(\mathbf{q}, t) \equiv \frac{\partial x_i}{\partial q_j} \ . \tag{1.35}$$

In the first-order approximation, called the Zel'dovich approximation (Zel'dovich 1970), the displacement field is simply the divergence of the initial potential field, scaled by the linear growth factor:

$$\mathbf{\Psi}^{(1)}(\mathbf{q}, t) = -D(t) \nabla \phi^{(1)}(\mathbf{q}) \ . \tag{1.36}$$

The Poisson Equation (1.14) relates the gravitational potential to the initial (Gaussian) over-density field. The Zel'dovich approximation has been used widely to study structure formation, as well as to set up initial conditions in N-body simulations.

Both the Eulerian and Lagrangian approaches to perturbation theory are useful in different ways. Eulerian perturbation theory has a more natural connection with observables (density and velocity fields), but it breaks down on much larger scales than Lagrangian perturbation theory. Both approaches have been employed extensively to study the dynamics of nonlinear structure formation.

1.3.4 Redshift-space Distortions

We have assumed until now that the matter distribution is isotropic in space. While this is likely a reasonable assumption, in reality our observational limitations make the distribution appear anisotropic. This is because we measure distances along the line-of-sight differently than on the plane of the sky.

In galaxy redshift surveys, the positional information available for each galaxy is its angular position on the plane of the sky and its redshift. We use the distance-redshift relation to convert redshift to distance along the line of sight:

$$d = \int_0^z \frac{c dz}{H(z)} \ , \tag{1.37}$$

where z is the redshift of the galaxy, and $H(z)$ is the Hubble expansion rate at that redshift. In the local universe, this can be approximated by the linear relation $d = cz/H_0$.

In converting redshift to distance, we assume the galaxy's line-of-sight speed is due only to the expansion of space. In reality, galaxies also have peculiar velocities that depend on their local environments so the measured redshift is the sum of the "true" cosmological redshift and the peculiar redshift:

$$z_{\rm obs} = z_{\rm true} + z_{\rm pec} \ . \tag{1.38}$$

Using the observed redshift leads to errors in the line-of-sight distances to galaxies. The resulting spatial distribution measured will be anisotropic along the line-of-sight direction (Kaiser 1987; Fry & Gaztanaga 1994; Hamilton 1998).

The effect of redshift-space distortions on the statistics of the matter distribution can be modeled as a coordinate transformation. The mapping from real space ($\mathbf{x}$) to redshift space ($\mathbf{s}$) is:

$$\mathbf{s} = \mathbf{x} - f v_z(\mathbf{x}) \hat{z} \ , \tag{1.39}$$

where f is the logarithmic derivative of the linear growth function $d \ln D(a) / d \ln a$, $\hat{z}$ is the line-of-sight direction, and $v_z(\mathbf{x})$ is related to the peculiar velocity ($\mathbf{u}(\mathbf{x})$) along the line of sight: $v_z(\mathbf{x}) \equiv -u_z(\mathbf{x})/(Haf)$.

To linear order, the redshift-space power spectrum can modeled with a simple multiplicative factor that is a function of angle:

$$P_L^s(k, \mu) = P_L(k)(1 + f\mu^2)^2 \ , \tag{1.40}$$

where μ is the cosine of the angle between $\mathbf{k}$ and the line-of-sight direction $\hat{z}$ (Kaiser 1987).

The equivalent expression in configuration space is:

$$\xi_L^s(s, \gamma) = \left(1 + \frac{2f}{3} + \frac{f^2}{5}\right) \xi_0(s) - \left(\frac{4f}{3} + \frac{4f^2}{7}\right) \mathcal{P}_2(\gamma)\xi_2(s) + \frac{8f^2}{35} \mathcal{P}_4(\gamma)\xi_4(s) \ , \tag{1.41}$$

where $\gamma \equiv \hat{s} \cdot \hat{z}$, $\mathcal{P}_\ell$ is the Legendre polynomial of order ℓ, and $\xi_n(s)$ are linear correlation functions with spherical Bessel function kernels:

$$\xi_n(s) \equiv \frac{1}{2\pi^2} \int P_L(k) j_n(kr) k^2 dk \ . \tag{1.42}$$

Modeling redshift-space statistics beyond linear order, for example using SPT, becomes much more complicated (Bernardeau et al. 2002). Some of the redshift-space kernels from SPT are given in Appendix A.

1.4 Focus of this Work

The statistics of the large-scale structure are an important cosmological probe. This is in large part because Baryon Acoustic Oscillations provide one of the cleanest signals available to determine cosmological distances, which in turn reveal the dynamics of dark energy. While systematic effects, such as nonlinearity and redshift-space distortions, are small on BAO scales, surveys are becoming so large and measurements so precise that it is now necessary that we fully understand these effects through theoretical modeling.

As mentioned previously, the most accurate way to model these effects is through numerical N-body simulations, but this is a computationally expensive technique because it requires resolving a large range of scales. Another disadvantage of this type of approach is that we gain relatively little physical insight because the relationship between the parameters of the simulation and the systematic effects is not always clear.

A strong alternative to numerical simulation on BAO scales is a perturbative description of the dynamics of structure formation. Previous work in this area has

been done almost exclusively in Fourier space using SPT. While these results have so far been quite successful, the analytical expressions for the nonlinear and redshift-space statistics become prohibitively difficult to implement as we start to push to higher orders for greater accuracy.

I began my thesis work by developing a configuration-space approach to perturbation theory, starting from the Zel'dovich Approximation. The motivation for this new approach was that nonlinear corrections and redshift-space distortions may take on a simpler form in configuration space. Also, because the BAO is a localized feature in configuration space, this is a more natural coordinate system to work in and the result may give us more physical intuition about the nonlinear effects at play. In Chapter 2, I outline this new approach in real space (without redshift-space distortions) and verify the result both analytically and numerically. Next, I show that we can extend the calculation to redshift space to describe the nonlinear anisotropic correlation function to 2nd order. Unlike the Fourier-space equivalent, the expression has a mathematically simple form involving products as opposed to convolutions.

I then considered the implications of the non-Gaussianity of the density field. As nonlinear gravitational evolution takes place, the initially Gaussian density field becomes non-Gaussian. This is obvious when one considers that densities can be arbitrarily high, but cannot be negative. This implies that the 2-point correlation function of the density field does not access all of the information in the distribution. One approach that has been recently employed is to assume the field is log-normally

distributed and to instead study the 2-point statistics of the log-transformed density (Neyrinck et al. 2009a).

I was interested in how such a transform effects the bias of the BAO feature in the correlation function. In Chapter 3, I use the same configuration-space approach described earlier to explore the effects of various density transforms on the location and shape of the BAO feature in the nonlinear 2-point correlation function. The results suggest that the log transform, which produces a more Gaussian distribution, gives a less biased BAO peak position at low redshift. This may have implications for future BAO detections and could reduce errors on measured dark energy parameters.

Another way to approach non-Gaussianity is to consider the higher-point statistics of the density field. The 3-point correlation function and its Fourier transform, the bispectrum, contain information about inflation parameters, structure formation, and galaxy bias. However, the theoretical modeling of these statistics is not yet precise enough to do sophisticated data analysis. In Chapter 4, I review current techniques for modeling the nonlinear matter bispectrum, both analytically and numerically. I test the limitations of these techniques to understand where improvements are needed in order to accurately predict the nonlinear matter bispectrum. With more accurate theoretical models, we can extract cosmological information from the galaxy bispectrum.

In studying the Fourier-space models of the bispectrum, I found that a configuration-space approach could again aid in modeling the effects of redshift-space distortions. In

Chapter 5 I show how the configuration-space approach from Chapter 2 can be used to calculate the first non-zero term of the 3-point correlation function, first in real space. While this real-space result has been previously found through Fourier-transform, the configuration-space approach is much simpler mathematically and more powerful because it can be extended to redshift space. I present for the first time the result for the tree-level redshift-space 3-point correlation function. While these preliminary results have yet to be thoroughly tested, their simple representation in configuration space is promising for future modeling of 3-point statistics in redshift space.

The results presented in this thesis highlight the advantages of a configuration-space approach over a Fourier-space approach in modeling the statistics of large-scale structure. In Chapter 6 I summarize my findings and discuss directions for future research. As surveys begin to deliver vast amounts of data, systematic effects are become increasingly important to understand. The developments presented here provide a new perspective on theoretical modeling of the statistics of large-scale structure and are a promising avenue for future work.

Chapter 2

The Nonlinear Matter Correlation Function

2.1 Introduction

The Baryon Acoustic Oscillation (BAO) signal, which was imprinted on the 2-point statistics of matter in the early Universe, provides us a way to measure the dynamics of dark energy. As was discussed in Section 1.2, BAOs arose from photon pressure opposing the gravitational collapse of baryonic density perturbations in the baryon-photon plasma before the epoch of recombination (Peebles & Yu 1970; Silk 1968; Sunyaev & Zel'dovich 1970; Bond & Efstathiou 1984). We see the signature of this effect in both the temperature power spectrum of the cosmic microwave background (CMB) (de Bernardis et al. 2000; Hanany et al. 2000), and the galaxy 2-point

statistics. The BAO feature was first detected as a peak in the correlation function of the Luminous Red Galaxies (LRGs) in the Sloan Digital Sky Survey (SDSS) by Eisenstein et al. (2005), and was subsequently measured in many other galaxy surveys (Cole et al. 2005; Padmanabhan et al. 2007; Percival et al. 2007, 2010; Blake et al. 2011b).

The BAO signal is useful because even at low redshift, the scale of interest is still largely in the linear regime. The location of the peak thus acts as a "standard ruler" with which we can measure the expansion history of the Universe over time. This allows us to constrain the equation of state of dark energy (Seo & Eisenstein 2003).

As shown in Section 1.3.2, linear theory predicts that the amplitude of the peak will scale as the square of the linear growth function, $D(t)$. However, at low redshift, nonlinear evolution alters the location and shape of the peak on the order of about 1%. The effects of nonlinear evolution can be modeled most accurately using N-body simulations, although these can be computationally expensive. A more efficient method is using a perturbative approach to gravitational dynamics (Crocce & Scoccimarro 2008a). It is also well known that there are first order effects on the correlation function due to the transformation from real to redshift space (Kaiser 1987; Fry & Gaztanaga 1994; Tian et al. 2011; Blake et al. 2011a; Seo et al. 2012), but the effects on higher-order terms are less clear. As observations of the BAO signal reach the sub-percent level, understanding the effects of both nonlinear gravitational evolution and redshift-space distortions on the acoustic peak has become increasingly

important.

Much work has been done to characterize the nonlinear power spectrum using Standard Perturbation Theory in real space (Jain & Bertschinger 1994; Bouchet et al. 1995; Bernardeau et al. 2002; Crocce & Scoccimarro 2006, 2008a; Matsubara 2008b), and in redshift space (Matsubara 2008a; Taruya et al. 2010; Valageas 2011). This work has almost exclusively focused on Fourier space. However, there are some advantages to working in configuration space as opposed to Fourier space. First, the survey window function has a more natural representation in configuration space as opposed to Fourier space. Second, the transformation to redshift space is more straightforward to model. Lastly, the Fourier-space kernels (such as Equations 1.25 and 1.26) suggest that a configuration-space representation may be mathematically simpler, involving products as opposed to convolutions.

In this Chapter, we present a method of calculating the first nonlinear term in the correlation function using the Zel'dovich approximation. In Section 2.2, we show how to carry out the calculation in real space. In Section 2.3, we show how the approach can be extended to redshift space. We conclude in Section 2.4.

2.2 Real-space Correlation Function

In this Section, we compute the nonlinear correlation function in real-space from the Zel'dovich approximation. Then, in Section 2.2.2, we show that our expression is

the exact Fourier transform of the nonlinear Zel'dovich power spectrum. We directly compare our calculation to the expression for the nonlinear Zel'dovich power spectrum, originally calculated in Grinstein & Wise (1987), and more recently in Valageas (2011). We show in Section 2.2.3 that our configuration-space term is in agreement with numerical simulations of the Zel'dovich approximation.

2.2.1 Theory

The Zel'dovich approximation maps particles' initial Lagrangian coordinate, $\mathbf{q}$, to their co-moving Eulerian coordinate, $\mathbf{x}$, through the gradient of the linear potential, $\phi(\mathbf{q})$, and the growth function $D(t)$ (Zel'dovich 1970; Shandarin & Zeldovich 1989). The linear potential is related to the linear (Gaussian) density field through the Poisson equation:

$$\mathbf{x}(\mathbf{q},t) = \mathbf{q} - D(t)\nabla_q\phi(\mathbf{q}) \ , \tag{2.1}$$

$$D(t)\nabla_q^2\phi(\mathbf{q}) = \delta_L(\mathbf{q},t) \ .$$

The real-space density is then related to the Jacobian of the transformation from Lagrangian to Eulerian coordinates.

$$\frac{\rho(\mathbf{x},t)}{\bar{\rho}} = \left|\frac{\partial x_i}{\partial q_j}\right|^{-1} = \frac{1}{J(\mathbf{q},t)} = 1 + \delta(\mathbf{q}(\mathbf{x})) \ , \tag{2.2}$$

where $\mathbf{x}$ and $\mathbf{q}$ are related by the Zel'dovich formula (2.1). Here, δ (without subscript L) is the *weakly nonlinear* over-density. Equation (2.2) for the Eulerian density is only strictly valid before shell-crossing, where the mapping from $\mathbf{q}$ to $\mathbf{x}$ is one-to-one. As

is discussed in Kofman et al. (1994), when there is multi-streaming, multiple values of $\mathbf{q} = \mathbf{q}_i$ map to the same point $\mathbf{x}$, thus the Eulerian density at a given point is a sum over all of the streams at that point.

$$\rho(\mathbf{x}) = \sum_{i=1}^{N_{\mathbf{streams(x)}}} \varrho(\mathbf{q}_i(\mathbf{x})) \ . \tag{2.3}$$

Here, $\rho(\mathbf{x})$ is the full Eulerian density, and $\varrho(\mathbf{q}_i)$ are the "single-stream" densities. However, shell-crossing does not contribute greatly at the large scales we are concerned with, and so we assume the "single-stream" density is the full density. We will show that this assumption leads to a result that agrees with the usual perturbative results.

The Jacobian can be written in terms of invariants, I_1, I_2, and I_3, of the symmetric matrix $d_{ij}(\mathbf{q})$, called the deformation tensor (Zel'dovich 1970):

$$d_{ij}(\mathbf{q}) = \frac{\partial^2 \phi(\mathbf{q})}{\partial q_i \partial q_j} \ , \tag{2.4}$$

$$J(\mathbf{q}, t) = 1 - DI_1(\mathbf{q}) + D^2 I_2(\mathbf{q}) - D^3 I_3(\mathbf{q}) \ . \tag{2.5}$$

The invariants can be written in terms of the eigenvalues of $d_{ij}(\mathbf{q})$: λ_1, λ_2, and λ_3.

$$\begin{aligned} I_1(\mathbf{q}) &= \lambda_1 + \lambda_2 + \lambda_3 \ , \\ I_2(\mathbf{q}) &= \lambda_1\lambda_2 + \lambda_1\lambda_3 + \lambda_2\lambda_3 \ , \\ I_3(\mathbf{q}) &= \lambda_1\lambda_2\lambda_3 \ . \end{aligned} \tag{2.6}$$

From Equation 2.2, the Eulerian overdensity can be expressed by the Taylor expansion

of the inverse Jacobian, to any order:

$$\delta(\mathbf{q},t) = DI_1(\mathbf{q}) + D^2\left(I_1(\mathbf{q})^2 - I_2(\mathbf{q})\right) + D^3\left(I_1(\mathbf{q})^3 - 2I_1(\mathbf{q})I_2(\mathbf{q}) + I_3(\mathbf{q})\right) + ... \tag{2.7}$$

Note that the first term in this expansion corresponds to linear theory: $\delta_L = DI_1(\mathbf{q})$.

However, as our goal in this paper is to calculate the density correlation function at a fixed (comoving) Eulerian distance, we need to be careful about the details of the difference between the Eulerian and Lagrangian coordinates. Instead of the usual forward relation, writing $\mathbf{x}$ in terms of $\mathbf{q}$, we will need the reverse and express $\mathbf{q}$ with $\mathbf{x}$, using the Taylor expansion around $\mathbf{x}$ in a recursive fashion.

$$\mathbf{q}(\mathbf{x}) = \mathbf{x} + D\,\nabla_q\phi(\mathbf{q}(\mathbf{x}))\ . \tag{2.8}$$

To zeroth order, $\nabla_q\phi(\mathbf{q}(\mathbf{x})) = \nabla_q\phi(\mathbf{x})$, but when considering the higher order terms in the density, it is necessary to express $\nabla_q\phi(\mathbf{q}(\mathbf{x}))$ to linear order in D.

$$\frac{\partial\phi(\mathbf{x}(\mathbf{q}))}{\partial q_i} = \left(\frac{\partial\phi(\mathbf{q})}{\partial q_i} + D\sum_j \frac{\partial^2\phi(\mathbf{q})}{\partial q_i\partial q_j}\frac{\partial\phi(\mathbf{q})}{\partial q_j}\right)\Bigg|_{\mathbf{q}=\mathbf{x}}\ . \tag{2.9}$$

By expanding the function $\delta(\mathbf{q})$ about the point $\mathbf{q} = \mathbf{x}$, we arrive at an expression for $\delta(\mathbf{x})$ that is a power series in D.

$$\delta(\mathbf{x},t) = \delta\left(\mathbf{x} + D\nabla_q\phi(\mathbf{q}(\mathbf{x}))\right)\ . \tag{2.10}$$

A Taylor expansion of the right hand side of Equation (2.10) gives:

$$\delta(\mathbf{x},t) = \left(\delta(\mathbf{q},t) + D\sum_i \frac{\partial\phi(\mathbf{q}(\mathbf{x}))}{\partial q_i}\frac{\partial\delta(\mathbf{q},t)}{\partial q_i} + \frac{1}{2}D^2\sum_{i,j}\frac{\partial^2\delta(\mathbf{q},t)}{\partial q_i\partial q_j}\frac{\partial\phi(\mathbf{q})}{\partial q_i}\frac{\partial\phi(\mathbf{q})}{\partial q_j}\right)\Bigg|_{\mathbf{q}=\mathbf{x}}\ . \tag{2.11}$$

With this, we can write the Eulerian density in terms of the Lagrangian density to third order in D:

$$\delta(\mathbf{x},t) = \left(\delta(\mathbf{q},t) + D\sum_i \frac{\partial\phi(\mathbf{q})}{\partial q_i}\frac{\partial\delta(\mathbf{q},t)}{\partial q_i} + D^2\sum_{i,j}\frac{\partial^2\phi(\mathbf{q})}{\partial q_i\partial q_j}\frac{\partial\phi(\mathbf{q})}{\partial q_j}\frac{\partial\delta(\mathbf{q},t)}{\partial q_i} + \frac{1}{2}D^2\sum_{i,j}\frac{\partial^2\delta(\mathbf{q},t)}{\partial q_i\partial q_j}\frac{\partial\phi(\mathbf{q})}{\partial q_i}\frac{\partial\phi(\mathbf{q})}{\partial q_j}\right)\Bigg|_{\mathbf{q}=\mathbf{x}} . \tag{2.12}$$

We use Equation (2.7) to express δ in terms of the linear quantities δ_L and ϕ, where δ_L is already first order in D.

The real-space correlation function in co-moving Eulerian coordinates is:

$$\xi(\mathbf{x}_1 - \mathbf{x}_2, t) = \langle\delta(\mathbf{x}_1,t)\delta(\mathbf{x}_2,t)\rangle \ . \tag{2.13}$$

This can be written in powers of D using the above expansion of the Eulerian over-density. Because the over-density field is assumed to be a zero-mean Gaussian random field, the odd moments vanish. The correlation function to second order is then:

$$\xi(\mathbf{r},t) = \xi^{(1)}(\mathbf{r})D^2 + \xi^{(2)}(\mathbf{r})D^4 + ...$$

We define the functions:

$$\xi_n^m(r) = \frac{1}{2\pi^2}\int_0^\infty P_L(k)j_n(kr)k^{m+2}\mathrm{d}k \ , \tag{2.14}$$

where j_n is the spherical Bessel function of order n and $P_L(k)$ is the linear power spectrum. Using this definition, the linear term is:

$$\xi^{(1)}(\mathbf{r}) = \xi_0^0(r) \ , \tag{2.15}$$

the spherically symmetric Fourier transform of the linear power spectrum.

$\xi^{(2)}(\mathbf{r})$ is the expectation of a sum of products of four terms expressed with the linear quantities. Since these are all Gaussian, the only irreducible terms are second order. Thus we only need to calculate expectations of the type $\langle a(\mathbf{q}_1)b(\mathbf{q}_2)\rangle$. Mathematica was used to express the various derivatives of $\phi(\mathbf{q})$ in terms of spherical harmonics, and to calculate the expectation values between them. We illustrate this process in the following example.

To calculate the expectation value $\left\langle \frac{\partial\phi(\mathbf{q}_1)}{\partial q_z}\frac{\partial^2\phi(\mathbf{q}_2)}{\partial q_z^2}\right\rangle$, we first express each term as a Fourier-space integral and expand the angular part in spherical harmonics:

$$\frac{\partial\phi(\mathbf{q})}{\partial q_z} = -\int\frac{\mathrm{d}^3k}{(2\pi)^3}\frac{ik_z}{k^2}\hat{\delta}_L(\mathbf{k})e^{i\mathbf{k}\cdot\mathbf{q}} = -i\sqrt{\frac{4\pi}{3}}\int\frac{\mathrm{d}^3k}{(2\pi)^3}\frac{Y_1^0(\hat{k})}{k}\hat{\delta}_L(\mathbf{k})e^{i\mathbf{k}\cdot\mathbf{q}}\ , \tag{2.16}$$

$$\begin{aligned}\frac{\partial^2\phi(\mathbf{q})}{\partial q_z^2} &= \int\frac{\mathrm{d}^3k}{(2\pi)^3}\frac{k_z^2}{k^2}\hat{\delta}_L(\mathbf{k})e^{i\mathbf{k}\cdot\mathbf{q}} \\ &= \frac{\sqrt{4\pi}}{3}\int\frac{\mathrm{d}^3k}{(2\pi)^3}\left(Y_0^0(\hat{k}) + \frac{2Y_2^0(\hat{k})}{\sqrt{5}}\right)\hat{\delta}_L(\mathbf{k})e^{i\mathbf{k}\cdot\mathbf{q}}\ .\end{aligned} \tag{2.17}$$

The expectation value can then be written as:

$$\begin{aligned}\left\langle \frac{\partial\phi(\mathbf{q}_1)}{\partial q_z}\frac{\partial^2\phi(\mathbf{q}_2)}{\partial q_z^2}\right\rangle = -\frac{4\pi i}{3^{3/2}(2\pi)^6}\iint\mathrm{d}^3k_1\mathrm{d}^3k_2e^{i(\mathbf{k}_1\cdot\mathbf{q}_1+\mathbf{k}_2\cdot\mathbf{q}_2)}\frac{\langle\hat{\delta}_L(\mathbf{k}_1)\hat{\delta}_L(\mathbf{k}_2)\rangle}{k}\ , \\ \times\ Y_1^0(\theta_1,\varphi_1)\left(Y_0^0(\theta_2,\varphi_2) + \frac{2}{\sqrt{5}}Y_2^0(\theta_2,\varphi_2)\right)\ .\end{aligned} \tag{2.18}$$

This simplifies using the definition of the linear power spectrum:

$$\langle\hat{\delta}_L(\mathbf{k}_1)\hat{\delta}_L(\mathbf{k}_2)\rangle = (2\pi)^3\delta_D(\mathbf{k}_1+\mathbf{k}_2)P_L(k_1)\ . \tag{2.19}$$

To evaluate the integral in Equation 2.18, we must calculate the integrals:

$$\int Y_l^m(\theta,\varphi)Y_{l'}^{*m'}(\theta,\varphi)e^{i\mathbf{k}\cdot(\mathbf{q}_1-\mathbf{q}_2)}\mathrm{d}\Omega_k\ . \tag{2.20}$$

We use the plane-wave (Rayleigh) expansion for $e^{i\mathbf{k}\cdot(\mathbf{q}_1-\mathbf{q}_2)}$ to compute these integrals in terms of spherical Bessel functions, $j_n(kr)$, where $\mathbf{r} = \mathbf{q}_1 - \mathbf{q}_2$. In general, the integral is zero for $m \neq m'$, because we assume that $\mathbf{r}$ is along the $\hat{z}$ direction, and $\mathbf{r}\cdot\mathbf{k} = rk\cos\theta$.

$$\begin{aligned}\left\langle \frac{\partial\phi(\mathbf{q}_1)}{\partial q_z}\frac{\partial^2\phi(\mathbf{q}_2)}{\partial q_z^2}\right\rangle &= -\frac{1}{5(2\pi^2)}\int_0^\infty P_L(k)\left(3j_1(kr)\mathcal{P}_1(\mu) - 2j_3(kr)\mathcal{P}_3(\mu)\right)k\,\mathrm{d}k\ , \\ &= -\frac{3}{5}\mathcal{P}_1(\mu)\xi_1^{-1}(r) + \frac{2}{5}\mathcal{P}_3(\mu)\xi_3^{-1}(r)\ . \end{aligned} \tag{2.21}$$

where μ is the cosine of the angle between $\hat{r}$ and $\hat{z}$, and $\mathcal{P}_l(\mu)$ are the Legendre polynomials. In the expansion of the over-density, Equation (2.12), each term is evaluated at $\mathbf{q} = \mathbf{x}$, so the expectation values in the correlation function become functions of the Eulerian distance, $r = |\mathbf{x}_1 - \mathbf{x}_2|$.

In the full calculation, there are many seemingly serendipitous cancellations of terms, which in the end give us a relatively simple expression. As we found, any small mistake in the Mathematica script can lead to a far more complicated expression with the wrong asymptotics, so it is important to understand the expected behavior of the full correlation function to check the result. Firstly, the expectation value of the over-density should vanish to second order. Secondly, the correlation function should be isotropic in real space. Finally, we consider the asymptotic behavior of the expression – at zero lag, it must be finite, as this is the variance of the over-density field, and on large scales, the expression must tend to zero. Requiring this behavior rules out many erroneous results, and was a useful debugging tool.

The full expression for the first nonlinear term of the Zel'dovich correlation function in comoving Eulerian coordinates is:

$$\xi^{(2)}(\mathbf{r}) = -\frac{1}{3}\xi_0^{-2}(0)\xi_0^2(r) + \frac{19}{15}\xi_0^0(r)^2 + \frac{34}{21}\xi_2^0(r)^2 + \frac{4}{35}\xi_4^0(r)^2 - \frac{16}{5}\xi_1^{-1}(r)\xi_1^1(r) - \frac{4}{5}\xi_3^{-1}(r)\xi_3^1(r) + \frac{1}{3}\xi_0^{-2}(r)\xi_0^2(r) + \frac{2}{3}\xi_2^{-2}(r)\xi_2^2(r) \ . \tag{2.22}$$

At zero lag, this takes the value:

$$\xi^{(2)}(0) = \frac{19}{15}\xi_0^0(0)^2 = \frac{19}{15}\sigma_0^4 \ . \tag{2.23}$$

where σ_0^2 is the variance of the linear over-density field. As expected, the nonlinear term is finite at $r = 0$. As $r \to \infty$, each set of terms within the expression tends to zero, due to the behavior of the spherical Bessel functions, so the full expression tends to zero as expected. Note that this expression contains products of the functions $\xi_n^m(r)$. In the next section, we show that this is the exact Fourier transform of the nonlinear Zel'dovich power spectrum.

2.2.2 Comparison to Power Spectrum

The nonlinear Zel'dovich power spectrum can be found in Grinstein & Wise (1987) and Valageas (2011). Here, we show that our expression, Equation 2.22, is the exact Fourier transform of these previous results.

Using our Fourier conventions, the first nonlinear term in the Zel'dovich power

spectrum is:

$$P^{(2)}(k) = P_{13}(k) + P_{22}(k) \tag{2.24}$$
$$= -k^2\sigma_v^2 P_L(k) + \iint \frac{\mathrm{d}^3k_1\mathrm{d}^3k_2}{(2\pi)^3}\delta_D(\mathbf{k}-\mathbf{k}_1-\mathbf{k}_2)\frac{(\mathbf{k}\cdot\mathbf{k}_1)^2(\mathbf{k}\cdot\mathbf{k}_2)^2}{2k_1^4k_2^4}P_L(k_1)P_L(k_2)\ ,$$
$$\sigma_v^2 = \frac{1}{6\pi^2}\int_0^\infty P_L(w)\mathrm{d}w\ .$$

We group Equation (2.22) into two terms, in order to clearly relate it to $P_{13}(k)$ and $P_{22}(k)$:

$$\xi^{(2)}(r) = \xi_{(13)}(r) + \xi_{(22)}(r)\ , \tag{2.25}$$

where $\xi_{(13)}(r)$ is defined as the first term in Equation (2.22), and $\xi_{(22)}(r)$ contains the remaining terms. The term $\xi_{(13)}(r)$ straightforwardly Fourier transforms to $P_{13}(k)$:

$$\mathcal{F}\left\{-\frac{1}{3}\xi_0^{-2}(0)\xi_0^2(r)\right\} = -\frac{(4\pi)^2}{3(2\pi)^3}\xi_0^{-2}(0)\int_0^\infty\int_0^\infty P_L(k')k'^4 j_0(k'r)j_0(kr)r^2\mathrm{d}k'\mathrm{d}r \tag{2.26}$$
$$= -\frac{2}{3\pi}\xi_0^{-2}(0)\int_0^\infty P_L(k')k'^4\frac{\pi}{2k'^2}\delta_D(k-k')\mathrm{d}k'$$
$$= -\frac{1}{3}\xi_0^{-2}(0)k^2P_L(k)\ .$$

This is equal to $P_{13}(k)$ from Equation (2.24):

$$P_{13}(k) = -k^2\sigma_v^2P_L(k) = -\frac{1}{3}\xi_0^{-2}(0)k^2P_L(k)\ . \tag{2.27}$$

The Fourier transform of $\xi_{(22)}(r)$ contains integrals of three spherical Bessel functions. In general:

$$\mathcal{F}\{\xi_n^{m_1}(r)\xi_n^{m_2}(r)\} = \frac{1}{\pi^3}\int_0^\infty\int_0^\infty\left(\int_0^\infty j_n(k_1r)j_n(k_2r)j_0(kr)r^2\mathrm{d}r\right)$$
$$\times\ P_L(k_1)P_L(k_2)k_1^{m_1+2}k_2^{m_2+2}\mathrm{d}k_1\mathrm{d}k_2\ . \tag{2.28}$$

We require the expressions for integrals of the type

$$\int_0^\infty j_0(kr) j_n(k_1 r) j_n(k_2 r) r^2 \mathrm{d}r, \tag{2.29}$$

which can be found in Mehrem et al. (1991).

For example, to compute $\mathcal{F}\{\xi_2^0(r)^2\}$, we need to evaluate the following integral:

$$\int_0^\infty j_2(k_1 r) j_2(k_2 r) j_0(kr) r^2 \mathrm{d}r = \frac{\pi \beta(k_1, k_2, k)}{32 k k_1^3 k_2^3} \left(3(k_2^2 + k_1^2 - k^2)^2 - 4k_1^2 k_2^2\right) \ , \tag{2.30}$$

$$\beta(k_1, k_2, k) = \begin{cases} 1 & |k_1 - k_2| < k < k_1 + k_2 \\ \frac{1}{2} & |k_1 - k_2| = k \ \ or \ k_1 + k_2 = k \\ 0 & \text{otherwise} \end{cases} .$$

This means that the integral is zero unless $\mathbf{k}$, $\mathbf{k}_1$, and $\mathbf{k}_2$ form a triangle. In the k_1 k_2 plane, we consider the region where this triangular condition is satisfied. On the boundary of that region, the Bessel integral is discontinuous. However, since the boundary has measure zero, it does not contribute to the integral. Thus, we consider only the inside of the region of the plane where $\mathbf{k}$, $\mathbf{k}_1$, and $\mathbf{k}_2$ form a triangle, i.e. where $\beta = 1$.

In the integral, we make the substitution $k_2 = |\mathbf{k} - \mathbf{k}_1|$, and integrate over the angle θ between $\mathbf{k}$ and $\mathbf{k}_1$.

$$\mathcal{F}\{\xi_2^0(r)^2\} = \frac{1}{64\pi^3}\int \mathrm{d}^3k_1 P_L(k_1)P_L(|\mathbf{k}-\mathbf{k}_1|)\frac{3((\mathbf{k}-\mathbf{k}_1)^2+k_1^2-k^2)^2-4k_1^2(\mathbf{k}-\mathbf{k}_1)^2}{k_1^2|\mathbf{k}-\mathbf{k}_1|^2}$$
$$= \frac{1}{4(2\pi)^3}\iint \mathrm{d}^3k_1\mathrm{d}^3k_2 P_L(k_1)P_L(k_2)\delta_D(\mathbf{k}-\mathbf{k}_1-\mathbf{k}_2)\frac{3(\mathbf{k}_1\cdot\mathbf{k}_2)^2-2k_1^2k_2^2}{k_1^2k_2^2}\ . \tag{2.31}$$

This illustrates how the products of two $\xi_n^m(r)$ in configuration space correspond to a convolution in Fourier space.

The Fourier transform of all the terms in $\xi_{(22)}(r)$ is:

$$\mathcal{F}\{\xi_{(22)}(r)\} = \iint \frac{\mathrm{d}^3k_1\mathrm{d}^3k_2}{(2\pi)^3}\delta_D(\mathbf{k}-\mathbf{k}_1-\mathbf{k}_2)\frac{(\mathbf{k}\cdot\mathbf{k}_1)^2(\mathbf{k}\cdot\mathbf{k}_2)^2}{2k_1^4k_2^4}P_L(k_1)P_L(k_2)\ . \tag{2.32}$$

which is exactly the $P_{22}(k)$ term from Equation (2.24). Thus, the entire expression transforms to $P^{(2)}(k)$.

This agreement validates our configuration-space approach to perturbation theory with the Zel'dovich approximation. It is also remarkable how the triangular closure of the three wave vectors is connected to the integral over three spherical Bessel functions.

2.2.3 Discussion

Our goal is to understand the effects of nonlinearities on the baryon acoustic peak in the correlation function. We have shown that we can derive an expression for the first nonlinear term in configuration space from the Zel'dovich approximation. For the real-space correlation function, we are able to check our analytical expression against

the Zel'dovich power spectrum from Grinstein & Wise (1987) and Valageas (2011), which is calculated using an entirely different technique. This provides analytical validation of our configuration-space approach to perturbation theory.

However, in Section 2.3, we will extend this calculation to redshift space, and eventually we may want to extend it to higher orders. For these applications, the Fourier equivalents do not exist, so we have no analytical validation of the results. Therefore, we need a numerical method that can be used to test these future results. Here, we present the results from a set of Zel'dovich simulations, and show that they validate our configuration-space result, and can therefore be used to test future analytical results in redshift space and at higher orders.

A set of 100 Zel'dovich simulations, written in Python, was run using CAMB (Lewis et al. 2000) to generate the initial power spectrum. We used the cosmological parameters $\Omega_\Lambda = 0.71$, $\Omega_m = 0.29$, $\Omega_b = 0.045$, $h = 0.7$, and $\sigma_8(z = 0) = 0.89$. Each simulation was a 1 Gpc/h box with 512^3 particles, and a cell length of 3.9 Mpc/h. We computed the density at 4 different redshifts in each simulation from $z = 10$ and $z = 0$ using a cloud-in-cell interpolation scheme. The density was then used to compute the correlation function at each time step. The average of the correlation functions over the 100 simulations allows us to see the behavior of the nonlinear term over time.

We expect the results from the simulations to agree with the analytical expression at high redshift, although the result will be noisy due to the small value of the

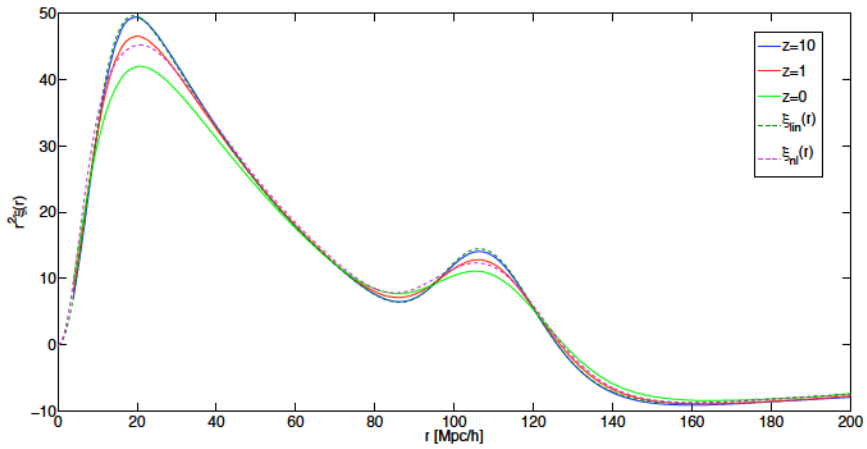

Figure 2.1: The nonlinear correlation function measured from Zel'dovich simulations compared to the analytic expression for the 2nd order correlation function. The dashed lines represent the theoretical predictions for the linear (dark green) and nonlinear (purple) correlation functions at z=0 from the Zel'dovich approximation. The solid lines are the correlation functions, normalized by D^2, measured from 100 Zel'dovich realizations. At $z = 10$, there is good agreement with linear theory. At $z = 1$ the behavior of the peak is well-described by the nonlinear correlation function. At $z = 0$ the first nonlinear term is not sufficient to describe the deviation from linear theory, as higher order terms become non-negligible.

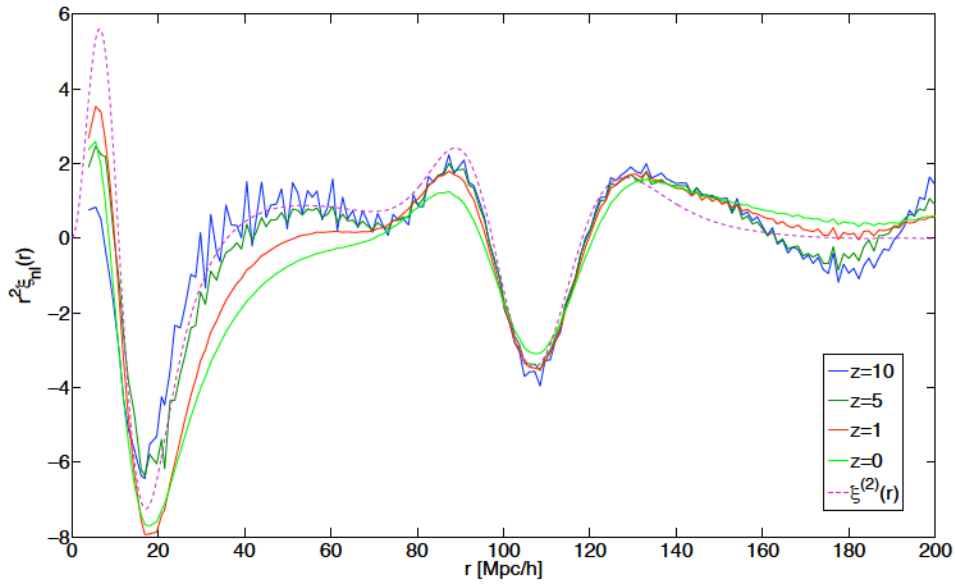

Figure 2.2: The nonlinear contribution to the correlation function. The dashed line represents the analytic expression for the nonlinear term from the Zel'dovich approximation. The solid lines are the nonlinear term from Zel'dovich simulations, averaged over 100 realizations. At $z = 10, 5$, and 1 there is good agreement with the analytical prediction. At $z = 0$, higher order terms have a non-negligible effect.

nonlinear contribution at early times. There will be a growing deviation from the analytical result with decreasing redshift coming from the next higher order term, proportional to D^6. At $z = 1$, this higher order term will be smaller than 1% of the value at the acoustic peak. At $z = 0$, however, this term will cause a deviation on the order of 5% at the BAO scale, and thus we do not expect the analytical expression to approximate well the behavior at $z = 0$. This is similar to the results from 1-loop standard perturbation theory as compared to N-body simulations (Matsubara 2008b), where the higher order terms have the greatest contribution at low redshift.

Figure 2.1 shows the averaged correlation functions at redshifts 10, 1, and 0, normalized by D^2 for comparison. We compare these to the theoretical predictions from the Zel'dovich approximation for the linear and nonlinear correlation functions at $z = 0$. At $z = 10$, the correlation function is well-approximated by linear theory. At $z = 1$, the behavior of the peak is closer to that of the nonlinear correlation function. At $z = 0$, higher order terms become non-negligible, so the first nonlinear term is not sufficient to fully describe the correlation function. As expected from perturbation theory, the acoustic peak is noticeably dampened at later times.

Figure 2.2 shows only the nonlinear contribution to the correlation function at $z = 10$, $z = 5$, $z = 1$, and $z = 0$, again normalized by D^2 for comparison. We also show the prediction from perturbation theory for the nonlinear term. There is overall agreement with theory at scales larger than about 20 Mpc/h. Below this scale, we are limited by the resolution of our simulation. At scales greater than about 140 Mpc/h,

we see deviation in the nonlinear term from the theoretical prediction. We believe that this is also an artifact of the simulation, related to aliasing of the particle window function. The deviation is amplified in this figure due to the multiplication with a very large value of r^2. On the scale of the acoustic peak, there is good agreement between the analytical expression and the simulations. At $z = 0$ we again see that the first nonlinear term is not sufficient to accurately describe the peak, because the higher order terms become non-negligible.

2.3 Redshift-space Correlation Function

We now extend the approach outlined in Section 2.2.1 into redshift space. In Section 2.3.1, we show how the calculation is done analytically. We compare our result to numerical simulations in Section 2.3.2.

2.3.1 Theory

In Section 2.2.1, we used the mapping from particles' initial Lagrangian coordinate, $\mathbf{q}$, and their co-moving Eulerian coordinate, $\mathbf{x}$, to compute the nonlinear correlation function in real space. Now, we can use the same approach to compute the expression in redshift space.

As discussed in Section 1.3.4, to a distant observer, the redshift coordinate $\mathbf{s}$ is related to the Eulerian coordinate $\mathbf{x}$ through the particle's peculiar velocity along the

line of sight:

$$\mathbf{s}(\mathbf{x}) = \mathbf{x} - f v_z(\mathbf{x}) \hat{n}, \tag{2.33}$$

where $\hat{n}$ is the line-of-sight direction, and f is the logarithmic derivative of the growth function, D, and v_z is related to the peculiar velocity ($\mathbf{u}(\mathbf{x})$) along the line of sight: $v_z(\mathbf{x}) \equiv -u_z(\mathbf{x})/(Haf)$ (see Hamilton (1998) for a review).

Combining Equation 2.33 with the Zel'dovich Approximation (Equation 2.1), we can write the transformation from Lagrangian to redshift coordinates:

$$\mathbf{s}(\mathbf{q}) = \mathbf{q} + \mathbf{\Psi}(\mathbf{q}, t) \ , \tag{2.34}$$

$$\mathbf{\Psi}(\mathbf{q}, t) \equiv -D(t) \left(\nabla_q \phi(\mathbf{q}) + f (\nabla_q \phi(\mathbf{q}) \cdot \hat{n}) \hat{n} \right) \ .$$

We now follow the same approach outlined in Section 2.2.1 to calculate the non-linear overdensity, but using the anisotropic displacement field, $\mathbf{\Psi}$. Mass conservation allows us to relate the initial Gaussian overdensity to the final redshift-space over-density through the Jacobian of the transformation in Equation (2.34):

$$\frac{\rho(\mathbf{s}, t)}{\bar{\rho}} = \left| \frac{\partial s_i}{\partial q_j} \right|^{-1} = \frac{1}{J(\mathbf{q}, t)} = 1 + \delta(\mathbf{q}(\mathbf{s})) \ , \tag{2.35}$$

where $\mathbf{s}$ and $\mathbf{q}$ are related by Equation (2.34). Here, δ (without subscript L) is the over-density in redshift space, expressed through the Lagrangian coordinate $\mathbf{q}$.

The Jacobian of this transformation can be written in terms of f and elements of

the deformation tensor $d_{ij}(\mathbf{q})$:

$$J(\mathbf{q},t) = 1 - D(I_1(\mathbf{q}) + f d_{nn}(\mathbf{q})) + D^2\left((1+f)I_2(\mathbf{q}) - f M_{nn}(\mathbf{q})\right) - D^3(1+f)I_3(\mathbf{q}) \ , \tag{2.36}$$

where d_{nn} is the line-of-sight component of d_{ij}, M_{nn} is the corresponding minor of the matrix, and I_1, I_2, and I_3 are the invariants of d_{ij}, as described in Section 2.2.1.

Again, we want to express the overdensity in terms of the redshift coordinate, rather than the Lagrangian coordinate, because we want the expression for the correlation function in terms of the observed redshift-space separation, $\mathbf{s}_1 - \mathbf{s}_2$. To do this, we invert Equation (2.34):

$$\mathbf{q}(\mathbf{s}) = \mathbf{s} - \mathbf{\Psi}(\mathbf{q}(\mathbf{s}),t) \ , \tag{2.37}$$

and use Taylor expansions of relevant quantities about the point $\mathbf{q} = \mathbf{s}$. First, we express $\mathbf{\Psi}$ as a function of redshift coordinate:

$$\Psi_i(\mathbf{s}(\mathbf{q})) = \left(\Psi_i(\mathbf{q}) - \sum_j \frac{\partial \Psi_i(\mathbf{q},t)}{\partial q_j}\Psi_j(\mathbf{q},t) + ...\right)\Bigg|_{\mathbf{q}=\mathbf{s}} \ , \tag{2.38}$$

where, Ψ_i indicates the i-th component of $\mathbf{\Psi}$. Because $\mathbf{\Psi}$ is proportional to D, this expansion is a power series in D. Next we relate the over-density in redshift coordinates to that in Lagrangian coordinates:

$$\delta(\mathbf{s},t) \equiv \delta(\mathbf{q}(\mathbf{s}),t) = \delta(\mathbf{s} - \mathbf{\Psi}(\mathbf{q}(\mathbf{s}))) \ . \tag{2.39}$$

A Taylor expansion of the right hand side of Equation (2.39) gives:

$$\delta(\mathbf{s},t) = \left(\delta(\mathbf{q},t) - \sum_i \frac{\partial\delta(\mathbf{q})}{\partial q_i}\Psi_i(\mathbf{q}(\mathbf{s})) + \frac{1}{2}\sum_{i,j}\frac{\partial\delta(\mathbf{q})}{\partial q_i \partial q_j}\Psi_i(\mathbf{q}(\mathbf{s}))\Psi_j(\mathbf{q}(\mathbf{s})) + ...\right)\Bigg|_{\mathbf{q}=\mathbf{s}} . \tag{2.40}$$

The full expression for the redshift-space over-density in terms of the Lagrangian over-density to third order in D is:

$$\delta(\mathbf{s},t) = \left(\delta(\mathbf{q},t) - \sum_i \frac{\partial\delta(\mathbf{q},t)}{\partial q_i}\Psi_i(\mathbf{q}) + \sum_{i,j}\frac{\partial\delta(\mathbf{q},t)}{\partial q_i}\frac{\partial\Psi_i(\mathbf{q},t)}{\partial q_j}\Psi_j(\mathbf{q},t) + \frac{1}{2}\sum_{i,j}\frac{\partial^2\delta(\mathbf{q},t)}{\partial q_i \partial q_j}\Psi_i(\mathbf{q})\Psi_j(\mathbf{q}) + ...\right)\Bigg|_{\mathbf{q}=\mathbf{s}} . \tag{2.41}$$

In co-moving coordinates, the redshift-space correlation function is defined as:

$$\xi(\mathbf{s},t) \equiv \langle\delta(\mathbf{s}',t)\delta(\mathbf{s}'+\mathbf{s},t)\rangle \ . \tag{2.42}$$

This can be written as a power series in D, as in real space:

$$\xi(\mathbf{s},t) = D^2\xi^{(1)}(\mathbf{s},t) + D^4\xi^{(2)}(\mathbf{s},t) \ , \tag{2.43}$$

where the terms proportional to odd powers of D again vanish because δ_L is assumed to be a Gaussian random field.

As in real-space, the redshift-space correlation function can be written in terms of the linear correlation functions:

$$\xi_n^m(s) = \frac{1}{2\pi^2}\int_0^\infty P_L(k) j_n(ks) k^{m+2} dk \ . \tag{2.44}$$

The calculations of the expectation values in redshift space are very similar to those in real space, but now involve the anisotropic displacement vector. For example,

the expectation value between the line-of-sight component of the displacement vector and its line-of-sight derivative is:

$$\left\langle \Psi_n(\mathbf{s}_1)\frac{\partial\Psi_n(\mathbf{s}_2)}{\partial q_n}\right\rangle = (1+f)^2\left(\frac{2}{5}\mathcal{P}_3(\mu)\xi_3^{-1}(s) - \frac{3}{5}\mathcal{P}_1(\mu)\xi_1^{-1}(s)\right) . \tag{2.45}$$

This result is the same as we found in real space in Section 2.2.1, but now with an extra factor of $(1+f)^2$.

The linear redshift-space correlation function, $\xi^{(1)}(\mathbf{s})$, can be computed in this way:

$$\begin{aligned}\xi^{(1)}(s,\mu) = &\left(1+\frac{2f}{3}+\frac{f^2}{5}\right)\xi_0^0(s) \\ &-\left(\frac{4f}{3}+\frac{4f^2}{7}\right)\mathcal{P}_2(\mu)\xi_2^0(s) + \frac{8f^2}{35}\mathcal{P}_4(\mu)\xi_4^0(s) ,\end{aligned} \tag{2.46}$$

where $\mathcal{P}_\ell(\mu)$ is the Legendre polynomial of order ℓ. This is the configuration-space equivalent of the linear Kaiser formula (Kaiser 1986; Hamilton 1992; Hamilton & Culhane 1996).

As in real space, the first nonlinear term contains expectation values of four linear quantities, which simplifies to products of the functions $\xi_n^m(s)$ due to Wick's theorem. In redshift space, the term has additional dependence on f and μ, as expected. We have condensed the terms for convenience, and give the full expression in Appendix B.

$$\begin{aligned}\xi^{(2)}(s,\mu) = &\sigma_v^2\sum_{\ell=0}^{4} f^{\ell/2}B_\ell(f)\xi_\ell^2(r)\mathcal{P}_\ell(\mu) \\ &+\sum_{\ell=0}^{8}\sum_{n_1,n_2}^{6}\sum_{m=0}^{2} f^{\ell/2}A_{n_1,n_2}^{\ell,m}(f)\xi_{n_1}^m(s)\xi_{n_2}^{-m}(s)\mathcal{P}_\ell(\mu),\end{aligned} \tag{2.47}$$

where

$$\sigma_v^2 \equiv \frac{1}{6\pi^2}\int_0^\infty P_L(k)dk \ . \tag{2.48}$$

There are several interesting cases we can study using this expression. The azimuthally averaged correlation function, which uses a $\sin\theta \ d\theta$ weighting, picks out only the $\ell = 0$ terms from the anisotropic correlation function. This is due to the orthogonality of the Legendre polynomials. The linear contribution to the azimuthally averaged correlation function is $\bar{\xi}^{(1)}(s) = (1 + \frac{2}{3}f + \frac{1}{5}f^2)\xi_0^0(s)$. Using equation 2.47, we can easily compute the nonlinear contribution to the averaged correlation:

$$\begin{aligned}\bar{\xi}^{(2)}(s) = \sigma_v^2 B_0 \xi_0^2(r) + A_{00}^{00}\xi_0^0(s)^2 + A_{22}^{00}\xi_2^0(s)^2 \\ + A_{44}^{00}\xi_4^0(s)^2 + A_{11}^{01}\xi_1^1(s)\xi_1^{-1}(s) + A_{33}^{01}\xi_3^1(s)\xi_3^{-1}(s) \\ + A_{22}^{02}\xi_2^2(s)\xi_2^{-2}(s) \ .\end{aligned} \tag{2.49}$$

Similarly, the quadrupole term can be computed by choosing only the $\ell = 2$ terms, and so on. The B_ℓ and $A_{n_1,n_2}^{\ell,m}$ terms listed in Appendix B are grouped by multipole (ℓ).

2.3.2 Discussion

In Section 2.2.2, in order to verify our real-space result for the nonlinear correlation function, we were able to Fourier transform the expression and compare it with the previously calculated Fourier-space result. We then used a numerical simulation of

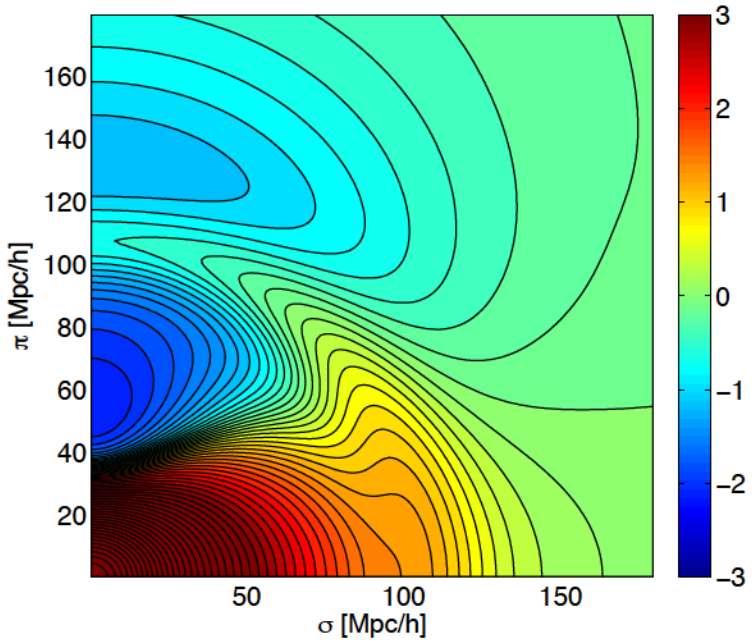

Figure 2.3: The two-dimensional linear correlation function in redshift space. We plot $\sinh^{-1}(500\xi^{(1)}(\mathrm{s}))$, which is linear near zero and logarithmic for high values of $\xi(\mathrm{s})$.

the Zel'dovich approximation whose results agreed with the analytical expression. We developed the numerical method in order to test other results, where analytical comparisons are not available to us, such as the redshift-space result presented in this Section. Here, we rely solely on these numerical simulations to verify the result.

We again use CAMB (Lewis et al. 2000) to generate the initial power spectrum, with the same cosmological parameters as before. Each simulation is a 1.5 Gpc/h box with 1024^3 particles. The particles are displaced from the initial grid to their redshift-space positions at $z = 10, 5, 1, 0$. We calculate the final redshift-space density using

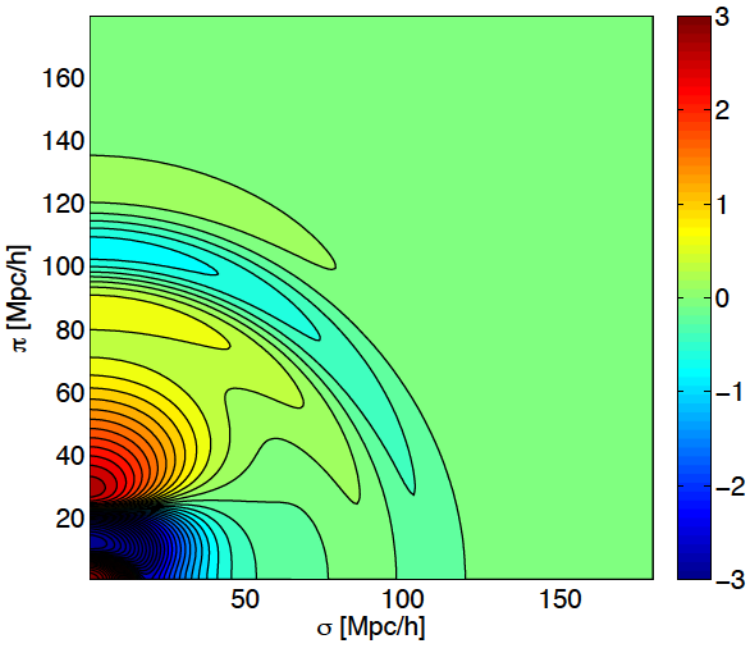

Figure 2.4: The first nonlinear term of the Zel'dovich correlation function in redshift space. Again, we plot $\sinh^{-1}(500\xi^{(2)}(\mathrm{s}))$ for clarity. Note that in this term, the BAO feature is negative (damped).

a cloud-in-cell scheme on a 256^3 grid, and this is used to compute the 2-dimensional correlation function using FFT. The average of the correlation functions over 1000 simulations at each redshift allows us to study the behavior of the correlation function over time. Because we do not average over the angle μ in redshift space as we do in real space, a larger box size and number of simulations are needed to sufficiently reduce the noise.

First, we consider the analytic prediction for the correlation function. Figure 2.3 shows the linear redshift-space correlation function, Equation (2.46). The x-axis is the transverse direction, and the y-axis is the line-of-sight direction. The BAO feature shows up as an anisotropic arc in the 2-dimensional redshift-space correlation function.

Figure 2.4 shows the prediction for the nonlinear term, Equation (2.47). The negative value along the BAO arc indicates that this term dampens the BAO feature. Along the line of sight, this term also tends to broaden the arc, due to the positive contribution on either side of the peak.

Next, we look at the results from the Zel'dovich simulations. To directly compare the simulations to our expression for the nonlinear term, we subtract off the linear term at each redshift and only look at the difference. Figure 2.5 shows the average nonlinear contribution to the correlation functions at redshifts $z = 10, 5, 1, 0$ from the Zel'dovich simulations. We have divided each by $D(z)^4$ so they are all on the same scale. Note that at high redshift, what is shown is the difference between two already

small values (the measured and linear correlation functions), divided by $D(z)^4$, which is also very small. Thus, the signal at high redshifts is noisier, even when averaged over 1000 simulations. Window function and discreteness effects are also amplified. At $z = 0$, where the nonlinear signal is larger, higher-order contributions become non-negligible, thus agreement with our theoretical expression is not guaranteed. At $z = 1$ we see the best agreement with our theoretical prediction, because the nonlinear term is larger, and higher-order terms are still small. We compare the results from the simulations at various redshifts in Figure 2.5 to the analytical expression in Figure 2.4. The shape of the nonlinear term matches fairly well to the analytical result at all redshifts. The damping of the BAO feature and broadening along the line of sight are clear.

To more easily compare the numerical results to the analytical expression, we can look at cuts of the correlation function along particular directions. Figure 2.6 shows the nonlinear terms from the simulations compared to the analytical expression along the line of sight ($\theta = 0$), a diagonal cut ($\theta = \pi/4$), and in the transverse direction ($\theta = \pi/2$). While these lines are relatively noisy, we can see that on the BAO scale the simulations agree with the analytical result in all three directions. On scales smaller than the BAO feature, we can see the growing contribution from the next higher order term, especially in the transverse and diagonal cuts. Due to the overall agreement between the numerical and analytical results, we conclude that our expression for the nonlinear term in redshift space is correct.

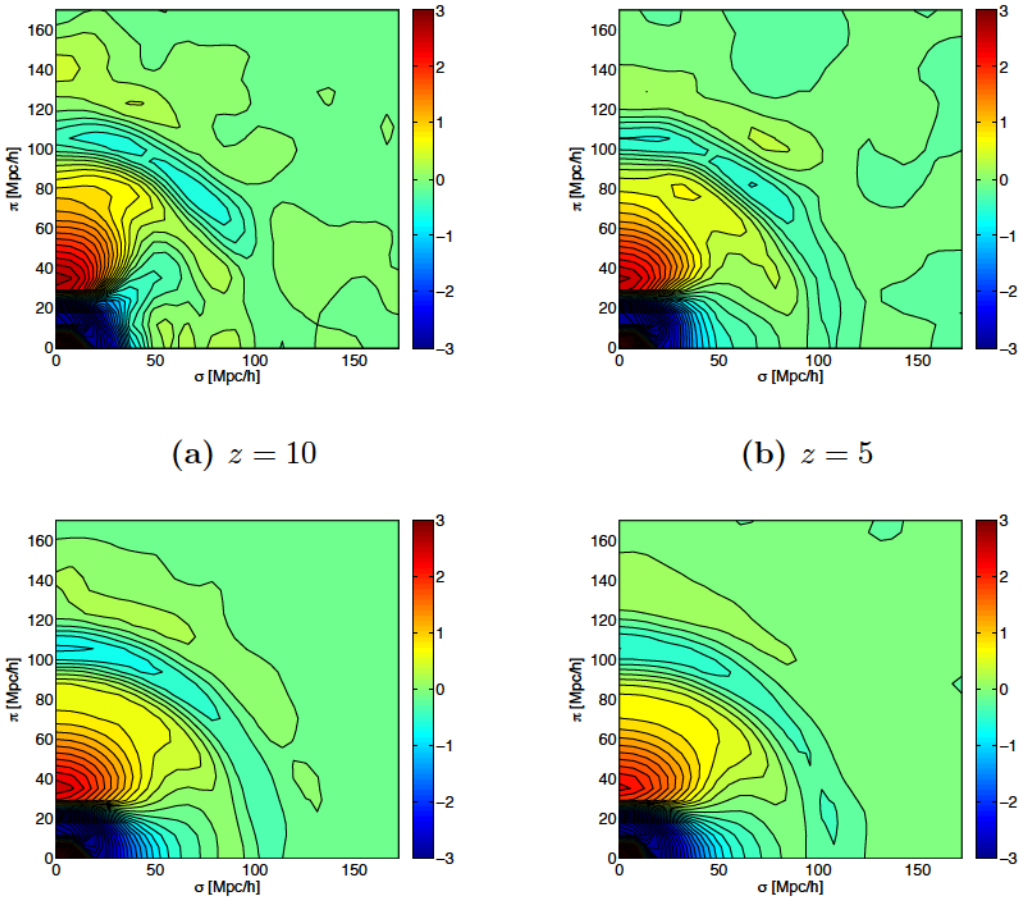

(a) $z = 10$ **(b)** $z = 5$

(c) $z = 1$ **(d)** $z = 0$

Figure 2.5: Nonlinear contributions to the correlation functions measured from 1000 Zel'dovich simulations, at $z = 10$ (top left), $z = 5$ (top right), $z = 1$ (bottom left), and $z = 0$ (bottom right).

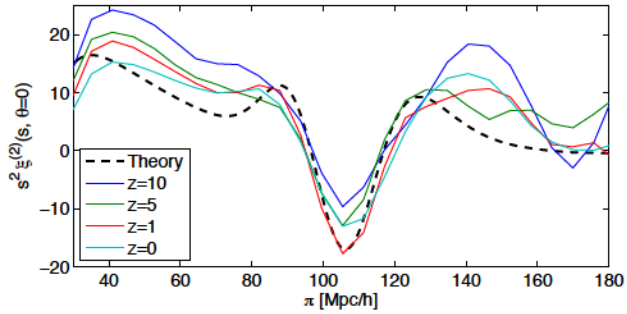

(a) Line of sight ($\mu = 1$)

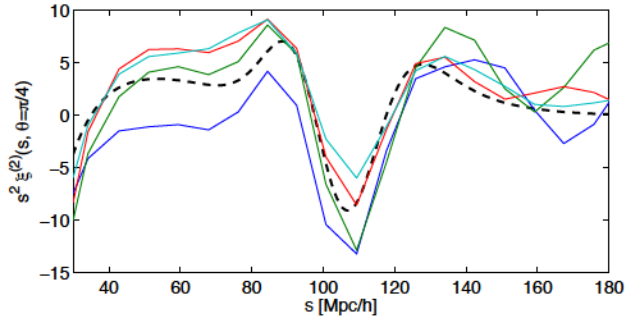

(b) Diagonal ($\mu = \sqrt{2}/2$)

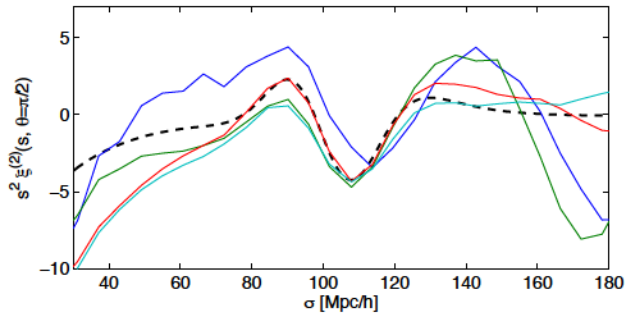

(c) Transverse ($\mu = 0$)

Figure 2.6: Cuts along different values of μ in the nonlinear contribution to the correlation function measured from Zel'dovich realizations versus the theoretical prediction for the 2nd-order contribution.

2.4 Conclusion

We have shown that the nonlinear correlation function can be directly calculated in a perturbative fashion in configuration space from the Zel'dovich approximation, and that this term is in agreement with both the analytical Fourier-space result and with numerical simulations. In configuration space, the nonlinear term has a simple form – the sum of products of a broader class of linear correlation functions, $\xi_n^m(r)$. Higher order terms are in principle straightforward to compute, involving terms with products of more than two of these functions. The simple form of these higher order terms is one advantage to developing perturbation theory in configuration space.

We have also shown that our configuration-space approach to perturbation theory can be extended to redshift space to give the nonlinear redshift-space correlation function to 2nd order in the Zel'dovich approximation. We validated our result through comparison with numerical simulations of the full Zel'dovich approximation. While the expression for the nonlinear contribution is made up of many terms, it is computationally simple because it is a closed-form expression made up of products of linear correlation functions, $\xi_n^m(s)$.

In principle, this method can be extended both to higher orders in the Zel'dovich approximation, beyond 2nd order, and to higher orders in Lagrangian Perturbation Theory, beyond the Zel'dovich approximation. Beyond 2nd order, the terms will be made up of more products of linear correlation functions, and should be straightforward to compute. Extending this method to higher orders in Lagrangian Perturbation

Theory would result in more accurate results, comparable to standard perturbation theory. We leave these extensions to future work.

Chapter 3

The Effect of Density Transformations on the BAO Peak

3.1 Introduction

The "standard ruler" that Baryon Acoustic Oscillations provide is an important cosmological tool for measuring dark energy parameters. The BAO peak has now been detected at unquestionable significance (Eisenstein et al. 2005; Cole et al. 2005; Anderson et al. 2012, 2014). The power and cleanliness of the BAO method is such that despite these impressively large data sets, statistical uncertainties still dominate the systematic effects. With the advent of even larger upcoming surveys, however, systematics such as the small shift in the BAO peak will soon be crucial to consider.

The peak is distorted and shifted at low redshift, even in the conceptually straight-

forward real-space dark-matter field, without galaxy bias and redshift-space distortions. This happens because of bulk displacements, understood most easily in a Lagrangian description. The broadening is largely removable by estimating the displacement field with the simple, linear Zel'dovich approximation (Eisenstein et al. 2007; Padmanabhan et al. 2012; Mehta et al. 2011). Refinements in estimating the displacement field, such as using the log density, are also promising (Mohayaee et al. 2006; Lavaux et al. 2008; Falck et al. 2012; Kitaura & Angulo 2012; Tassev & Zaldarriaga 2012). While restoring the initial sharpness of the BAO peak has obvious statistical benefits, such reconstruction methods can be rather involved.

As surveys grow, the shift in the peak becomes more important to consider in analysis than the broadening. Various studies have attributed the shift to so-called "mode-coupling" terms in the power spectrum (Smith et al. 2008; Matsubara 2008b; Seo et al. 2008; Padmanabhan & White 2009; Taruya et al. 2009).

We can also understand the peak shift in configuration space. The over-density correlation function $\xi_\delta(r) = \langle\delta(\mathbf{x})\delta(\mathbf{r}+\mathbf{x})\rangle_\mathbf{x}$ is a volume average of over-densities $\delta = \rho/\bar{\rho} - 1$ at separation $\mathbf{r}$. The presence of the BAO peak in the linear correlation function means that on average in the initial conditions, over- and under-densities are surrounded by over- and under-dense shells, respectively, at a radius $r = r_s$, the sound horizon. In the initial conditions, the Gaussian probability density function (PDF) of $\delta_{\rm lin}$ exactly balances the contribution of the over-dense and under-dense regions to ξ_δ.

CHAPTER 3. THE EFFECT OF DENSITY TRANSFORMATIONS ON THE BAO PEAK

At low redshift, the PDF of δ becomes highly skewed, as over-densities collect matter and become sharp peaks (where δ grows arbitrarily high) at the expense of broad, shallow void regions (where $\delta \geq -1$). If the BAO shell around each particle remained intact, tethered to move precisely with the particle toward or into clusters, the peak in ξ_δ would not shift from its original location.

However, 3D motions generally cannot preserve all BAO shells. Central over- and under-densities attract or repel their over- and under-dense shells, broadening the averaged peak at low redshift. Moreover, the over-dense shells grow nonlinearly in density, and narrow (they must, from mass conservation); under-dense shells broaden. This nonlinear density enhancement of over-dense shells at $\delta(\mathbf{r}+\mathbf{x})$ gives more weight to $\delta(\mathbf{x}) > 0$ than < 0, pulling the peak in $\xi(r)$ to slightly lower r. This view of the peak shift is similar to that of Sherwin & Zaldarriaga (2012) in which the peak shifts because of an increased abundance of tracers in over-dense regions, where the universe expands more slowly than average.

In this Chapter, we use the Zel'dovich approximation (Zel'dovich 1970) to test the hypothesis that a density transform that produces a more-Gaussian final-conditions density PDF leads to a reduction in the peak motion, as such a transform more equally weights the contributions in the volume average from over-dense and under-dense regions. While we do not show mathematically how transformations change the weightings in the correlation function average, which would involve manipulating the PDFs of the transformed fields, we verify that the more weight low densities receive

in a transformation, the larger the peak position. We investigate two transformations that produce near-Gaussian PDFs – the log density and the displaced-initial-density – and one that over-weights low densities, $(1+\delta)^{-1}$.

Our investigation of log-density statistics is also motivated by recent work on clustering statistics of the log density and Gaussianized density, which have dramatically lower covariance on small scales, as well as better fidelity to the linear-theory shape (Neyrinck et al. 2009b). In principle, they can then give much tighter constraints on cosmological parameters (Neyrinck 2011). In fact, analysis of the log-density correlation function accesses all of the Fisher information in an idealized entirely lognormal field, whereas using even arbitrarily high-point δ correlation functions can give only a small fraction of that total information (Carron 2011; Carron & Neyrinck 2012). Here, for the first time we explicitly show the benefits of a log transform on large scales, where the benefits might have been thought to be negligible.

3.2 Theory

In this Section, we use the Zel'dovich approximation to calculate the nonlinear correlation functions of the density, the log density, and the displaced-initial-density field. We follow the approach outlined in Chapter 2 for perturbatively calculating the nonlinear density correlation function in the Zel'dovich approximation. We extend this approach to calculate the nonlinear correlation functions of the log density and

the Lagrangian density δ_L at an Eulerian position $\mathbf{x}$. For the latter, we examine the effect of Zel'dovich displacements by themselves, without considering the change in density at a constant Lagrangian coordinate.

As in Chapter 2, we start with the Zel'dovich approximation (Zel'dovich 1970). The initial displacement potential is related to the initial density field through the Poisson equation:

$$\mathbf{x}(\mathbf{q},t) = \mathbf{q} - D(t)\nabla_q\phi(\mathbf{q}) \ , \tag{3.1}$$

$$D(t)\nabla_q^2\phi(\mathbf{q}) = \delta_0(\mathbf{q},t) \ .$$

We write the Eulerian density in terms of the Jacobian of the transformation from Lagrangian to Eulerian coordinates from the conservation of mass:

$$\frac{\rho(\mathbf{x},t)}{\bar{\rho}} = \left|\frac{\partial x_i}{\partial q_j}\right|^{-1} = \frac{1}{J(\mathbf{q},t)} = 1 + \delta(\mathbf{q}(\mathbf{x})) \ . \tag{3.2}$$

The Jacobian can be written in terms of the eigenvalues (λ_1, λ_2, and λ_3) of the deformation tensor $d_{ij}(\mathbf{q})$, or equivalently in terms of the invariants of the matrix (I_1, I_2, and I_3), which are simple functions of the eigenvalues (Bouchet et al. 1995).

$$d_{ij}(\mathbf{q}) = \frac{\partial^2\phi(\mathbf{q})}{\partial q_i \partial q_j} \ , \tag{3.3}$$

$$J(\mathbf{q},t) = (1 - D\lambda_1)(1 - D\lambda_2)(1 - D\lambda_3) \tag{3.4}$$

$$= 1 - DI_1(\mathbf{q}) + D^2I_2(\mathbf{q}) - D^3I_3(\mathbf{q}) \ . \tag{3.5}$$

Using the Zel'dovich approximation, we write the nonlinear density perturbatively

in Eulerian coordinates as:

$$\delta(\mathbf{x},t) = \left(\delta(\mathbf{q},t) + D\sum_i \frac{\partial\phi(\mathbf{q})}{\partial q_i}\frac{\partial\delta(\mathbf{q},t)}{\partial q_i} + D^2\sum_{i,j}\frac{\partial^2\phi(\mathbf{q})}{\partial q_i\partial q_j}\frac{\partial\phi(\mathbf{q})}{\partial q_j}\frac{\partial\delta(\mathbf{q},t)}{\partial q_i} + \frac{1}{2}D^2\sum_{i,j}\frac{\partial^2\delta(\mathbf{q},t)}{\partial q_i\partial q_j}\frac{\partial\phi(\mathbf{q})}{\partial q_i}\frac{\partial\phi(\mathbf{q})}{\partial q_j}\right)\Bigg|_{\mathbf{q}=\mathbf{x}} . \tag{3.6}$$

The correlation function of the over-density in co-moving Eulerian coordinates can then be written in powers of D as:

$$\xi_\delta(\mathbf{r},t) \equiv \langle\delta(\mathbf{x},t)\delta(\mathbf{x}+\mathbf{r},t)\rangle = \xi_\delta^{(1)}(\mathbf{r})D^2 + \xi_\delta^{(2)}(\mathbf{r})D^4 + ... \tag{3.7}$$

We have explicitly labeled this correlation function ξ_δ to distinguish it from other correlation functions we consider later.

As we found in Chapter 2, the first nonlinear term in the over-density correlation function can be calculated in terms of the linear statistics using Equation 3.6. The final expression we found is:

$$\xi_\delta^{(2)}(\mathbf{r}) = -\frac{1}{3}\xi_0^{-2}(0)\xi_0^2(r)\frac{19}{15}\xi_0^0(r)^2 + \frac{34}{21}\xi_2^0(r)^2 + \frac{4}{35}\xi_4^0(r)^2 - \frac{16}{5}\xi_1^{-1}(r)\xi_1^1(r) - \frac{4}{5}\xi_3^{-1}(r)\xi_3^1(r) + \frac{1}{3}\xi_0^{-2}(r)\xi_0^2(r) + \frac{2}{3}\xi_2^{-2}(r)\xi_2^2(r) . \tag{3.8}$$

We can use the same approach to calculate the correlation function of the log of the density field. Starting with Equation 3.2 and using the definition of the Jacobian, Equation 3.4, we compute the log of the density, which we define as the quantity $A(\mathbf{q})$:

$$\begin{aligned}\ln(1+\delta(\mathbf{q},t)) \equiv A(\mathbf{q}) &= -\ln J(\mathbf{q},t) \\ &= -(\ln(1-D\lambda_1) + \ln(1-D\lambda_2) + \ln(1-D\lambda_3)) .\end{aligned} \tag{3.9}$$

We expand this expression in powers of D, and rewrite it in terms of the invariants of the deformation tensor:

$$\begin{aligned}\ln(1+\delta(\mathbf{q},t)) &= D(\lambda_1+\lambda_2+\lambda_3)+\frac{1}{2}D^2(\lambda_1^2+\lambda_2^2+\lambda_3^2)+\frac{1}{3}D^3(\lambda_1^3+\lambda_2^3+\lambda_3^3)+... \\ &= DI_1+\frac{1}{2}D^2(I_1^2-2I_2)+\frac{1}{3}D^3(I_1^3-3I_1I_2+3I_3)+... \end{aligned} \tag{3.10}$$

We now have the log density expressed in Lagrangian coordinates, $\mathbf{q}$. We transform this into Eulerian coordinates as above to get an expression for $A(\mathbf{x},t)$. Because this quantity has a non-zero mean, its correlation function is defined as:

$$\xi_A(\mathbf{r},t) = \left\langle (A(\mathbf{x},t)-\bar{A})(A(\mathbf{x}+\mathbf{r},t)-\bar{A})\right\rangle \ , \tag{3.11}$$

where $\bar{A}$ is the Eulerian mean.

The first two terms in the correlation function are then:

$$\xi_A^{(1)}(r) = \xi_0^0(r) \ , \tag{3.12}$$

$$\begin{aligned}\xi_A^{(2)}(r) = &-\frac{2}{3}\xi_0^0(0)\xi_0^0(r)-\frac{1}{3}\xi_0^{-2}(0)\xi_0^2(r)+\frac{13}{30}\xi_0^0(r)^2+\frac{20}{21}\xi_2^0(r)^2+\frac{4}{35}\xi_4^0(r)^2 \\ &-\frac{6}{5}\xi_1^{-1}(r)\xi_1^1(r)-\frac{4}{5}\xi_3^{-1}(r)\xi_3^1(r)+\frac{2}{3}\xi_2^{-2}(r)\xi_2^2(r)+\frac{1}{3}\xi_0^{-2}(r)\xi_0^2(r) \ . \end{aligned} \tag{3.13}$$

Note that the first term in $\xi_A^{(2)}(r)$ can be written as $-\frac{2}{3}\sigma_0^2\xi_A^{(1)}(r)$, where σ_0^2 is the variance of the initial density field (where the density is assumed to be smoothed on some scale). This term describes the reduction in the amplitude of ξ_A compared with the linear correlation function.

Next, we look at the initial density field at Eulerian position $\mathbf{x}$. For this quantity, we take the initial density, $\delta_0(\mathbf{q})$, and use the Zel'dovich formula, Equation 3.1, to

relate $\mathbf{q}$ to $\mathbf{x}$. The expression for $\delta_L(\mathbf{x})$ is equivalent to Equation 3.6, but with δ replaced with δ_0:

$$\delta_L(\mathbf{x}) = \left(\delta_0(\mathbf{q}) + D^2 \sum_i \frac{\partial\phi(\mathbf{q})}{\partial q_i}\frac{\partial\delta_0(\mathbf{q})}{\partial q_i} + D^3 \sum_{i,j} \frac{\partial^2\phi(\mathbf{q})}{\partial q_i \partial q_j}\frac{\partial\phi(\mathbf{q})}{\partial q_j}\frac{\partial\delta_0(\mathbf{q})}{\partial q_i} + \frac{D^3}{2}\sum_{i,j}\frac{\partial^2\delta_0(\mathbf{q})}{\partial q_i\partial q_j}\frac{\partial\phi(\mathbf{q})}{\partial q_i}\frac{\partial\phi(\mathbf{q})}{\partial q_j}\right)\Bigg|_{\mathbf{q}=\mathbf{x}} . \tag{3.14}$$

We label the correlation function of this quantity as ξ_{δ_L}. The first two terms are:

$$\xi^{(1)}_{\delta_L}(r) = \xi^0_0(r) \ , \tag{3.15}$$

$$\xi^{(2)}_{\delta_L}(r) = -\frac{2}{3}\xi^0_0(0)\xi^0_0(r) + \frac{1}{3}\xi^0_0(r)^2 + \frac{2}{3}\xi^0_2(r)^2 + \frac{1}{3}\xi^{-2}_0(r)\xi^2_0(r) - \frac{1}{3}\xi^{-2}_0(0)\xi^2_0(r) + \frac{2}{3}\xi^{-2}_2(r)\xi^2_2(r) \ . \tag{3.16}$$

Again, we note the damping term, $-\frac{2}{3}\xi^0_0(0)\xi^0_0(r)$, which is the same as we found in ξ_A. We also note that the expression for $\xi^{(2)}_{\delta_L}$ is simpler than either $\xi^{(2)}_{\delta}$ or $\xi^{(2)}_{A}$.

Finally, to investigate the peak shift in a transformation which further boosts the weight of under-densities, we consider the correlation function of the reciprocal of the density, $\xi_{1/\rho}$. This statistic is of some theoretical interest in a Lagrangian approach, since $(1+\delta)^{-1}$ is simply the Jacobian, Equation 3.4. When we transform to Eulerian coordinates we get:

$$(1+\delta(\mathbf{x}))^{-1} = \left(J(\mathbf{q}) + D^2 \sum_i \frac{\partial\phi(\mathbf{q})}{\partial q_i}\frac{\partial J(\mathbf{q})}{\partial q_i} + D^3 \sum_{i,j} \frac{\partial^2\phi(\mathbf{q})}{\partial q_i \partial q_j}\frac{\partial\phi(\mathbf{q})}{\partial q_j}\frac{\partial J(\mathbf{q})}{\partial q_i} + \frac{D^3}{2}\sum_{i,j}\frac{\partial^2 J(\mathbf{q})}{\partial q_i\partial q_j}\frac{\partial\phi(\mathbf{q})}{\partial q_i}\frac{\partial\phi(\mathbf{q})}{\partial q_j}\right)\Bigg|_{\mathbf{q}=\mathbf{x}} . \tag{3.17}$$

The first two terms of $\xi_{1/\rho}$ are:

$$\xi^{(1)}_{1/\rho}(r) = \xi^0_0(r) \ , \tag{3.18}$$

$$\xi^{(2)}_{1/\rho}(r) = \frac{2}{3}\xi^0_0(0)\xi^0_0(r) - \frac{1}{3}\xi^{-2}_0(0)\xi^2_0(r) + \frac{3}{5}\xi^0_0(r)^2 + \frac{2}{7}\xi^0_2(r)^2 + \frac{4}{35}\xi^0_4(r)^2 + \frac{4}{5}\xi^{-1}_1(r)\xi^1_1(r) - \frac{4}{5}\xi^{-1}_3(r)\xi^1_3(r) + \frac{2}{3}\xi^{-2}_2(r)\xi^2_2(r) + \frac{1}{3}\xi^{-2}_0(r)\xi^2_0(r) \ . \tag{3.19}$$

Because our interest in this transformation is to test a more extreme weighting of under-densities, and we do not anticipate a practical measurement of $\xi_{1/\rho}$ (which, for example, could be violently sensitive to discreteness noise), for clarity we do not plot $\xi_{1/\rho}$ in the figures below, but do discuss its peak position.

3.3 Discussion

Our goal is to understand how the various transformations to the density field affect the correlation function, specifically at the BAO peak. In this section, we consider the effects of the first nonlinear term in the correlation functions on the BAO peak position and shape. We then examine the various terms in the expressions in order to understand their role in the overall correlation function. For the following we use an initial power spectrum generated by CAMB (Lewis et al. 2000), assuming fiducial WMAP5 cosmological parameters (Komatsu et al. 2009): $(H_0, \Omega_\Lambda, \Omega_{\rm CDM}, \Omega_b, n_s, \sigma_8) = (70.1, 0.233, 0.0462, 0.721, 0.96, 0.817)$. We smooth the linear power spectrum with a $\sigma = 5$ Mpc/h Gaussian, which was a large enough smoothing length to give agreement between the analytical expression and numerical Zel'dovich realizations in

Chapter 2 up to $z = 0$.

Fig. 3.1 shows the correlation functions at $z = 0$ of the linear theory density, Zel'dovich density, Zel'dovich log-density, and displaced-initial-density. We note that the BAO peak of all nonlinear correlation functions are broadened compared with $\xi_{\rm lin}$. The smoothing of the acoustic peak relative to that of the linear correlation function is due to large-scale bulk motions, which are present in the three nonlinear fields. In the case of ξ_δ we also observe an enhancement at the peak, perhaps from over-weighting over-dense mass elements, which contract.

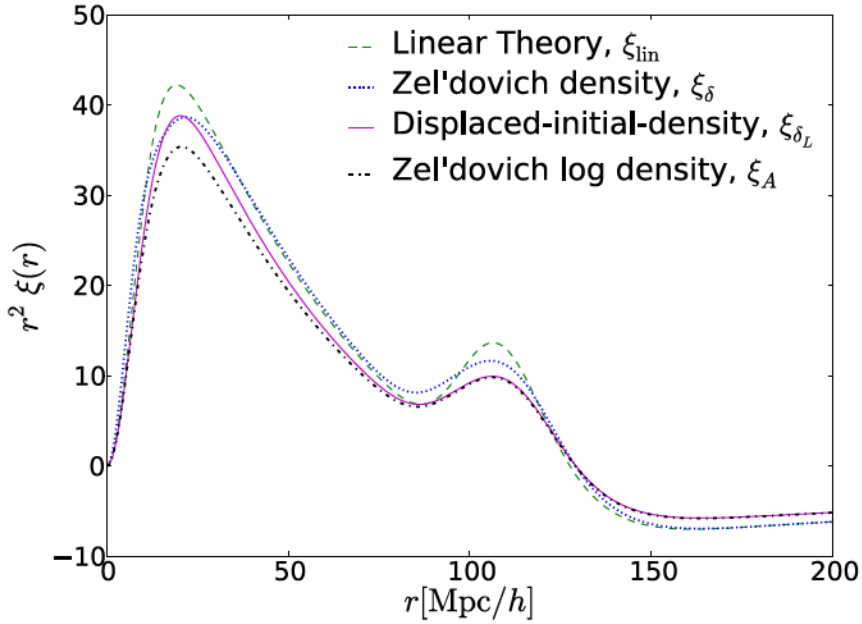

Figure 3.1: Nonlinear correlation functions at $z = 0$. Green dashed line - linear theory, Blue dotted line - nonlinear density from Zel'dovich approximation, magenta solid line - displaced-initial-density field, $\delta_L(\vec{x})$, black dot-dashed line - $\ln(1+\delta)$ from Zel'dovich approximation

Fig. 3.2 shows a close-up of the BAO peak, and the position of each of the peaks (r_p) is indicated. We measure the peak of $r^2\xi$ because this is the quantity that is integrated to give the variance on a given scale. The peaks in order of largest to smallest r_p are: $\xi_{1/\rho}$: $r_p = 106.5$ Mpc/h (not shown), $\xi_{\rm lin}$: $r_p = 106.4$ Mpc/h, ξ_{δ_L} : $r_p = 106.2$ Mpc/h, ξ_A : $r_p = 106.1$ Mpc/h, and ξ_δ : $r_p = 105.8$ Mpc/h. There are other roughly equivalent definitions of the peak position, such as the minimum χ^2 of template correlation functions or the peak through a wavelet filter. These are essential to use in the presence of cosmic variance, but the simpler peak definition used here is acceptable since we use a linear correlation function with no cosmic variance.

Next, we look at the effects of individual terms in the nonlinear expressions on the location of the peak. Fig. 3.3 shows the terms that contribute to each of these nonlinear correlation functions. We exclude the damping terms of ξ_A and ξ_{δ_L} because they do not contribute to the shift in the peak position. Each term is represented by a different color, and the solid lines have a different amplitude in each expression. The dot-dashed line has the same amplitude in ξ_δ and ξ_A (and is zero in ξ_{δ_L}), and the dashed line is the same in all three expressions. From this plot we see that the effect of the dashed black line is to smooth the peak in all three cases, by increasing the amplitude around the peak and decreasing the amplitude at the peak. Several of the other terms cause a shift in the peak position by showing a slope around the peak. For ξ_{δ_L}, the magenta line is the only term with this property, so the shift is not very large. In ξ_δ and ξ_A, the red (dot-dashed) and magenta (solid) lines have nearly

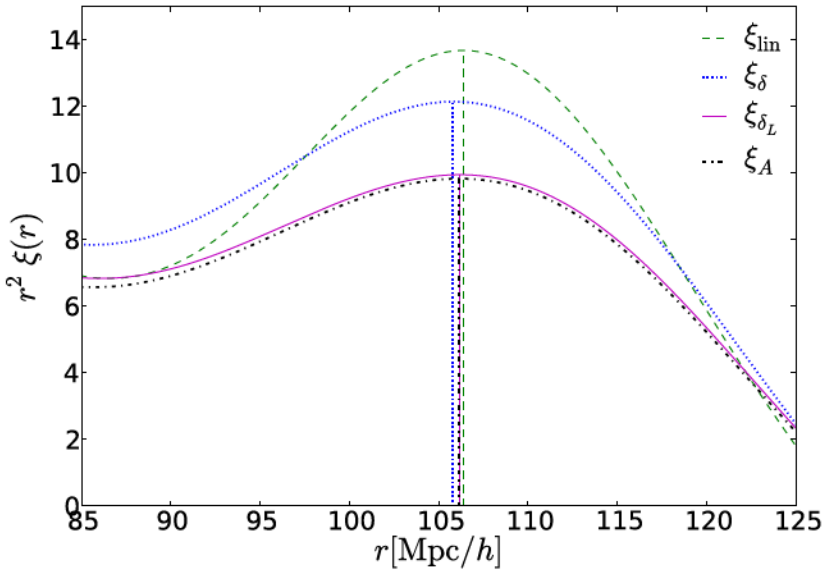

Figure 3.2: Peak locations of the various correlation functions at $z = 0$. Green dashed line - linear theory, peak is at $r = 106.4$Mpc/h. Blue dotted line - nonlinear density from Zel'dovich approximation, peak is at $r = 105.8$ Mpc/h. Magenta solid line - displaced-initial-density, $\delta_L(\vec{x})$, peak is at $r = 106.2$ Mpc/h. Black dot-dashed line - $\ln(1+\delta)$ from Zel'dovich approximation, peak is at $r = 106.1$ Mpc/h.

opposite slopes, and so the shift from the combination of these terms is small.

The major contributor to the shift in the peak position in ξ_A and ξ_δ is the (solid) blue line, which is the term proportional to $-\xi_1^1(r)\xi_1^{-1}(r)$. In ξ_δ the amplitude of this term is 16/5, whereas for ξ_A the amplitude is 6/5. Thus we see a larger shift in the peak position in ξ_δ than in ξ_A, and both have larger shifts than ξ_{δ_L}. We also note that in the expression for $\xi_{1/\rho}$ this term has the opposite sign, indicating a shift to greater radius.

We can understand this term better by using the recursion relation for spherical Bessel functions:

$$j_0'(x) = -j_1(x) \tag{3.20}$$

This allows us to rewrite $\xi_1^m(r)$ in terms of derivatives of the linear correlation functions with respect to r:

$$\xi_1^m(r) = -\xi_0^{m-1}(r)' \tag{3.21}$$

$$\xi_1^1(r)\xi_1^{-1}(r) = \xi_0^0(r)'\xi_0^{-2}(r)' \tag{3.22}$$

In fact this is exactly the term Crocce & Scoccimarro (2008b) found to be responsible for the BAO peak shift from the mode coupling term of the correlation function in renormalized perturbation theory. This term is the product of the derivative of the linear density correlation function ($\xi_0^0(r)$) and the derivative of the linear velocity correlation function ($\xi_0^{-2}(r)$).

3.4 Conclusion

In this Chapter, we have explored the idea that the shift in the position of the BAO peak in the usual density correlation function is due to over-weighting of high density peaks that bulk flows bring toward each other. We have shown that the two transformations to the density field that suppress over-dense regions and boost under-dense regions in statistical weight result in a reduced shift in the BAO peak position

at low redshift. Moreover, we have shown that a transformation that further weights under-dense regions causes the peak to shift in the opposite direction, to larger r. We used the Zel'dovich approximation and configuration-space perturbation theory to examine the first nonlinear contribution to the correlation functions of the nonlinear density, the log-density, and the displaced-initial-density fields. We identified the terms largely responsible for the shift in the BAO peak, and found that they were proportional to the first derivative of the linear correlation function. The displaced-initial-density exhibits the smallest shift due to a lack of shift terms in the nonlinear correlation function expression.

The log-density correlation function has some shift, but it is smaller than in the nonlinear density correlation function. In fact, the correlation function of the log density is almost indistinguishable from that of the displaced-initial-density on BAO scales. The near-equivalence of the log density and the displaced initial density recalls the lognormal model of Coles & Jones (1991), in which gravity enhances initial densities with an exponential transform, even though a Zel'dovich-realization density field is not an exactly lognormal field.

By studying both the nonlinear density and displaced-initial-density, we decouple the effects of density enhancements from the bulk flows of initial fluctuations. The fundamental broadening of the initial peak is seen in ξ_{δ_L}, whereas in ξ_δ the peak is additionally sharpened. However, we suspect that this sharpness is not statistically useful because it comes from only the fraction of the mass elements that have con-

tracted. We intend to test the noise properties of the transformed fields in N-body simulations. Future work is also needed to examine the potential of transformations such as these in the presence of galaxy bias, discreteness, and redshift-space distortions.

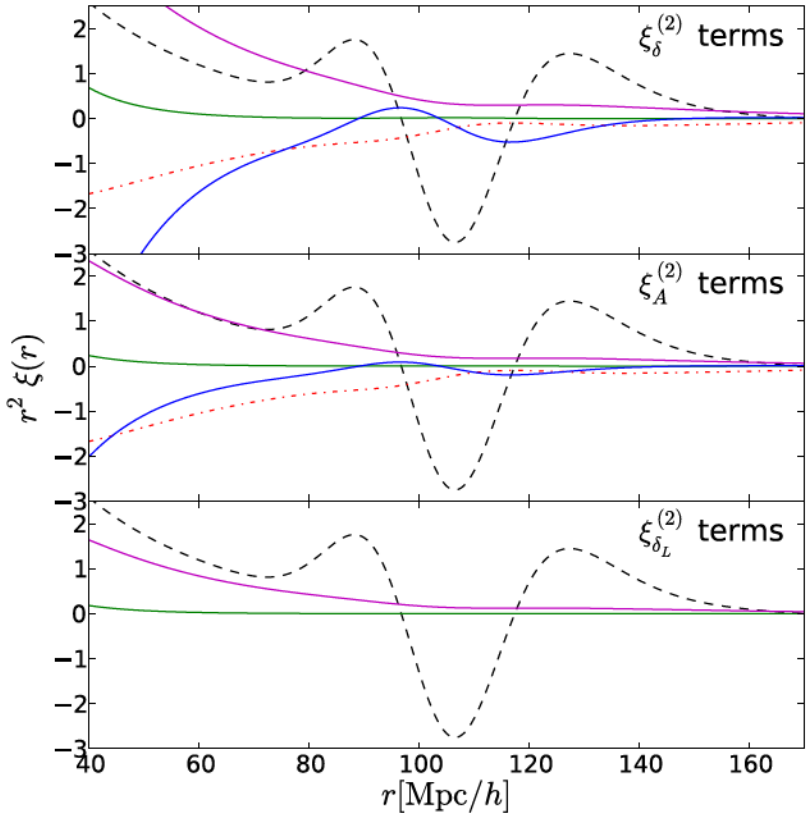

Figure 3.3: Top to bottom: Terms in the expressions for $\xi_\delta^{(2)}$, $\xi_A^{(2)}$, and $\xi_{\delta_L}^{(2)}$ (not including damping terms in the bottom two). Different terms are represented by different colors: Black dashed - terms with same amplitude in all 3 expressions $\left[1/3(\xi_0^2(r)\xi_0^{-2}(r) - \xi_0^2(r)\xi_0^{-2}(r)) + 2/3\xi_2^2(r)\xi_2^{-2}(r)\right]$. Red dot-dash - terms that are the same in both ξ_δ and ξ_A $\left[-4/5\xi_3^1(r)\xi_3^{-1}(r) + 4/35\xi_4^0(r)^2\right]$. The amplitude of this term is zero for ξ_{δ_L}. Green - amplitude of $\xi_0^0(r)^2$ term. Magenta - amplitude of $\xi_2^0(r)^2$ term. Blue - amplitude of $\xi_1^1(r)\xi_1^{-1}(r)$. This term is largely responsible for the shift in peak position.

Chapter 4

The Nonlinear Matter Bispectrum

4.1 Introduction

The two-point correlation function of galaxies has been widely employed to study the large-scale structure, and has provided tight constraints cosmological parameters associated with on the curvature of the universe, initial conditions, and properties of dark energy (Tegmark et al. 2006; Blake et al. 2011b; Parkinson et al. 2012; Reid et al. 2012; de la Torre et al. 2013).

A complete description of non-Gaussian large-scale structure, however, must include higher-order statistics. Although the matter density fluctuations follow *nearly* Gaussian statistics at early times, the nonlinear process of gravitational instability generically drives the matter density non-Gaussian. In addition, a nonlinear bias relation between the galaxy-density and matter-density contrast and the distortion

of the measured redshift of galaxies due to peculiar velocities further enhances the non-Gaussianity. The leading order statistic sensitive to such non-Gaussianity is the three-point correlation function and its Fourier transform the bispectrum. The three-point correlation function is defined as:

$$\zeta(r_1, r_2, r_3) = \langle \delta(\mathbf{x}_1)\delta(\mathbf{x}_2)\delta(\mathbf{x}_3) \rangle \ , \tag{4.1}$$

where $\delta(\mathbf{x})$ is the over-density at position $\mathbf{x}$, $r_1 = |\mathbf{x}_1 - \mathbf{x}_3|$, $r_2 = |\mathbf{x}_2 - \mathbf{x}_1|$, and $r_3 = |\mathbf{x}_3 - \mathbf{x}_2|$ are the lengths of the sides of the triangle formed by $\mathbf{x}_1$, $\mathbf{x}_2$, and $\mathbf{x}_3$. The bispectrum is defined as:

$$(2\pi)^3 B(k_1, k_2, k_3)\delta_D(\mathbf{k}_1 + \mathbf{k}_2 + \mathbf{k}_3) = \langle \hat{\delta}(\mathbf{k}_1)\hat{\delta}(\mathbf{k}_2)\hat{\delta}(\mathbf{k}_2) \rangle \ , \tag{4.2}$$

where δ_D is the 3-dimensional Dirac-delta function ensuring the wave-vectors $\mathbf{k}_1$, $\mathbf{k}_2$, and $\mathbf{k}_3$ form a triangle.

The galaxy three-point function and bispectrum have been measured previously in several galaxy surveys, including IRAS (Scoccimarro et al. 2001), 2dFGRS (Verde et al. 2002; Gaztañaga et al. 2005), SDSS (Nichol et al. 2006; Nishimichi et al. 2007; Marín 2011; McBride et al. 2011a,b), and WiggleZ (Marín et al. 2013), but have not been as fruitful as their two-point counterparts. This is in part because theoretical models of the three-point correlation function and bispectrum have not yet reached the level that is required for sophisticated data analysis.

Future surveys promise orders of magnitude improvement in both galaxy number density and volume coverage, permitting better determination of the higher-point

statistics of the cosmic density field. Upon accessing all the cosmological information, the three-point statistics will be a powerful probe of inflation (Jeong & Komatsu 2009; Sefusatti & Komatsu 2007; Baldauf et al. 2011), nonlinear structure formation (Scoccimarro et al. 1998, 1999), and astrophysics such as galaxy formation (Baldauf et al. 2011). In order to fully exploit the data, we must develop more accurate theoretical models of the 3-point statistics.

In order to extract information from the galaxy bispectrum, we first have to accurately model the bispectrum of the underlying matter field. This can be done numerically, with N-body simulations, or analytically with Standard Perturbation Theory and various extensions thereof.

Cosmological N-body simulations are the most direct way of studying the nonlinear evolution of the matter bispectrum. One consideration when looking at the n-point statistics (in particular at high redshift) is transients from initial conditions of the simulation (Scoccimarro 1998; Crocce et al. 2006).

In simulations, the initial positions and velocities of the particles are often generated by using Lagrangian Perturbation Theory (LPT), either to first order (Zel'dovich approximation) or second order (2LPT). Because the initial conditions from the Zel'dovich approximation and 2LPT include spurious decaying modes – which do not exist in the real universe – on top of the desired growing modes, one has to wait a long enough time for the decaying modes to sufficiently decay away (Scoccimarro 1998). For the case of power spectrum, 2LPT initial conditions with starting redshift

of $z_{\rm ini} = 49$ may be enough for capturing the nonlinearities at $z = 0$ (Crocce et al. 2006).

Unlike in the power spectrum, where the Zel'dovich transients come from from sub-leading order, the decaying modes in the matter bispectrum affect the leading order, and suppress the resulting matter bispectrum even on very large scales. As we shall show in Section 4.3, correct simulation of the nonlinear matter bispectrum at redshifts $1 < z < 6$ requires even earlier starting redshifts with 2LPT initial conditions.

Parallel to numerical simulations is theoretical study of the nonlinear evolution of the matter density field. Standard Perturbation Theory (SPT) (for a review: Bernardeau et al. (2002)) models nonlinearities in the matter density field as a pressureless, single fluid evolving under gravitational interaction. In SPT, the leading order, tree-level, matter bispectrum can be calculated from the second order solution for the density field, giving us an expression that is valid on large scales.

Beyond tree-level, one can include successive higher order corrections to the bispectrum, which may correctly model the nonlinear bispectrum in the quasi-linear regime. For even smaller scales, where the density contrast is of order unity, SPT breaks down and the matter density field is in the fully nonlinear regime.

Various alternate approaches to SPT have been proposed to model the bispectrum on nonlinear scales. The first are phenomenological fitting formulas based on N-body simulations that claim to better model the nonlinear behavior of the bispectrum at

low redshift. There are two fitting formulas available in the literature: one proposed by Scoccimarro & Couchman (2001) and more recently one proposed by Gil-Marín et al. (2012). Another approach, informed by the recent development of renormalized perturbation theory (Crocce & Scoccimarro 2006), uses simplistic models of renormalizing the power spectrum while keeping the tree-level vertex (the second order kernel) intact. That is, we assume that the nonlinear behavior of the bispectrum is completely described by the nonlinear power spectrum, so the usual tree-level expression is altered by replacing the linear power spectrum with the nonlinear power spectrum.

In Section 4.4, we compare the three nonlinear formulas for the matter bispectrum with the results from the N-body simulations, and find the region of validity for each of formula. We find that the most stable model on the scales and redshifts we considered is the original phenomenological fitting formula proposed by Scoccimarro & Couchman (2001), and that the more recent formula fails on small scales and high redshifts. However, at high redshift ($z \approx 6$), 1-loop SPT is a better fit than the phenomenological models. Our results indicate that no single model works best in all regimes. Further work is needed to develop a more reliable model on a larger range of scales and redshift in order to effectively use the measured galaxy bispectrum to constrain cosmological parameters.

4.2 Standard Perturbation Theory

Here, we review Standard Perturbation Theory to calculate the tree-level bispectrum (Scoccimarro 1998, 2001; Bernardeau et al. 2002). We then follow the approach of Scoccimarro (1998) and Crocce et al. (2006) to compute the correct growing and decaying modes for initial conditions set using the Zel'dovich Approximation and 2LPT.

One way of simplifying the single fluid equations (Equations 1.19 and 1.20) is by combining the density field $\delta(\mathbf{k},\eta)$ and velocity divergence field $\theta(\mathbf{k},\eta)$ into a doublet as:

$$\Psi_a(\mathbf{k},\eta) = (\delta(\mathbf{k},\eta), -\theta(\mathbf{k},\eta)/\mathcal{H}) \ , \tag{4.3}$$

and using the logarithm of the linear growth factor relative to its initial value $\eta \equiv \ln(D(\tau)/D_i)$ as a time variable. Here, $\mathcal{H} \equiv d\ln a/d\tau = aH$ is the reduced Hubble parameter that is defined with conformal time $\tau = \int dt/a(t)$.

As discussed in Section 1.3.3, we can use the perturbative solution for a matter-dominated universe, and make the substitution $a(\tau) \to D(\tau)$ to account for arbitrary cosmology (Scoccimarro et al. 1998; Bernardeau et al. 2002). Combining the fluid equations for a matter-dominated universe gives us equations of motion for Ψ_a:

$$\partial_\eta \Psi_a(\mathbf{k},\eta) + \Omega_{ab}\Psi_b(\mathbf{k},\eta) = \gamma^{(s)}_{abc}(\mathbf{k},\mathbf{k}_1,\mathbf{k}_2)\Psi_b(\mathbf{k}_1,\eta)\Psi_c(\mathbf{k}_2,\eta) \ . \tag{4.4}$$

Here,

$$\Omega_{ab} \equiv \begin{bmatrix} 0 & -1 \\ -3/2 & 1/2 \end{bmatrix} \tag{4.5}$$

is the linear mixing matrix, and

$$\gamma^{(s)}_{121}(\mathbf{k}, \mathbf{k}_1, \mathbf{k}_2) = (2\pi)^3 \delta_D(\mathbf{k} - \mathbf{k}_1 - \mathbf{k}_2) \frac{\mathbf{k} \cdot \mathbf{k}_1}{2k_1^2} \ , \tag{4.6}$$

$$\gamma^{(s)}_{222}(\mathbf{k}, \mathbf{k}_1, \mathbf{k}_2) = (2\pi)^3 \delta_D(\mathbf{k} - \mathbf{k}_1 - \mathbf{k}_2) \frac{k^2(\mathbf{k}_1 \cdot \mathbf{k}_2)}{2k_1^2 k_2^2} \ , \tag{4.7}$$

encode the non-linear interactions. Note that $\gamma^{(s)}_{121}(\mathbf{k}, \mathbf{k}_1, \mathbf{k}_2) = \gamma^{(s)}_{112}(\mathbf{k}, \mathbf{k}_2, \mathbf{k}_1)$ and the integration $\int d^3k_i/(2\pi)^3$ over the repeated indices ($\mathbf{k}_1$ and $\mathbf{k}_2$) is implied.

A Laplace transform of Equation (4.4) in the variable η leads to:

$$\begin{aligned} &\omega \Psi_a(\mathbf{k}, \omega) - \phi_a(\mathbf{k}) + \Omega_{ab} \Psi_b(\mathbf{k}, \omega) \\ &= \gamma^{(s)}_{abc}(\mathbf{k}, \mathbf{k}_1, \mathbf{k}_2) \int_{c-i\infty}^{c+i\infty} \frac{d\omega_1}{2\pi i} \Psi_b(\mathbf{k}_1, \omega_1) \Psi_c(\mathbf{k}_2, \omega - \omega_1) \ , \end{aligned} \tag{4.8}$$

where $\phi_a(\mathbf{k}) = \Psi_a(\mathbf{k}, \eta = 0)$ is the density and velocity field at the initial time (the time at which we start the simulation). The linear part of Equation 4.8 can be written in terms of a matrix σ_{ab}:

$$\sigma^{-1}_{ab}(\omega) \equiv \omega \delta_{ab} + \Omega_{ab} \ , \tag{4.9}$$

$$\sigma_{ab}(\omega) = \frac{1}{(2\omega + 3)(\omega - 1)} \begin{bmatrix} 2\omega + 1 & 2 \\ 3 & 2\omega \end{bmatrix} \ . \tag{4.10}$$

Finally, we obtain the formal solution through an inverse Laplace transformation

as:

$$\Psi_a(\mathbf{k},\eta) = g_{ab}(\eta)\phi_b(\mathbf{k}) + \int_0^\eta d\eta' g_{ab}(\eta-\eta')\gamma^{(s)}_{bcd}(\mathbf{k},\mathbf{k}_1,\mathbf{k}_2)\Psi_c(\mathbf{k}_1,\eta')\Psi_d(\mathbf{k}_2,\eta') \ . \tag{4.11}$$

Here,

$$g_{ab}(\eta) = \int_{c-i\infty}^{c+i\infty}\frac{d\omega}{2\pi i}\sigma_{ab}(\omega)e^{\omega\eta} = \frac{e^\eta}{5}\begin{bmatrix}3 & 2\\ 3 & 2\end{bmatrix} - \frac{e^{-3\eta/2}}{5}\begin{bmatrix}-2 & 2\\ 3 & -3\end{bmatrix} , \tag{4.12}$$

is the Green's function which describes the time evolution of the linear perturbations. The first term proportional to $e^\eta \propto D/D_i$ is the growing mode and the second term proportional to $e^{-3\eta/2} \propto (D/D_i)^{-3/2}$ is the decaying mode.

In order to find the perturbative solution to Equation 4.11, we expand the initial and final conditions (ϕ_a and Ψ_a) in terms of the linear (Gaussian) density $\delta_0(\mathbf{k})$ field at initial time as:

$$\phi_a(\mathbf{k}) = \sum_{n=1}^\infty \phi_a^{(n)}(\mathbf{k}) \ , \tag{4.13}$$

$$\Psi_a(\mathbf{k},\eta) = \sum_{n=1}^\infty \Psi_a^{(n)}(\mathbf{k},\eta) \ , \tag{4.14}$$

where

$$\phi_a^{(n)}(\mathbf{k}) = [\delta_D]_n \mathcal{T}_a^{(n)}(\mathbf{k}_1,\cdots,\mathbf{k}_n)\delta_0(\mathbf{k}_1)\cdots\delta_0(\mathbf{k}_n) \ , \tag{4.15}$$

$$\Psi_a^{(n)}(\mathbf{k},\eta) = [\delta_D]_n \mathcal{F}_a^{(n)}(\mathbf{k}_1,\cdots,\mathbf{k}_n,\eta)\delta_0(\mathbf{k}_1)\cdots\delta_0(\mathbf{k}_n) \ , \tag{4.16}$$

and $[\delta_D]_n \equiv \delta_D(\mathbf{k} - \mathbf{k}_1 - \cdots - \mathbf{k}_n)$. Here, $\mathcal{T}_a^{(n)}$ are the n-th order kernels of the initial density and velocity fields, and $\mathcal{F}_a^{(n)}(\eta)$ are the n-th order resulting kernels at a later time η. Again, the integration $\int d^3k_i/(2\pi)^3$ over the repeated $\mathbf{k}_i$'s are implied.

We can now calculate the kernels $\mathcal{F}_a^{(n)}$ at the final redshift from the initial kernels $\mathcal{T}_a^{(n)}$:

$$\mathcal{F}_a^{(n)}(\eta) = g_{ab}(\eta)\mathcal{T}_b^{(n)} + \sum_{m=1}^{n-1} \int_0^\eta ds\; g_{ab}(\eta - s)\gamma_{bcd}^{(s)}\mathcal{F}_c^{(m)}(s)\mathcal{F}_d^{(n-m)}(s). \tag{4.17}$$

This recursion relation is the starting point of our analysis of the growing and decaying modes in the bispectrum.

4.2.1 Growing mode solutions

In the real universe, the decaying modes decay away at very early times, and the density field is in its fastest growing mode for any reasonable choice of the initial redshift. Therefore, the initial conditions for an ideal N-body simulations must be set at an early enough time (or high enough redshift) such that SPT is valid on the smallest resolved scales, and set by the fastest growing modes at all relevant orders in SPT.

Here, we find the fastest growing mode solution perturbatively. We first find the linear growing mode $\phi_a^{(1)}(\mathbf{k}) = \delta_0(\mathbf{k})(1, 1)$ so that the decaying part of the Green's function (Equation 4.12) vanishes. Then, the second order kernels at time η are

given by Equation 4.17 using the linear growing kernel of $\mathcal{F}_a^{(1)} = e^{\eta}(1,1)$. While the time integral in Equation 4.17 gives rise to a slowly growing mode ($\propto e^{\eta}$) and a decaying mode ($\propto e^{-\frac{3}{2}\eta}$), these are exactly canceled by the initial fastest-growing kernels $\mathcal{T}_a^{(2)} = (F_2^{(s)}, G_2^{(s)})$ defined by the kernels in SPT (Bernardeau et al. 2002) and we are left with the fastest-growing solution of $\mathcal{F}_2^{(n)}(\eta) = e^{2\eta}(F_2^{(s)}, G_2^{(s)})$.

The same is true for all the higher order kernels, and the fastest growing solutions are

$$\Psi_a^{(n)}(\mathbf{k},\eta) = (2\pi)^3\delta_D(\mathbf{k}-\mathbf{k}_1-\cdots-\mathbf{k}_n)\mathcal{F}_a^{(n)}(\mathbf{k}_1,..,\mathbf{k}_n,\eta)\delta_0(\mathbf{k}_1)\cdots\delta_0(\mathbf{k}_n), \quad (4.18)$$

where

$$\mathcal{F}_a^{(n)}(\eta) = e^{n\eta}\left(F_n^{(s)}, G_n^{(s)}\right) \quad (4.19)$$

are the SPT kernels mentioned in Section 1.3.3. The recursive formulae for these kernels can be found in Appendix A.

When the single fluid approximation is valid (at early times and on large scales), ideal N-body simulations must reproduce the density and velocity fields in 4.18 with the growing mode kernels 4.19. To satisfy this condition, we must start simulations with initial density and velocity fields satisfying 4.18.

4.2.2 The Tree-level Bispectrum

Using the definition of the bispectrum (Equation 4.2), we can now compute the leading-order (tree-level) growing mode of the bispectrum in terms of the second order

kernel $F_2^{(s)}$ (Equation 1.25):

$$B(k_1, k_2, k_3) = 2e^{4\eta} F_2^{(s)}(\mathbf{k}_1, \mathbf{k}_2) P_L(k_1) P_L(k_2) + (2 \text{ cyclic}) \ , \tag{4.20}$$

where the cyclic terms are the (ordered) permutations of k_1, k_2, and k_3.

Figure 4.1 shows two visualizations of the tree-level bispectrum. The top figure shows the bispectrum, calculated in bins of (k_1, k_2, k_3), with $\delta k = 0.005h/\text{Mpc}$, flattened into a 1-dimensional vector. We have imposed the constraint $k_1 \geq k_2 \geq k_3$ without loss of generality. The vertical lines in this figure separate slices of k_1, and the value of k_1 in several slices is shown at the bottom of the figure. This type of plot is useful for comparing multiple bispectra on one axis.

The lower plot in Figure 4.1 shows the bispectrum in just one of these slices, at $k_1 = 0.2h/\text{Mpc}$. We have normalized the bispectrum by its maximum value in this slice. This figure is useful for studying the shape-dependence of the bispectrum. The locations of some specific triangular configurations are shown. One can see that the signal is highest in the elongated configuration ($k_1 = k_2 + k_3$), with a suppression at squeezed triangles ($k_1 \approx k_2 \gg k_3$), and lowest signal in isosceles ($k_2 = k_3$) and equilateral ($k_1 = k_2 = k_3$) configurations at this scale.

4.2.3 Transients from Initial conditions

Generating the fastest-growing initial conditions at all orders in perturbation theory is quite non-trivial. This is in part because we simulate N-body dynamics with

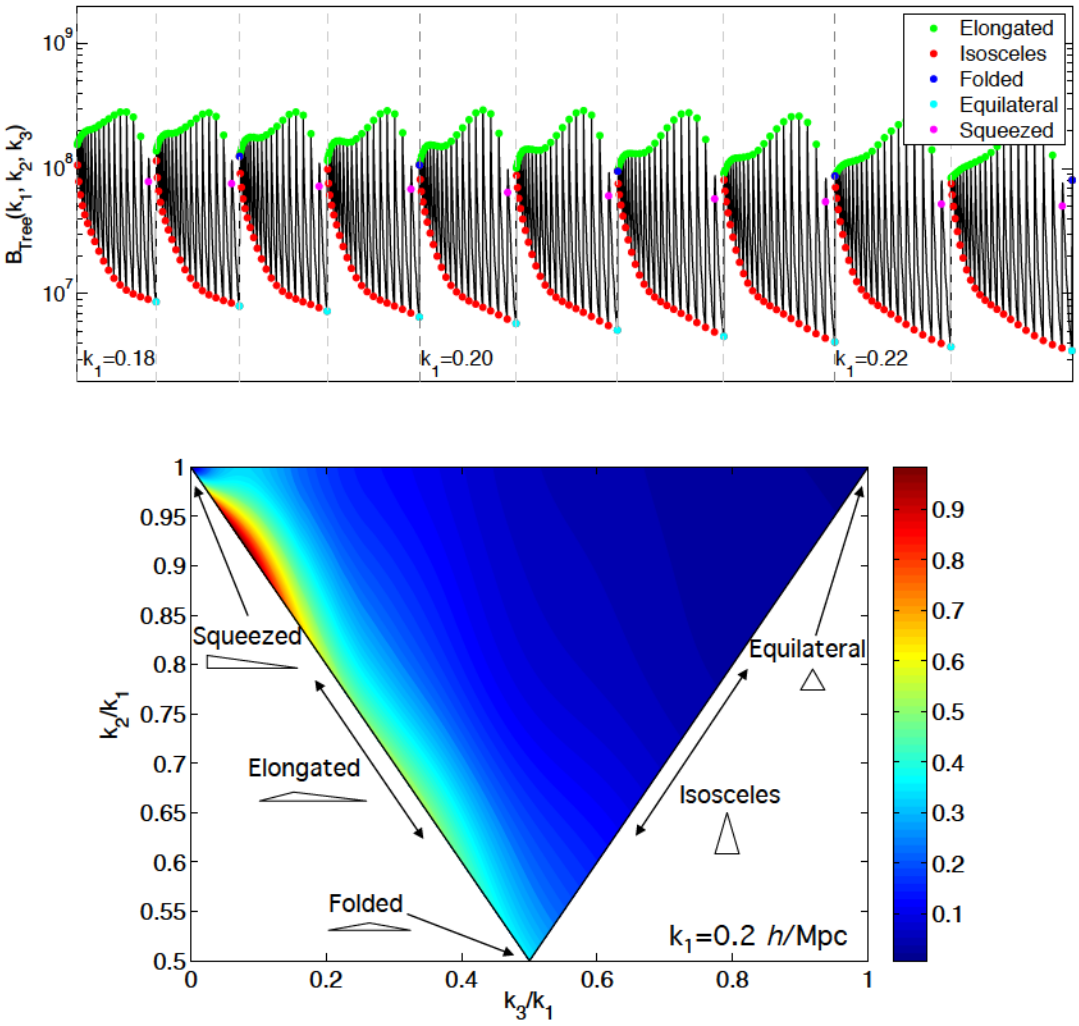

Figure 4.1: Two visualizations of the tree-level bispectrum from Standard Perturbation Theory. The top plot shows the bispectrum calculated in bins of (k_1, k_2, k_3) with $\delta k = 0.005h/\text{Mpc}$, flattened into a 1-dimensional vector. The vertical lines in this figure separate slices of k_1, and the value of k_1 in several slices is shown (in h/Mpc) at the bottom of the figure. The bottom plot shows the bispectrum in one slice at $k_1 = 0.2h/\text{Mpc}$ (normalized by its maximum value in the slice). The locations of various limiting triangular configurations are shown.

the motion of matter *particles*. That is, the initial conditions for N-body simulations are set by the position and velocity of each particle rather than set by density and velocity gradient field as is demanded by SPT. Due to the nonlinear relation between particle's position and the resulting density field, the initial conditions can only satisfy the fastest-growing condition (Equation 4.18) perturbatively, in an order-by-order manner. As a result, when generating initial conditions with the growing mode at a given order in δ_0, it is inevitable that spurious decaying modes will be excited at higher orders.

In this section, we study such decaying modes for two of the most widely used initial condition generators: first order (Zel'dovich approximation) and second order (2LPT) Lagrangian Perturbation Theory. For each initial condition generating schemes, we give the initial density and velocity kernels $\mathcal{T}_a^{(n)}$, and find the evolved kernel at the final redshift by using Equation 4.17 in order to study the resulting transients in the matter bispectrum as a function of initial and final redshifts as well as triangular configuration and scales.

In the Zel'dovich approximation, the linear order initial kernels are:

$$\mathcal{T}_a^{\mathrm{ZA},(1)} = (1, 1) \ . \tag{4.21}$$

This means the Zel'dovich approximation indeed gives rise to the growing mode solution in linear order. On the other hand, the second order initial kernels are

$$\mathcal{T}_a^{\mathrm{ZA},(2)} = \left(\frac{(\mathbf{k}\cdot\mathbf{k}_1)(\mathbf{k}\cdot\mathbf{k}_2)}{2k_1^2k_2^2}, \ \frac{k^2(\mathbf{k}_1\cdot\mathbf{k}_2)}{2k_1^2k_2^2} \right) \ , \tag{4.22}$$

which are different from the fastest-growing mode kernels of SPT in Equation 1.25. Therefore, the transients in the Zel'dovich approximation start to appear from second order, and they affect the subsequent evolution of the density and velocity fields at second order. To find the kernels at late times, we plug Equation 4.22 into Equation 4.17. We find that the 2nd order kernels are:

$$\mathcal{F}_2^{\mathrm{ZA},(2)}(\mathbf{k}_1,\mathbf{k}_2,\eta) = e^{2\eta}F_2^{(s)}(\mathbf{k}_1,\mathbf{k}_2,\eta) + \left(\mu_{12}^2-1\right)\left(\frac{3}{10}e^{\eta} - \frac{3}{35}e^{-\frac{3}{2}\eta}\right) , \tag{4.23}$$

$$\mathcal{G}_2^{\mathrm{ZA},(2)}(\mathbf{k}_1,\mathbf{k}_2,\eta) = e^{2\eta}G_2^{(s)}(\mathbf{k}_1,\mathbf{k}_2,\eta) + \left(\mu_{12}^2-1\right)\left(\frac{3}{10}e^{\eta} + \frac{9}{70}e^{-\frac{3}{2}\eta}\right) . \tag{4.24}$$

where $\mu_{ij} = \hat{\mathbf{k}}_i \cdot \hat{\mathbf{k}}_j$.

This yields transients in the leading order matter bispectrum, and the slowest-decaying transient is given by:

$$B^{\mathrm{ZA}}(k_1,k_2,k_3) - B^{\mathrm{true}}(k_1,k_2,k_3) = \frac{3}{5}\left[\frac{D}{D_i}\right]^3 \left(\mu_{12}^2-1\right) P_L(k_1)P_L(k_2) + (2 \text{ cyclic}) , \tag{4.25}$$

With Equation 4.17, one can also show that, with Zel'dovich initial conditions, the slowest-decaying transients at all higher orders ($n \geq 2$) are suppressed only by e^{η} with respect to the fastest-growing modes.

In 2LPT, the linear- and second-order initial kernels are:

$$\mathcal{T}_a^{\mathrm{2LPT},(1)} = (1,1) , \tag{4.26}$$

$$\mathcal{T}_a^{\mathrm{2LPT},(2)} = (F_2^{(s)}, G_2^{(s)}) . \tag{4.27}$$

As shown in Section 4.2.1, the density and velocity fields in 2LPT remain as

the fastest-growing modes, and an N-body simulation with 2LPT initial conditions correctly reproduces the leading order bispectrum.

On the other hand, 2LPT initial conditions differ from the fastest-growing modes at third order and higher. This generates spurious slowly growing modes and decaying modes. Again, using Equation 4.17, one can show that, for 2LPT initial conditions, the slowest-decaying modes are suppressed by two powers in the linear growth factor ($e^{-2\eta}$) with respect to the fastest growing mode at $n(\geq 3)$-th order. Therefore, we expect the following time dependence of transients:

$$B^{\rm 2LPT}(k_1, k_2, k_3) - B^{\rm true}(k_1, k_2, k_3) \propto \left[\frac{D}{D_i}\right]^2, \tag{4.28}$$

which happens on smaller scales than the Zel'dovich case because the transient only comes from next-to-leading order and beyond.

4.3 Transients from Simulations

We have reviewed the perturbation theory prediction for the error induced in the bispectrum that comes from setting initial conditions at a finite initial redshift with first- and second-order Lagrangian Perturbation Theory. In this section, we study the error induced by transients numerically with a suite of simulations with different initial redshifts, using both the Zel'dovich approximation (ZA) and 2LPT for setting the initial positions and velocities of particles. Below, we describe the details of these simulations and give a recommendation for accurate numerical modeling of the

bispectrum on nonlinear scales.

We ran 2 sets of 8 simulations, one set in a 200 Mpc/h box and the other in a 1 Gpc/h box. Each set used the same random seed to set initial conditions. This ensures that within each set, any differences we measure between the simulations are due solely to the initial conditions generator. Four of the runs in each set used ZA initial conditions, four used 2LPT, and we use the following initial redshifts in each case: $z_{\rm init} = 200, 100, 50, 25$. We also ran fiducial simulations with both box sizes using 2LPT with $z_{\rm init} = 400$, to which all other runs are compared. This is our $B^{\rm true}$. Each run had 512^3 particles, and used the following cosmological parameters ($\Omega_\Lambda = 0.7$, $\Omega_m = 0.3$), and were run using the GADGET code. The cloud-in-cell density was computed on a 1024^3 grid at $z = 6, 5, 4, 3, 2$ and 1, and used to compute the bispectrum at each redshift.

Figure 4.2 shows the fractional error in the measured bispectrum, as compared to the fiducial bispectrum, at $z = 1$ in both the large (left) and small (right) boxes, from 2LPT (top) and ZA (bottom) initial conditions. The various initial redshifts are shown in different colors. As expected, the error from the ZA simulations is significantly larger on all scales than in the 2LPT simulations, because the ZA transients appear at tree-level as opposed to 1-loop. In order to accurately model the nonlinear bispectrum numerically, we suggest using 2LPT initial conditions with an initial redshift $z_{\rm init} \geq 100$. For $z_i = 100$, the error from transients is less than 3% in the (low-resolution) large-box simulation and less than 1% in the small-box simulation

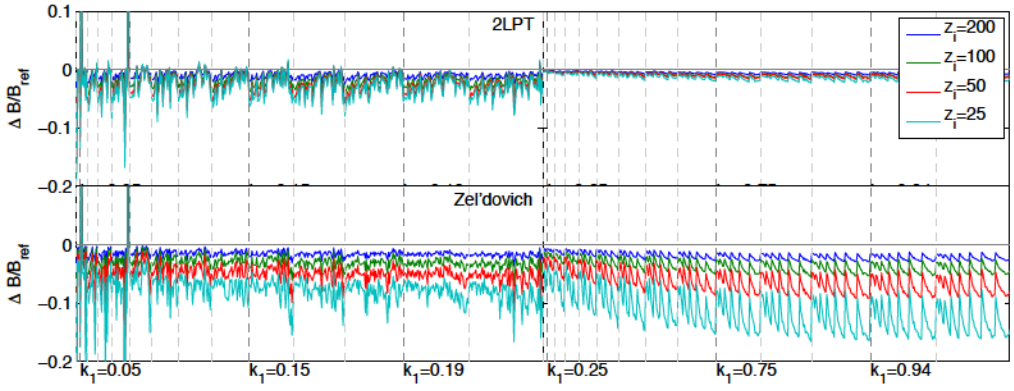

Figure 4.2: Error induced by transients in the measured bispectrum at $z = 1$ using Zel'dovich and 2LPT initial conditions with different initial redshifts. The left column shows the results from the large-box simulation and the right column shows the small-box simulation. The top panels show the error in simulations using 2LPT initial conditions and the bottom panels show the error from Zel'dovich initial conditions.

at $z = 1$. At high redshift, the errors are on the order of 10% (large box) and $< 2\%$ (small box). For $z_i = 200$, at $z = 1$ the transient errors are about 2% and $< 1\%$, and at $z = 6$ the errors are 5% and $< 2\%$.

Another consideration is the shape-dependence of the bispectrum transients. Figure 4.3 shows the transient signal ($\Delta B = B - B^{\rm true}$; top) and transient error ($\Delta B/B^{\rm true}$; bottom) at $k_1 = 0.2h/\text{Mpc}$ (normalized to -1). On the left is the prediction from SPT for the transients from ZA initial conditions. The middle column shows the signal and error measured from the the $z_i = 200$ ZA simulation at $z = 1$. The right column shows the same for the 2LPT simulation with $z_i = 200$.

While Figure 4.2 clearly shows that the 2LPT transients have a much smaller amplitude than the ZA transients, Figure 4.3 shows that they have the same shape-dependence. The measured shape dependence of the transient signal (top panels) agrees reasonably well with the SPT prediction, except for in the elongated configuration, where the measured signal is more negative than predicted. However, the shape-dependence of the measured error (bottom panels) agrees better to the predicted transient error (bottom panels) in all configurations. The transient error is greatest in the equilateral configuration, and smallest in the elongated configuration for both ZA and 2LPT initial conditions. We found that the shape dependence of the transients is independent of redshift in both cases.

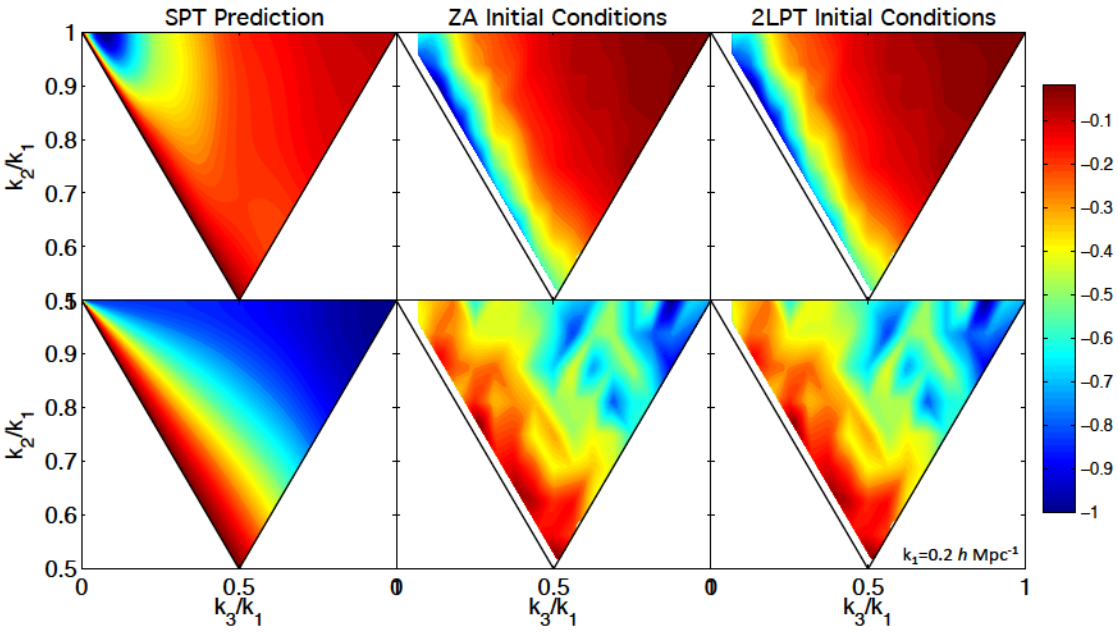

Figure 4.3: Shape dependence of the transient signal and error in the measured bispectrum at $k_1 = 0.2h/\mathrm{Mpc}$ at $z = 1$ from Zel'dovich and 2LPT initial conditions compared to the SPT prediction. The top panels show the transient signal, which is highest in the squeezed and elongated configurations. The bottom panels show the error, which is highest in the equilateral configuration.

4.4 Phenomonological Models

We now test the accuracy of various theoretical templates for the nonlinear bispectrum against the measured matter bispectrum from N-body simulations. For comparison, we use the result of $z_{\rm init} = 400$ (2LPT) simulation, as the nonlinear matter bispectra measured from other 2LPT simulations converge to it, and the transient signal will be very small in this simulation.

On large enough scales, the leading order (tree level) prediction in Equation 4.20 is enough to model the matter bispectrum. Modeling the matter bispectrum on smaller scales where nonlinearities become stronger, however, requires more elaborate calculation.

On quasi-linear scales, we expect the next-to-leading order (one-loop) bispectrum in SPT to model the nonlinear evolution reasonably well. The next-to-leading order matter bispectrum is given by four additional one-loop terms (Bernardeau et al. 2002):

$$\begin{aligned} B^{\rm 1loop}(k_1,k_2,k_3) =& B^{\rm tree}(k_1,k_2,k_3) + B^{(222)}(k_1,k_2,k_3) + B^{(123a)}(k_1,k_2,k_3) \\ &+ B^{(123b)}(k_1,k_2,k_3) + B^{(114)}(k_1,k_2,k_3) \ , \end{aligned} \tag{4.29}$$

where $B^{\rm tree}$ is the leading order bispectrum in Equation 4.20 and

$$B^{(222)}(k_1,k_2,k_3) = 8\int \frac{d^3q}{(2\pi)^3} F_2^{(s)}(\mathbf{q},\mathbf{k}_1-\mathbf{q})F_2^{(s)}(-\mathbf{q},\mathbf{k}_2+\mathbf{q})F_2^{(s)}(\mathbf{q}-\mathbf{k}_1,-\mathbf{k}_2-\mathbf{q}) \times P_L(q)P_L(|\mathbf{k}_1-\mathbf{q}|)P_L(|\mathbf{k}_2+\mathbf{q}|)\ , \tag{4.30}$$

$$B^{(114)}(k_1,k_2,k_3) = 12P_L(k_2)P_L(k_3)\int \frac{d^3q}{(2\pi)^3} P_L(q) \times F_4^{(s)}(\mathbf{q},-\mathbf{q},-\mathbf{k}_2,-\mathbf{k}_3) + (2\text{ cyc.})\ , \tag{4.31}$$

$$B^{(123a)}(k_1,k_2,k_3) = 6P_L(k_1)\int \frac{d^3q}{(2\pi)^3} P_L(q)P_L(|\mathbf{k}_2-\mathbf{q}|) \times F_2^{(s)}(\mathbf{q},\mathbf{k}_2-\mathbf{q})F_3^{(s)}(-\mathbf{q},\mathbf{q}-\mathbf{k}_2,-\mathbf{k}_1) + (5\text{ cyc.})\ , \tag{4.32}$$

$$B^{(123b)}(k_1,k_2,k_3) = 6P_L(k_1)P_L(k_3)F_2^{(s)}(\mathbf{k}_1,\mathbf{k}_3) \times \int \frac{d^3q}{(2\pi)^3} F_3^{(s)}(\mathbf{q},-\mathbf{q},\mathbf{k}_3)P_L(q) + (5\text{ cyc.}), \tag{4.33}$$

are non-linear corrections with $F_n^{(s)}$ being symmetric kernels encoding the fastest growing mode of the nonlinear density evolution (see Appendix A for density kernels). Note that the expression above is completely determined by the given linear matter power spectrum $P_L(k)$.

On smaller scales where SPT breaks down due to strong nonlinearities, various phenomenological models have been proposed as an alternative way of predicting the nonlinear behavior of the matter bispectrum. Here, we consider three such models for the nonlinear matter bispectrum.

The simplest model that we consider is PT+, where we attribute the entirety of the nonlinearities in the matter bispectrum to the nonlinear matter power spectrum. This leads to an expression that is identical to Equation 4.20, but uses the measured

(fully-nonlinear) power spectrum from the N-body simulation in place of the linear power spectrum:

$$B(k_1, k_2, k_3) = 2F_2^{(s)}(\mathbf{k}_1, \mathbf{k}_2)P(k_1)P(k_2) + (2 \text{ cyc.}) \ . \tag{4.34}$$

This model is motivated from the expression of the one-loop bispectrum in Equation 4.29, which can be written as $B^{1\text{loop}}(k_1, k_2, k_3) = 2F_2^{(s)}(\mathbf{k}_1, \mathbf{k}_2)P_{1\text{loop}}(k_1)P_{1\text{loop}}(k_2) + 2(\text{cyc.})+(\text{irreducible terms})$, with the one-loop power spectrum $P_{1\text{loop}}(k)$. In the language of the renormalized perturbation theory (Crocce & Scoccimarro 2006), PT+ corresponds to fixing the 'vertex' (the kernel $F_2^{(s)}$) while using the renormalized propagator (power spectrum $P(k)$).

PT+ is a simplified version of the fitting formula proposed by Scoccimarro & Couchman (2001) (hereafter, SC), where the $F_2^{(s)}$ kernel in Equation 4.34 is replaced by the *effective* kernel F_2^{eff} as follows:

$$\begin{aligned} F_2^{\text{eff}}(\mathbf{k}_i, \mathbf{k}_j) = \frac{5}{7}a(n_i, k_i)a(n_j, k_j) \\ + \frac{1}{2}\cos(\theta_{ij})\left(\frac{k_i}{k_j} + \frac{k_j}{k_i}\right)b(n_i, k_i)b(n_j, k_j) \\ + \frac{2}{7}\cos^2(\theta_{ij})c(n_i, k_i)c(n_j, k_j) \ . \end{aligned} \tag{4.35}$$

Here, θ_{ij} is the angle between two wavevectors $\mathbf{k}_i$ and $\mathbf{k}_j$, and F_2^{eff} reduces to the PT kernel in Equation 1.25 when $a = b = c = 1$. The three functions $a(n, k)$, $b(n, k)$, $c(n, k)$ are functions of the wavenumber k and the effective slope of the linear power

spectrum $n \equiv d\ln P_L(k)/d\ln k$:

$$a(n,k) = \frac{1+\sigma_8^{a_6}(z)[0.7Q_3(n)]^{1/2}(qa_1)^{n+a_2}}{1+(qa_1)^{n+a_2}}\,, \tag{4.36}$$

$$b(n,k) = \frac{1+0.2a_3(n+3)q^{n+3}}{1+q^{n+3.5}}\,, \tag{4.37}$$

$$c(n,k) = \frac{1+4.5a_4/[1.5+(n+3)^4](qa_5)^{n+3}}{1+(qa_5)^{n+3.5}}\,, \tag{4.38}$$

where $q \equiv k/k_{\rm nl}$, with nonlinear scale $k_{\rm nl}$ defined by the wavenumber at which the dimensionless power spectrum $\Delta^2(k) \equiv k^3P_L(k)/(2\pi^2)$ becomes unity $\Delta^2(k_{\rm nl}) \equiv 1$, and $Q_3(n) \equiv (4-2^n)/(1+2^{n+1})$. SC fit the parameters a_1 through a_6 using the bispectrum measured from P^{3}M simulations (Jenkins et al. 1998) with 256^3 particles in 240 Mpc/h box to find that $a_1 = 0.25$, $a_2 = 3.5$, $a_3 = 2$, $a_4 = 1$, $a_5 = 2$, $a_6 = -0.2$.

Recently, Gil-Marín et al. (2012) (hereafter, GM) proposed extending the SC model further with 3 additional parameters, where $a(n,k)$, $b(n,k)$ and $c(n,k)$ in the effective kernel $F_2^{\rm eff}$ are replaced by the tilded functions:

$$\tilde{a}(n,k) = \frac{1+\sigma_8^{a_6}(z)[0.7Q_3(n)]^{1/2}(qa_1)^{n+a_2}}{1+(qa_1)^{n+a_2}}\,, \tag{4.39}$$

$$\tilde{b}(n,k) = \frac{1+0.2a_3(n+3)q^{n+3}(qa_7)^{n+3+a_8}}{1+(qa_7)^{n+3.5+a_8}}\,, \tag{4.40}$$

$$\tilde{c}(n,k) = \frac{1+4.5a_4/[1.5+(n+3)^4](qa_5)^{n+3+a_9}}{1+(qa_5)^{n+3.5+a_9}}\,. \tag{4.41}$$

The definitions for n, q, $k_{\rm nl}$, and Q_3 are the same as above, except in this model $n(k)$ is smoothed so the oscillatory features from the BAO are removed (further discussion of this can be found in Gil-Marín et al. (2012)). Then, GM fit the parameters a_1 to a_9 using the measured matter bispectrum from two sets of N-body simulations,

one with $L = 2.4$ Gpc/h (768^3 particles), and one with $L_b = 1.875$ Gpc/h (1024^3 particles), to find the best-fit parameters of $a_1 = 0.484$, $a_2 = 3.740$, $a_3 = -0.849$, $a_4 = 0.392$, $a_5 = 1.013$, $a_6 = -0.575$, $a_7 = 0.128$, $a_8 = -0.722$, $a_9 = -0.926$.

Note that the conditions on which the fitting formulae are developed is quite different. While SC have used the matter bispectrum at all triangular configurations (a total of about a million triangles for $k \leq 2.3$ h/Mpc) at redshift $z = 0$ and $z = 1$, GM have only used certain configurations ($\theta_{12}/\pi = 0.1, 0.2, \cdots, 0.9$ and $k_2/k_1 = 1.0, 1.5, 2.0, 2.5$, for $k_2 < 0.4$ Mpc/h) at four different redshifts $z = 0, 0.5, 1, 1.5$. Moreover, they are subject to different levels of transient errors as the ΛCDM simulations used by SC are generated at $z_{\rm init} = 30$ with the Zel'dovich approximation, and the simulations used by GM are generated by 2LPT at $z_{\rm init} = 19$ (2.4 Gpc/h box) and $z_{\rm init} = 49$ (1.875 Gpc/h box).

To test the validity of each of the phenomenological formulae outside of the dynamical (Fourier) ranges and redshift ranges at which the models are fitted for, we compare the model predictions to measured bispectra at redshifts $1 < z < 6$ in both large-scale (1 Gpc/h) and small-scale (200 Mpc/h) simulations. We compare these to the predictions from tree-level PT, PT+, and 1-loop PT. For both the SC and GM models, we calculate the effective slope of the linear power spectrum $n(k)$ from the BAO-smoothed linear power spectrum which provides better agreement than the $n(k)$ including BAO.

First, we check that we can reproduce the results from Gil-Marín et al. (2012)

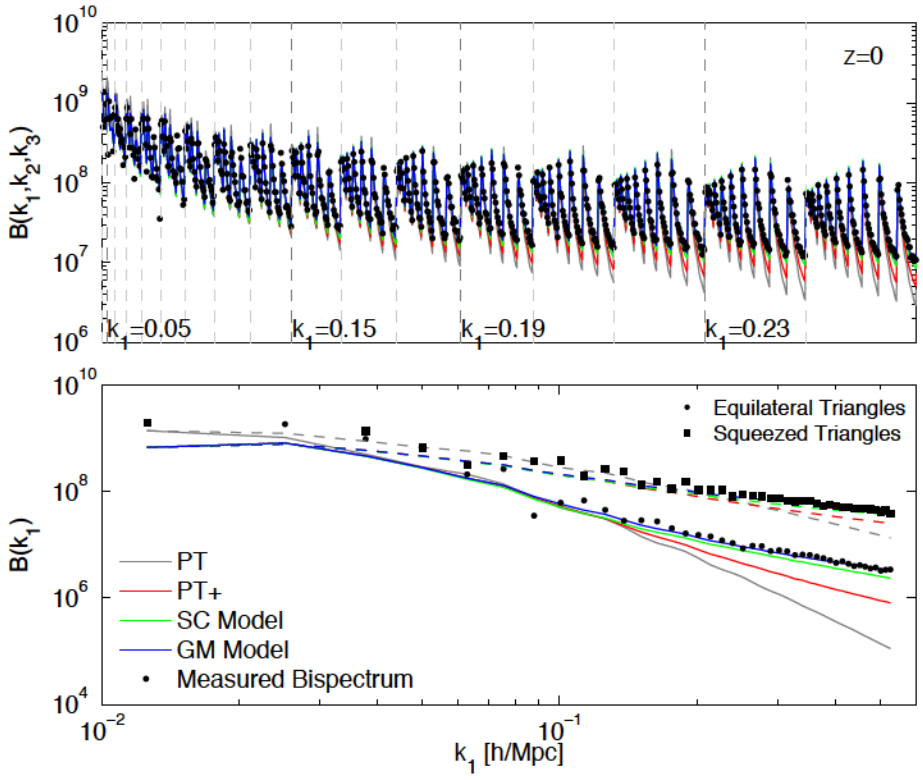

Figure 4.4: The bispectrum at $z = 0$ measured from the 1 Gpc/h simulation, compared to the SC (green), GM (blue), PT (grey), and PT+ (red) models. The top plot shows the full flattened bispectrum, and the bottom plot shows only the squeezed and equilateral triangles as a function of k_1.

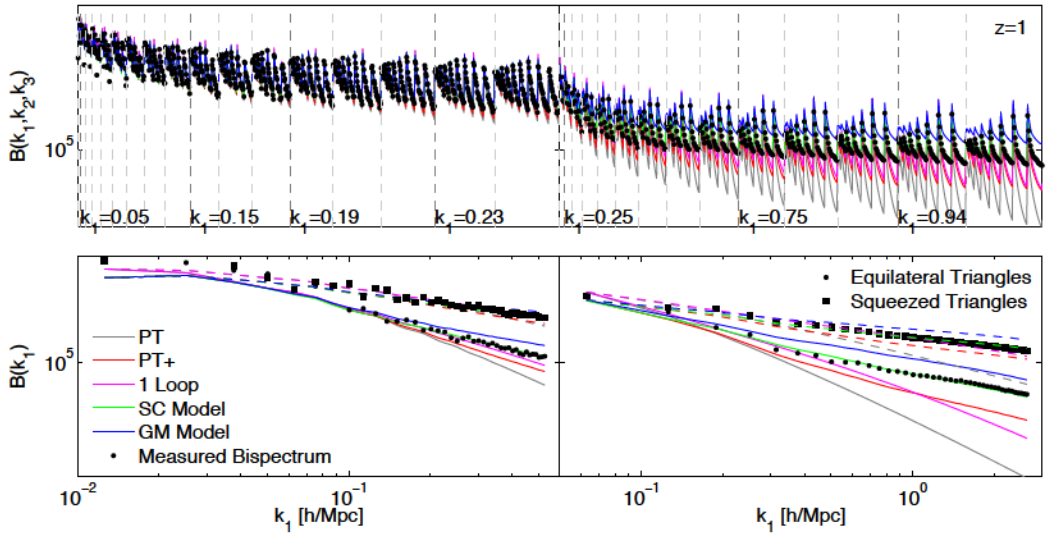

Figure 4.5: The bispectrum at $z = 1$ measured from the large-box (left) and small-box (right) simulations, compared to the SC (green), GM (blue), PT (grey), and PT+ (red) models. The top plot shows the full flattened bispectrum, and the bottom plot shows only the squeezed and equilateral triangles as a function of k_1.

at $z = 0$ on large scales. We expect that the GM model is the most accurate here, because their model parameters were fit from a similar simulation. Figure 4.4 shows the measured bispectrum at $z = 0$ from the 1 Gpc/h simulation, compared to the SC and GM models, as well as PT and PT+. The top plot shows the full flattened bispectrum, and the bottom plot shows only the squeezed and equilateral triangles as a function of k_1. We can see that the GM model fits the data best on these scales at $z = 0$.

Next we look at $z = 1$ in both the 1 Gpc/h and 200 Mpc/h simulations. Figure 4.5 compares the measured bispectrum to the models at $z = 1$. The left column

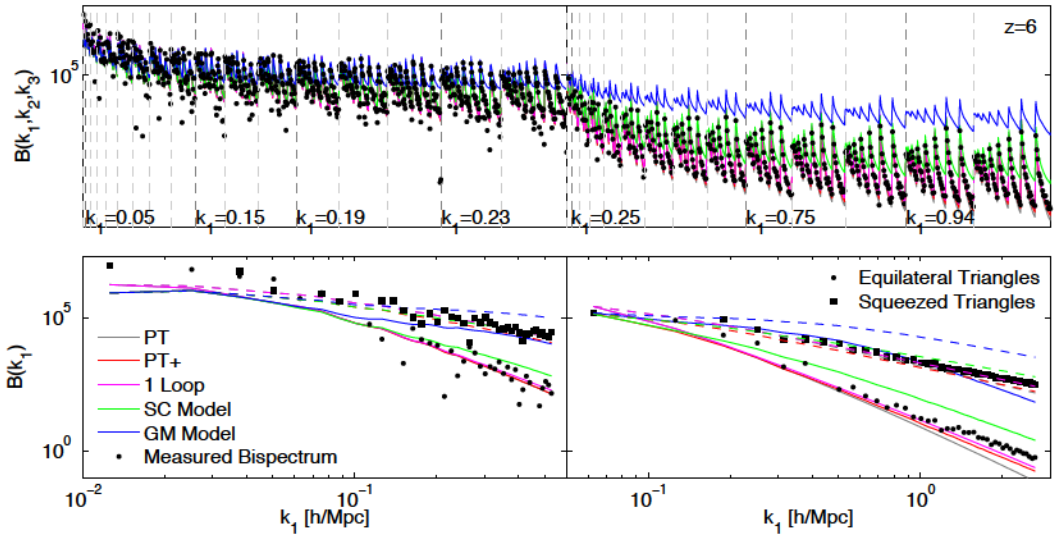

Figure 4.6: The bispectrum at $z = 6$ measured from the large-box (left) and small-box (right) simulations, compared to the SC (green), GM (blue), PT (grey), and PT+ (red) models. The top plot shows the full flattened bispectrum, and the bottom plot shows only the squeezed and equilateral triangles as a function of k_1.

shows the results from the large-box simulation, and the right shows the small-box simulation. Note that the k_1 range in the bottom plots overlaps, but we plot the results from the two simulations separately for clarity. Also note that the measured signal for squeezed triangles from the two simulations will be slightly different due to the different resolutions. From these plots, we see that even at this relatively low redshift, the SC model predicts the measured bispectrum better than the updated GM model, especially on small scales for equilateral triangles.

At higher redshift, $z = 6$, the GM model badly over-predicts the full bispectrum.

Figure 4.6 shows the measured bispectrum at $z = 6$ from both simulations compared to the models. Here, the predictions from perturbation theory (1-loop and PT+) are more accurate than either of the phenomenological models. The SC model slightly over-predicts the bispectrum on all scales.

It is clear from these comparisons that one must carefully consider the range of validity of a given model when predicting the nonlinear bispectrum. At $z = 0$ on large scales, the GM model undoubtedly gives the best prediction, but outside of that, it is safer to use the SC model. At high redshift ($z = 6$), the PT models are sufficient, and in fact in some cases better, for modeling the nonlinear bispectrum. Further work is needed to develop a more reliable model of the nonlinear bispectrum.

4.5 Conclusion

Current and future surveys promise ever-more accurate measurements of the galaxy three-point function and bispectrum. These measurements can give us a better understanding of the growth of structure, galaxy bias, and primordial non-Gaussianity. Extracting information from the galaxy 3-point function requires accurate modeling of the nonlinear dark-matter density field.

We have shown that when studying the matter bispectrum numerically, it is important to understand the effects of transients from initial conditions in simulations. Based on our suite of simulations, we recommend using 2LPT initial conditions

with $z_{\rm init} \geq 100$ to model the matter bispectrum within a few percent on scales $k < 1\ h/\mathrm{Mpc}$ at redshifts $6 \geq z \geq 1$.

Another challenge is modeling the nonlinear behavior of the bispectrum beyond tree-level perturbation theory. We have shown that the SC model is the most reliable on both large and small scales, at high and low redshift. However, other models (perturbation theory and the GM model) are more accurate in specific regimes. Further work is needed to develop a more reliable model of the nonlinear bispectrum in order to effectively extract cosmological information from the galaxy bispectrum.

Chapter 5

The 3-point Correlation Function in Real and Redshift Space

As surveys prepare to deliver vast amounts of data making higher-point statistics become more accessible, our understanding of the effects of systematics, such as nonlinearity and redshift-space distortions, on higher-point statistics must improve. By including these effects in our theoretical models of the statistics, we can more accurately constrain cosmological parameters from the data.

In Chapter 4, we discussed the challenges to modeling the nonlinear bispectrum, both numerically and analytically. The models we considered were all in real space, meaning they did not include the effects of redshift-space distortions on the bispectrum. While some attempts have been made to model the bispectrum in redshift space the results are valid over a limited range of scales and as with the power spec-

trum, the results involve integrations over complicated kernels (Scoccimarro et al. 1999; Smith et al. 2008; Marín et al. 2013). So far, there is no satisfactory model of the 3-point correlation function in redshift space. In order to access the full information of the 3-point statistics of the galaxy density field, we must model the effects of redshift-space distortions on the underlying matter density field.

In this Chapter, we show how the configuration-space approach to perturbation theory presented in Chapter 2 can be used to calculate the tree-level 3-point correlation function. In Section 5.1, we show how to perform the calculation in real space. The result agrees with a previous result found by Fourier-transforming the tree-level bispectrum from SPT. In Section 5.2 we extend our calculation to redshift space, which is not possible in the Fourier-space method. We conclude in Section 5.4

5.1 Real Space

The tree-level 3-point correlation function in real space can be computed by Fourier-transforming Equation 4.20 (Bernardeau et al. 2002). Here we derive the same result using a fully configuration-space approach.

We start with 2nd order Lagrangian Perturbation Theory (2LPT), which maps particles' initial positions $\mathbf{q}$ to their final positions $\mathbf{x}$ through the gradient of the 2nd-order potential field:

$$\mathbf{x} = \mathbf{q} - D_1 \nabla_q \phi^{(1)}(\mathbf{q}) + D_2 \nabla_q \phi^{(2)}(\mathbf{q}) \ , \tag{5.1}$$

where $D_2(\tau) \approx -\frac{3}{7}D_1^2(\tau)$ in a matter-dominated universe (Bouchet et al. 1995). The potentials are defined as:

$$\nabla_q^2 \phi^{(1)}(\mathbf{q}) = \delta_L(\mathbf{q}) = I_1(\mathbf{q}) \ , \tag{5.2}$$

$$\nabla_q^2 \phi^{(2)}(\mathbf{q}) = \sum_{i>j} \phi^{(1)}_{,ii}\phi^{(1)}_{,jj} - (\phi^{(1)}_{,ij})^2 = I_2(\mathbf{q}) \ , \tag{5.3}$$

where I_1 and I_2 are invariants of the deformation tensor d_{ij} defined in Chapter 2:

$$d_{ij}(\mathbf{q}) = \frac{\partial^2 \phi^{(1)}(\mathbf{q})}{\partial q_i \partial q_j} \ . \tag{5.4}$$

$I_1(\mathbf{q})$ is the trace of $d_{ij}(\mathbf{q})$ and $I_2(\mathbf{q})$ is the trace of the minors of $d_{ij}(\mathbf{q})$.

Using the Jacobian of the transformation from $\mathbf{q}$ to $\mathbf{x}$ we write the density to second order in 2LPT:

$$\delta(\mathbf{q}) = D\left(I_1(\mathbf{q}) + \frac{3}{7}DI_2(\mathbf{q})\right) + D^2\left(I_1(\mathbf{q})^2 - I_2(\mathbf{q})\right) + ... \tag{5.5}$$

$$= DI_1(\mathbf{q}) + D^2\left(I_1(\mathbf{q})^2 - \frac{4}{7}I_2(\mathbf{q})\right) + ... \tag{5.6}$$

We then express this as a function of $\mathbf{x}$ instead of $\mathbf{q}$ using a Taylor expansion, as we did in Chapter 2:

$$\delta(\mathbf{x}) = DI_1(\mathbf{x}) + D^2\left(I_1(\mathbf{x})^2 - \frac{4}{7}I_2(\mathbf{x}) + \nabla\phi^{(1)}(\mathbf{x}) \cdot \nabla I_1(\mathbf{x})\right) + ... \tag{5.7}$$

As we saw in Section 4.2, 2LPT correctly reproduces the 2nd-order density kernels ($F_2^{(s)}$), so the tree-level 3-point correlation function can be computed using 2LPT and will agree with the SPT result.

From the expression for the density in Equation 5.7 we can calculate the tree-level 3-point correlation function in real space:

$$\langle\delta(\mathbf{x}_1)\delta(\mathbf{x}_2)\delta(\mathbf{x}_3)\rangle = D^4\left(\left\langle\delta^{(1)}(\mathbf{x}_1)\delta^{(1)}(\mathbf{x}_2)\delta^{(2)}(\mathbf{x}_3)\right\rangle + 2 \text{ cyclic}\right) + \mathcal{O}(D^6) \ , \qquad (5.8)$$

where $\delta^{(1)}$ is the first-order density term ($I_1(\mathbf{x})$) and $\delta^{(2)}$ is the second-order density, $\left[I_1(\mathbf{x})^2 - \frac{4}{7}I_2(\mathbf{x}) + \nabla\phi^{(1)}(\mathbf{x})\cdot\nabla I_1(\mathbf{x})\right]$. The two cyclic terms are the permutations of $\mathbf{x}_1$, $\mathbf{x}_2$, and $\mathbf{x}_3$ that do not repeat.

The expectation value in Equation 5.8 is made up of three terms: $\langle I_1(\mathbf{x}_1)I_1(\mathbf{x}_2)I_1^2(\mathbf{x}_3)\rangle$, $\langle I_1(\mathbf{x}_1)I_1(\mathbf{x}_2)I_2(\mathbf{x}_3)\rangle$, and $\langle I_1(\mathbf{x}_1)I_1(\mathbf{x}_2)\nabla\phi^{(1)}(\mathbf{x}_3)\cdot\nabla I_1(\mathbf{x}_3)\rangle$. Each of these terms can be reduced to products of expectation values between two linear quantities using Wick's theorem. Each expectation value will be a function of the length of one of the sides the triangle defined by $\mathbf{x}_1$, $\mathbf{x}_2$, $\mathbf{x}_3$: $\mathbf{r}_1 = \mathbf{x}_1 - \mathbf{x}_3$, $\mathbf{r}_2 = \mathbf{x}_2 - \mathbf{x}_1$, and $\mathbf{r}_3 = \mathbf{x}_3 - \mathbf{x}_2$.

To calculate these expectation values, we start by assuming that the 3 sides of the triangle are along the line of sight direction ($\hat{z}$). In this case, the expectation values such as $\langle I_1(\mathbf{x}_1)d_{11}(\mathbf{x}_3)\rangle$ are particularly easy to calculate because $\mathbf{r}_1 = \mathbf{x}_1 - \mathbf{x}_3$ is along $\hat{z}$, so $\mathbf{k}\cdot\mathbf{r}_1 = kr\cos\theta_k$:

$$\begin{aligned}\langle I_1(\mathbf{x}_1)d_{11}(\mathbf{x}_3)\rangle &= \frac{1}{(2\pi)^3}\int P(k)\frac{k_x^2}{k^2}e^{i\mathbf{k}\cdot(\mathbf{x}_1-\mathbf{x}_3)}d^3k \\ &= \frac{1}{(2\pi)^3}\int P(k)\frac{k_x^2}{k^2}e^{ikr_1\cos\theta_k}d^3k \\ &= \frac{1}{3}\xi_0^0(r_1) + \frac{1}{3}\xi_2^0(r_1) \ . \qquad (5.9)\end{aligned}$$

All together, the line-of-sight 3-point function is:

$$\zeta_{LOS}(r_1, r_2, r_3) = D^4 \Bigg(\frac{34}{21}\xi_0^0(r_1)\xi_0^0(r_3) - \cos\theta_{31} \left(\xi_1^1(r_1)\xi_1^{-1}(r_3) + \xi_1^{-1}(r_1)\xi_1^1(r_3)\right) + \frac{8}{21}\xi_2^0(r_1)\xi_2^0(r_3) + 2 \text{ cyclic} \Bigg) . \tag{5.10}$$

Because all three legs of the triangle are along $\hat{z}$, the triangle is completely flattened, so $\theta_{12} = \pi$, and $\theta_{23} = 0$, and $\theta_{31} = 0$.

For a general triangle not along the line of sight, such as in Figure 5.1, we can imagine the vectors $\mathbf{r}_1$, $\mathbf{r}_2$, and $\mathbf{r}_3$, initially along $\hat{z}$, are rotated by angles β, β', and β'' about the y-axis. To form a triangle, the angles β' and β'' are determined by the angle β and the inner-angles of the triangle (θ_{12}, θ_{23}, and θ_{31}). These relations are given in Figure 5.1.

To calculate the expectation values in the case of a general triangle, we correspondingly rotate our coordinate system for each leg. For example, we rotate $\mathbf{r}_1$ by β, so the d'_{11} component of the deformation tensor in the new coordinate system (primed quantities) in terms of the line-of-sight quantities (unprimed) is:

$$d_{11}(\mathbf{x})' = \cos^2(\beta) d_{11}(\mathbf{x}) - 2\cos(\beta)\sin(\beta) d_{13}(\mathbf{x}) + \sin^2(\beta) d_{33}(\mathbf{x}) . \tag{5.11}$$

The expectation value $\langle I_1(\mathbf{x}_1) d'_{11}(\mathbf{x}_3)\rangle$ in the new coordinate system becomes:

$$\begin{aligned} \langle I_1(\mathbf{x}_1) d_{11}(\mathbf{x}_3)'\rangle &= \cos^2(\beta) \langle I_1(\mathbf{x}_1) d_{11}(\mathbf{x}_3)\rangle - 2\cos(\beta)\sin(\beta) \langle I_1(\mathbf{x}_1) d_{13}(\mathbf{x}_3)\rangle \\ &\quad + \sin^2(\beta) \langle I_1(\mathbf{x}_1) d_{33}(\mathbf{x}_3)\rangle \\ &= \frac{1}{3}\xi_0^0(r_1) + \frac{1}{6}\left(3\cos(2\beta) - 1\right)\xi_2^0(r_1) . \end{aligned} \tag{5.12}$$

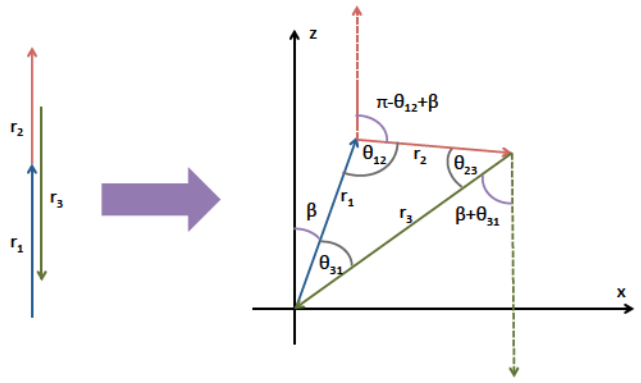

Figure 5.1: Schematic for calculating the 3-point correlation function for a general triangular configuration in real space. Given r_1, r_2, and r_3 along the line-of-sight (left), we can construct a triangle by rotating each leg by some angle about the y axis to get a triangle in the x-z plane, as shown. The 3 rotation angles can be related through the rotation angle of r_1 (β and the inner angles of the triangle, θ_{12}, θ_{23}, and θ_{31}.

The first invariant I_1 remains unchanged because it is invariant under rotations.

The r_3 leg of the triangle is rotated by angle $\beta + \theta_{31}$, so the same expectation value between $\mathbf{x}_2$ and $\mathbf{x}_3$ will be:

$$\begin{aligned}\langle I_1(\mathbf{x}_2) d_{11}(\mathbf{x}_3)' \rangle &= \cos^2(\beta+\theta_{31}) \langle I_1(\mathbf{x}_2) d_{11}(\mathbf{x}_3) \rangle + \sin^2(\beta+\theta_{31}) \langle I_1(\mathbf{x}_2) d_{33}(\mathbf{x}_3) \rangle \\ &\quad - 2\cos(\beta+\theta_{31})\sin(\beta+\theta_{31}) \langle I_1(\mathbf{x}_2) d_{13}(\mathbf{x}_3) \rangle \\ &= \frac{1}{3}\xi_0^0(r_3) + \frac{1}{6}\left(3\cos(2(\beta+\theta_{31})) - 1\right)\xi_2^0(r_3) \ . \end{aligned} \tag{5.13}$$

If we add up all of the terms in the 3-point correlation function we get:

$$\begin{aligned}\zeta(r_1, r_2, r_3) = D^4 \Bigg(&\frac{34}{21}\xi_0^0(r_1)\xi_0^0(r_3) - \cos\theta_{31}\left(\xi_1^1(r_1)\xi_1^{-1}(r_3) + \xi_1^{-1}(r_1)\xi_1^1(r_3)\right) \\ &+ \frac{2}{21}\left(1 + 3\cos 2\theta_{31}\right)\xi_2^0(r_1)\xi_2^0(r_3) + 2 \text{ cyclic} \Bigg) \ . \end{aligned} \tag{5.14}$$

We can see that this is equal to equation 5.10 for $\theta_{31} = 0$, $\theta_{12} = \pi$, and $\theta_{23} = 0$. This expression is equivalent to that given in Bernardeau et al. (2002), found by Fourier-transforming the tree-level bispectrum from SPT.

5.2 Redshift Space

Unlike the in Fourier-space approach, we can easily extend this calculation to redshift space. The transformation from real to redshift space is:

$$\mathbf{s} = \mathbf{x}(\mathbf{q}) - Df(\nabla_q \phi(\mathbf{q}) \cdot \hat{z})\hat{z} \ , \tag{5.15}$$

where $\mathbf{s}$ is the redshift-space position, f is the linear growth rate, $d\ln D/d\ln a$, and $\hat{z}$ is the line-of-sight direction.

The redshift-space density to second order is:

$$\delta_s(\mathbf{q}) = D(I_1(\mathbf{q}) + f d_{nn}(\mathbf{q})) + D^2\Bigg((I_1(\mathbf{q}) + f d_{nn}(\mathbf{q}))^2 - \frac{4}{7}\left((1+f)I_2(\mathbf{q}) - f M_{nn}(\mathbf{q})\right)\Bigg) + ... \tag{5.16}$$

where d_{nn} is the line-of-sight component of the deformation tensor, and M_{nn} is the corresponding minor of the matrix.

We write the density as a function of redshift-space coordinate s:

$$\delta_s(\mathbf{s}) = D(I_1(\mathbf{s}) + f d_{nn}(\mathbf{s})) + D^2\big((I_1(\mathbf{s}) + f d_{nn}(\mathbf{s}))^2 - \frac{4}{7}\left((1+f)I_2(\mathbf{s}) - f M_{nn}(\mathbf{s})\right) + \big(\nabla\phi^{(1)}(\mathbf{s}) + f(\nabla_q\phi^{(1)}(\mathbf{s})\cdot\hat{z})\hat{z}\big)\cdot\nabla(I_1(\mathbf{s}) + f d_{nn}(\mathbf{s}))\big) + ... \tag{5.17}$$

For a general triangle in real (isotropic) space, the angle β cancels out in the full 3-point function (equation 5.14), as expected. This is because the real-space 3-point correlation function is independent of the orientation of the triangle.

In redshift space, where the $\hat{z}$ direction is our line of sight, in general we expect the 3-point correlation function to depend on this angle. But, this is not enough to fully describe the triangle in redshift space: we also need to take into account the angle that the plane of the triangle makes with the line of sight. In the previous section, the triangle we considered in the x-z plane makes an angle $\alpha = \pi/2$ with the line of sight (see lower triangle in Figure 5.2). To describe any triangle, after rotating each side by its angle about the y-axis, we can rotate all of the sides by some angle $\phi = \pi/2 - \alpha$ about the x-axis. This is shown in the upper triangle in Figure 5.2. The

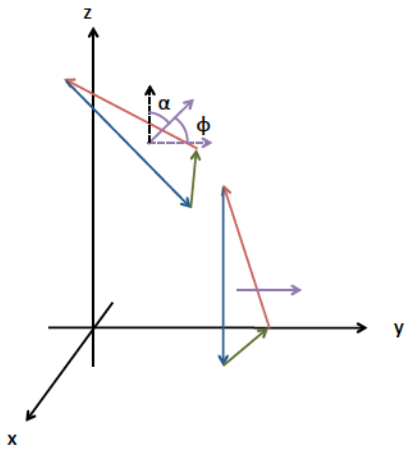

Figure 5.2: Schematic for calculating the 3-point correlation function for a general triangular configuration in redshift space. The triangle, originally in the x-z plane, is rotated about the x axis by angle ϕ.

β angle describes the orientation of $\mathbf{r}_1$ within the plane of the triangle, with respect to the rotated $\hat{z}$ axis.

To calculate the expectation values in redshift space, we must include the additional rotation by ϕ about the $\mathbf{x}$ axis. In this new coordinate system (double primed quantities), $d_{11}(\mathbf{x})''$ is unchanged:

$$d_{11}(\mathbf{x})'' = \cos^2(\beta)d_{11}(\mathbf{x}) - 2\cos(\beta)\sin(\beta)d_{13}(\mathbf{x}) + \sin^2(\beta)d_{33}(\mathbf{x}) \ , \tag{5.18}$$

and $d_{22}(\mathbf{x})''$ is now:

$$\begin{aligned} d_{22}(\mathbf{x})'' = {} & \cos^2(\phi)d_{22}(\mathbf{x}) + \cos^2(\beta)\sin^2(\phi)d_{33}(\mathbf{x}) + \cos(\beta)\sin(2\phi)d_{23}(\mathbf{x}) \\ & + \sin(2\phi)\sin(\beta)d_{12}(\mathbf{x}) + \sin^2(\phi)\sin^2(\beta)d_{11}(\mathbf{x}) + \sin^2(\phi)\sin(2\beta)d_{13}(\mathbf{x}) \ . \end{aligned} \tag{5.19}$$

For the redshift-space correlation function, we use $\delta^{(1)}$ and $\delta^{(2)}$ from Equation 5.17, and calculate the expectation values in the same way as described above. The resulting expression, which is a function of s_1, s_2, s_3, $\phi = \pi/2 - \alpha$, and β, as well as the growth rate f, contains many terms involving products of the linear correlation functions $\xi_n^m(r)$. To simplify slightly, we marginalize over the β dependence, because we are more interested in dependence on α:

$$\zeta_\alpha(s_1, s_2, s_3, \alpha) = \frac{1}{2\pi} \int_0^{2\pi} \zeta(s_1, s_2, s_3, \alpha, \beta)\ d\beta\ . \tag{5.20}$$

The expression for $\zeta_\alpha(r_1, r_2, r_3, \alpha)$ can be written in the following way:

$$\zeta_\alpha(r_1, r_2, r_3, \alpha) = \sum_{\ell=0}^{8} \sum_{m=-1}^{1} \sum_{n_1,n_2=0}^{5} f^{\ell/2} A^{\ell,m}_{n_1,n_2}(f, x) \xi^m_{n_1}(r_1) \xi^{-m}_{n_2}(r_2) \mathcal{P}_\ell(\cos\alpha) \tag{5.21}$$

$$+ \text{(2 cyclic)}\ ,$$

where x is the cosine of the corresponding inner-angle of the triangle (here, $x = \cos\theta_{12}$). The $A^{\ell,m}_{n_1,n_2}$ terms are given in Appendix C, grouped by multipole ℓ.

5.3 Discussion

We now look at the theoretical predictions made in Section 5.2 for the real- and redshift-space 3-point correlation functions. In order to verify our results, we also look at preliminary comparisons to N-body simulation data.

We first consider the monopole in redshift space, which is defined as:

$$\zeta_0(s_1, s_2, s_3) = \int_{-\pi/2}^{\pi/2} \zeta_\alpha(s_1, s_2, s_3, \alpha) \sin\alpha\ d\alpha\ . \tag{5.22}$$

The integral picks out only the $\ell = 0$ terms in Equation 5.21.

Figure 5.3 shows the 3-point correlation function of several isosceles configurations in real and redshift space. It shows the 3-point correlation function of equilateral triangles in real space (black line), redshift-space monopole (blue line), and ζ_α for $\alpha = 0$ (dashed green line), and $\alpha = \pi/2$ (dot-dashed green line). The upper left panel shows equilateral triangles, the upper right shows $r_2 = r_3 = 2r_1$, and so on. Notice that the monopole term is similar (but not equivalent to) the real-space prediction in these configurations. Also, the signal from triangles along the plane of the sky ($\alpha = 0$) is boosted compared to that from triangles perpendicular to the plane of the sky ($\alpha = \pi/2$). This is similar to what we see in the 2-point correlation function in redshift space.

We can also look at the reduced 3-point correlation function:

$$Q_\alpha(s_1, s_2, s_3, \alpha) = \frac{\zeta_\alpha(s_1, s_2, s_3, \alpha)}{\xi_s^{(1)}(s_1)\xi_s^{(1)}(s_2) + \xi_s^{(1)}(s_1)\xi_s^{(1)}(s_3) + \xi_s^{(1)}(s_2)\xi_s^{(1)}(s_3)} , \tag{5.23}$$

where

$$\xi_s^{(1)}(s) = \left(1 + \frac{2f}{3} + \frac{f^2}{5}\right) \xi_L(s) , \tag{5.24}$$

is the angular-averaged (monopole) linear correlation function in redshift space.

Figure 5.4 shows the dependence of the tree-level reduced 3-point correlation function on opening angle (θ_{12}) for $r_1 = 10$ and 20 Mpc/h, for different ratios of r_2/r_1 in real and redshift space. The left panels show the real-space prediction and the right panels show Q_α for $\alpha = 0$ (dashed lines) and $\alpha = \pi/2$ (solid lines). We can see again

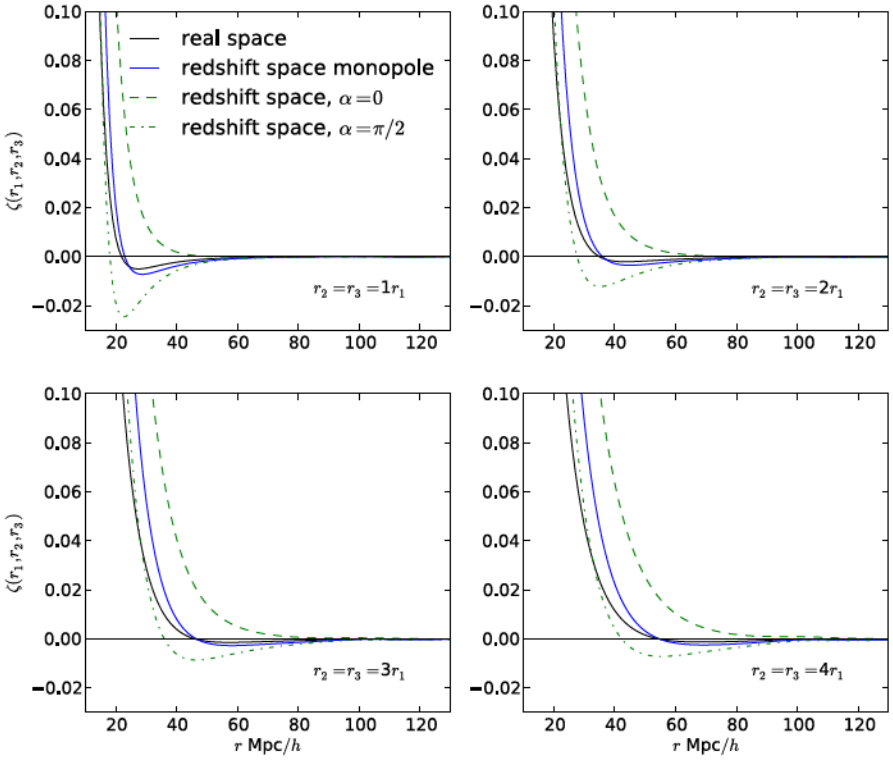

Figure 5.3: The 3-point correlation function of several isosceles triangle configurations for real space (black lines), redshift space monopole (blue line), redshift-space for $\alpha = 0$ (dashed green line), and $\alpha = \pi/2$ (dot-dashed green line). The upper left panel shows equilateral triangles, upper right shows $r_2 = r_3 = 2r_1$, lower left shows $r_2 = r_3 = 3r_1$, lower right shows $r_2 = r_3 = 4r_1$.

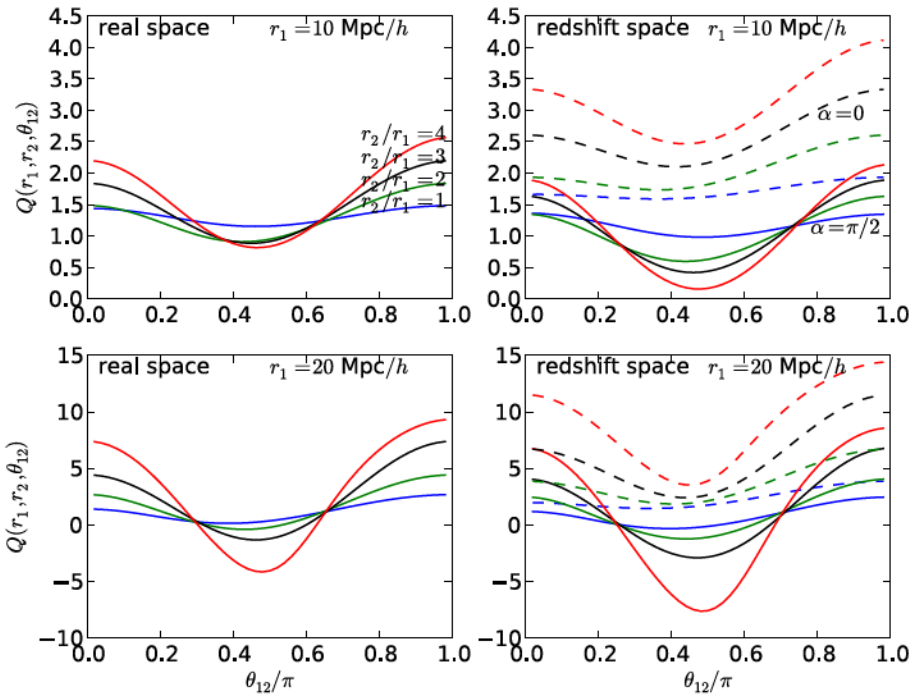

Figure 5.4: Reduced 3-point correlation function in real and redshift space as a function of opening angle, θ_{12} for $r_1 = 10$ (top panels) and 20 Mpc/h (bottom panels). The left panel shows the real-space reduced bispectrum and the right panel shows the redshift-space bispectrum for $\alpha = 0$ (dashed lines) and $\alpha = \pi/2$ (solid lines).

that for $\alpha = 0$, Q_α is boosted compared to $\alpha = \pi/2$. Also, the dip at $\theta_{12} = \pi/2$ in the reduced bispectrum is deeper for the $\alpha = \pi/2$ case.

It is clear that redshift-space distortions have a considerable effect on the 3-point statistics of the matter density, introducing a dependence on orientation from the line-of-sight direction that does not exist in real space.

Next, we compare our prediction for the angular-averaged 3-point correlation func-

tion (monopole) to measurements from an N-body simulation. We use 4 dark-matter realizations, each a 1 $(\mathrm{Gpc}/h)^3$ box, to measure the 3-point correlation function in real and redshift space at $z = 0$. The 1024^3 particles in each simulations were subsampled to reduce computing time[1].

The 3-point correlation function was measured in each volume in both real and redshift space (monopole). Figure 5.5 shows the 3-point correlation function for triangles with $s_1 = 20$ Mpc$/h$, $s_2 = 40$ Mpc$/h$ (left panel) as well as $s_1 = 30$ Mpc$/h$, $s_2 = 60$ Mpc$/h$ (right panel). The error bars are estimated using the standard deviation of the measured signal in the four realizations. The theoretical prediction for real space (Equation 5.14) and redshift-space monopole (Equation 5.22) are shown in blue and red solid lines, respectively.

Our expression for the angular-averaged (monopole) 3-point correlation function in redshift space appears to be valid on large scales compared to that measured from the Indra simulations. However, the prediction for the monopole, as well as the higher multipoles of ζ_α, should be verified through further comparisons with N-body simulations on a range of scales and triangular configurations.

[1]The Indra simulations were run by Jie Wang at Johns Hopkins University and 3-point function measurements are courtesy of Felipe Marin at Swinburne University.

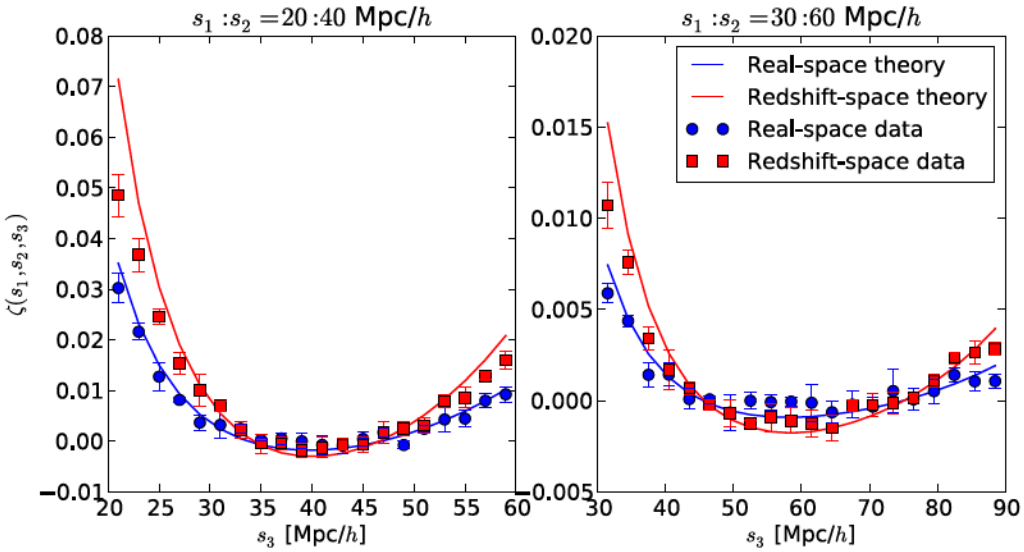

Figure 5.5: The tree-level 3-point correlation function in real space (blue line) and redshift space (red line) compared to measurements from an N-body simulation in real space (blue dots) and redshift space (red squares). The left panel shows triangles with $s_1 = 20$ Mpc/h, $s_2 = 40$ Mpc/h, and the right panel shows triangles with $s_1 = 30$ Mpc/h, $s_2 = 60$ Mpc/h.

5.4 Conclusion

Modeling redshift-space distortions in Fourier space involves integration over complicated kernels and quickly becomes unwieldy to implement. We have shown that a configuration-space approach to perturbation theory allows us to calculate the tree-level 3-point correlation function in both real and redshift space. The calculation is mathematically straightforward, involving simple expectation values and two rotations of coordinate system. While these results are preliminary and should be verified further with numerical simulations, this approach is a promising first step to including redshift-space distortions in models of higher-point statistics of the matter density. By modeling systematics such as redshift-space distortions we can access more cosmological information from the 3-point statistics of the galaxy density field.

Chapter 6

Conclusions

The spatial distribution of matter in the universe is a powerful probe of cosmological information. Accessing this information requires accurate theoretical models of systematics such as nonlinearity and redshift-space distortions. In this thesis, I have presented a new approach to modeling nonlinearity and redshift-space distortions and highlighted the many advantages of this approach by applying it to 2-point statistics, density transformations, and 3-point statistics.

In Chapter 2, I presented the configuration-space approach to perturbation theory starting from the Zel'dovich approximation. I used this approach to calculate the nonlinear contribution to the correlation function. I verified the result analytically, through comparison to the power spectrum, and numerically, through a suite of Zel'dovich realizations. Next, I showed how this approach can be used to model the nonlinear correlation function in redshift space. While nonlinearity and redshift-

space distortions appear as difficult convolutions in Fourier-space, in configuration space they take the form of a simple sum of products of linear correlation functions. Higher-order corrections will also be simplified, as they will involve more products as opposed to more convolutions. In the future, I plan to extend this approach beyond the Zel'dovich approximation to more accurately predict the nonlinear behavior of the BAO peak in redshift space.

In Chapter 3, I considered the effects of density transformations on the bias of the BAO peak. Using configuration-space perturbation theory, I modeled the nonlinear correlation functions of various transformed fields. I found that a logarithmic transform, which produces a more Gaussian distribution, provides a less biased peak position at low redshift. In future, I plan to test this theoretical prediction using N-body simulations and apply the method to real galaxy data in order to demonstrate the improvement to constraints on dark energy.

In Chapter 4, I discussed the challenges associated with modeling the nonlinear matter bispectrum, both numerically and analytically. Using a suite of N-body simulations, I measured the error induced by transients from both Zel'dovich and 2LPT initial conditions. I found that accurate numerical modeling of the bispectrum at moderate-to-high redshifts requires simulations that use 2LPT initial conditions with an initial redshift of $z_i \geq 100$. Next, I tested the regimes of validity of several analytical and phenomenological models of the matter bispectrum. I found that while the phenomenological models work well at low redshift, the 1-loop bispectrum from SPT

is a better model at high redshifts on all scales. In order to access the full cosmological information in the galaxy bispectrum, we must develop more accurate models on a larger range of scales and redshifts.

In Chapter 5, I presented for the first time a configuration-space method for calculating the 3-point correlation function in real and redshift space. While the real-space result can be found through a Fourier-transform of the SPT bispectrum, the configuration-space approach is much simpler mathematically and more powerful because it can be extended to include redshift-space distortions. In the future, I plan to further test the validity of the redshift-space 3-point correlation function using N-body simulations. By modeling the redshift-space distortions in the matter 3-point correlation function, we can access more cosmological information in the galaxy density field.

Current and future galaxy surveys promise to deliver vast amounts of data, meaning that systematic effects will soon dominate over statistical errors in the determination of cosmological parameters. Accurate theoretical models of nonlinear gravitational evolution and redshift-space distortions are necessary to extract cosmological information from the statistics of large-scale structure. The developments presented in this thesis show that a configuration-space approach provides mathematically simpler results for the nonlinear and redshift-space statistics than the standard Fourier-space approaches in a range of applications. Configuration-space perturbation theory is a promising avenue for future work on theoretical modeling of the statistics of large-

scale structure.

Appendix A

Standard Perturbation Theory Kernels

In Standard Perturbation Theory, the density and velocity fields can be written perturbatively as:

$$\hat{\delta}(\mathbf{k},\tau) = \sum_{n=1}^{\infty} D(\tau)^n(\tau)\delta_n(\mathbf{k}) \ , \tag{A.1}$$

$$\hat{\theta}(\mathbf{k},\tau) = -\mathcal{H}f\sum_{n=1}^{\infty} D(\tau)^n(\tau)\theta_n(\mathbf{k}) \tag{A.2}$$

where $\mathcal{H}$ is the conformal Hubble rate: $\mathcal{H} = d\ln a/d\tau = aH$.

APPENDIX A. STANDARD PERTURBATION THEORY KERNELS

From the fluid equations, the terms $\hat{\delta}_n(\mathbf{k},\tau)$ and $\hat{\theta}_n(\mathbf{k},\tau)$ can be written as:

$$\delta_n(\mathbf{k}) = \int d^3\mathbf{q}_1 \cdots \int d^3\mathbf{q}_n \delta_D(\mathbf{q}_1 + \cdots + \mathbf{q}_n - \mathbf{k}) F_n(\mathbf{q}_1, ..., \mathbf{q}_n)\delta_L(\mathbf{q}_1)\cdots\delta_L(\mathbf{q}_n) \tag{A.3}$$

$$\theta_n(\mathbf{k}) = -\int d^3\mathbf{q}_1 \cdots \int d^3\mathbf{q}_n \delta_D(\mathbf{q}_1 + \cdots + \mathbf{q}_n - \mathbf{k}) G_n(\mathbf{q}_1, ..., \mathbf{q}_n)\delta_L(\mathbf{q}_1)\cdots\delta_L(\mathbf{q}_n) \tag{A.4}$$

where δ_D is the 3-dimensional Dirac-delta function. The kernels F_n and G_n are defined recursively, with $F_1 = G_1 = 1$:

$$F_n(\mathbf{q}_1,\cdots,\mathbf{q}_n) = \sum_{m=1}^{n-1} \frac{G_m(\mathbf{q}_1,\cdots,\mathbf{q}_m)}{(2n+3)(n-1)} \left[(1+2n)\frac{\mathbf{k}\cdot\mathbf{k}_1}{k_1^2} F_{n-m}(\mathbf{q}_{m+1},\cdots,\mathbf{q}_n) + \frac{k^2(\mathbf{k}_1\cdot\mathbf{k}_2)}{k_1^2 k_2^2} G_{n-m}(\mathbf{q}_{m+1},\cdots,\mathbf{q}_n) \right] \tag{A.5}$$

$$G_n(\mathbf{q}_1,\cdots,\mathbf{q}_n) = \sum_{m=1}^{n-1} \frac{G_m(\mathbf{q}_1,\cdots,\mathbf{q}_m)}{(2n+3)(n-1)} \left[3\frac{\mathbf{k}\cdot\mathbf{k}_1}{k_1^2} F_{n-m}(\mathbf{q}_{m+1},\cdots,\mathbf{q}_n) + n\frac{k^2(\mathbf{k}_1\cdot\mathbf{k}_2)}{k_1^2 k_2^2} G_{n-m}(\mathbf{q}_{m+1},\cdots,\mathbf{q}_n) \right] \tag{A.6}$$

where $\mathbf{k}_1 \equiv \mathbf{q}_1 + \cdots + \mathbf{q}_m$, $\mathbf{k}_2 \equiv \mathbf{q}_{m+1} + \cdots + \mathbf{q}_n$, $\mathbf{k} \equiv \mathbf{k}_1 + \mathbf{k}_2$, and $F_1 = G_1 = 1$.

In redshift space, we have:

$$\delta_s(\mathbf{k},t) = \sum_{n=1}^{\infty} D^n(t) \int d^3\mathbf{q}_1 \cdots \int d^3\mathbf{q}_n \delta_D(\mathbf{q}_1 + \cdots + \mathbf{q}_n - \mathbf{k}) \times Z_n(\mathbf{q}_1,\cdots,\mathbf{q}_n)\delta_L(\mathbf{q}_1)\cdots\delta_L(\mathbf{q}_n) \tag{A.7}$$

The first few kernels Z_n are:

$$Z_1(\mathbf{k}) = (1 + f\mu^2) \tag{A.8}$$

$$\begin{aligned} Z_2(\mathbf{k}_1, \mathbf{k}_2) &= F_2(\mathbf{k}_1, \mathbf{k}_2) + f\mu^2 G_2(\mathbf{k}_1, \mathbf{k}_2) \\ &\quad + \frac{f\mu k}{2}\left[\frac{\mu_1}{k_1}(1 + f\mu_2^2) + \frac{\mu_2}{k_2}(1 + f\mu_1^2)\right] \end{aligned} \tag{A.9}$$

$$\begin{aligned} Z_3(\mathbf{k}_1, \mathbf{k}_2, \mathbf{k}_3) &= F_3^{(s)}(\mathbf{k}_1, \mathbf{k}_2, \mathbf{k}_3) + f\mu^2 G_3^{(s)}(\mathbf{k}_1, \mathbf{k}_2, \mathbf{k}_3) \\ &\quad + f\mu k\left[F_2^{(s)}(\mathbf{k}_1, \mathbf{k}_2) + f\mu_{12}^2 G_2^{(s)}(\mathbf{k}_1, \mathbf{k}_2)\right]\frac{\mu_3}{k_3} \\ &\quad + f\mu k(1 + f\mu_1^2)\frac{\mu_{23}}{k_{23}} G_2^{(s)}(\mathbf{k}_2, \mathbf{k}_3) + \frac{(f\mu k)^2}{2}(1 + f\mu_1^2)\frac{\mu_2\mu_3}{k_2 k_3} \end{aligned} \tag{A.10}$$

where $\mu \equiv \mathbf{k} \cdot \hat{z}/k$, $\mathbf{k} \equiv \mathbf{k}_1 + \cdots + \mathbf{k}_n$, and $\mu_i \equiv \mathbf{k}_i \cdot \hat{z}/k_i$. Note that the third-order kernel Z_3 must still be symmetrized over its arguments.

Appendix B

The Nonlinear Redshift-space Correlation Function

The expression for the nonlinear term in the redshift-space correlation function from the Zel'dovich approximation is:

$$\xi^{(2)}(s,\mu) = \sigma_v^2 \sum_{\ell=0}^{4} f^{\ell/2} B_\ell(f) \xi_\ell^2(r) \mathcal{P}_\ell(\mu) + \sum_{\ell=0}^{8} \sum_{m=0}^{2} \sum_{n_1,n_2}^{6} f^{\ell/2} A_{n_1,n_2}^{\ell,m}(f) \xi_{n_1}^{m}(s) \xi_{n_2}^{-m}(s) \mathcal{P}_\ell(\mu) \tag{B.1}$$

where

$$\sigma_v^2 \equiv \frac{1}{6\pi^2} \int_0^\infty P_L(k) dk$$

The non-vanishing coefficients $B_\ell(f)$ and $A_{n_1,n_2}^{\ell,m}(f)$ are defined below, grouped by multipole ℓ:

APPENDIX B. THE NONLINEAR REDSHIFT-SPACE CORRELATION FUNCTION

$$B_0 = -\frac{1}{105}\left(105 + 140f + 140f^2 + 72f^3 + 15f^4\right)$$

$$A^{0,0}_{0,0} = \frac{1}{225}\left(285 + 380f + 320f^2 + 144f^3 + 27f^4\right)$$

$$A^{0,0}_{2,2} = \frac{2}{2205}\left(1785 + 2380f + 2233f^2 + 1098f^3 + 216f^4\right)$$

$$A^{0,0}_{4,4} = \frac{4}{3675}\left(105 + 140f + 140f^2 + 72f^3 + 16f^4\right)$$

$$A^{0,1}_{1,1} = -\frac{4}{525}\left(420 + 560f + 497f^2 + 234f^3 + 45f^4\right)$$

$$A^{0,1}_{3,3} = -\frac{4}{1575}\left(315 + 420f + 399f^2 + 198f^3 + 40f^4\right)$$

$$A^{0,2}_{0,0} = \frac{1}{315}\left(105 + 140f + 140f^2 + 72f^3 + 15f^4\right)$$

$$A^{0,2}_{2,2} = \frac{2}{315}\left(105 + 140f + 119f^2 + 54f^3 + 10f^4\right)$$

$$B_2 = \frac{2}{735}\left(980 + 1295f + 738f^2 + 159f^3\right)$$

$$A^{2,0}_{0,2} = -\frac{4}{315}\left(385 + 484f + 261f^2 + 54f^3\right)$$

$$A^{2,0}_{2,2} = \frac{4}{3087}\left(1309 + 1786f + 1017f^2 + 216f^3\right)$$

$$A^{2,0}_{2,4} = -\frac{16}{1715}\left(140 + 179f + 106f^2 + 24f^3\right)$$

$$A^{2,0}_{4,4} = \frac{16}{11319}\left(77 + 110f + 66f^2 + 16f^3\right)$$

$$A^{2,1}_{1,1} = -\frac{8}{525}\left(308 + 395f + 216f^2 + 45f^3\right)$$

$$A^{2,1}_{1,3} = \frac{4}{1225}\left(581 + 740f + 417f^2 + 90f^3\right)$$

$$A^{2,1}_{3,1} = \frac{4}{525}\left(399 + 510f + 283f^2 + 60f^3\right)$$

$$A^{2,1}_{3,3} = -\frac{16}{4725}\left(231 + 315f + 182f^2 + 40f^3\right)$$

$$A^{2,1}_{5,3} = \frac{16}{14553}\left(231 + 297f + 176f^2 + 40f^3\right)$$

$$A^{2,2}_{0,2} = -\frac{2}{315}\left(98 + 131f + 72f^2 + 15f^3\right)$$

$$A^{2,2}_{2,0} = -\frac{2}{63}\left(28 + 37f + 22f^2 + 5f^3\right)$$

$$A^{2,2}_{2,2} = \frac{4}{441}\left(77 + 92f + 49f^2 + 10f^3\right)$$

$$A^{2,2}_{4,2} = -\frac{16}{8085}\left(231 + 297f + 154f^2 + 30f^3\right)$$

$$B_4 = -\frac{8}{245}\left(21 + 19f + 6f^2\right)$$

$$A^{4,0}_{0,2} = \frac{8}{175}f^2\left(25 + 22f + 6f^2\right)$$

$$A^{4,0}_{2,2} = \frac{72}{1715}\left(51 + 46f + 12f^2\right)$$

$$A^{4,0}_{2,4} = -\frac{32}{3773}\left(88 + 85f + 24f^2\right)$$

$$A^{4,0}_{4,4} = \frac{144}{1226225}\left(715 + 702f + 216f^2\right)$$

$$A^{4,1}_{1,3} = \frac{48}{1225}\left(41 + 37f + 10f^2\right)$$

$$A^{4,1}_{3,1} = \frac{16}{1575}\left(251 + 227f + 60f^2\right)$$

$$A^{4,1}_{3,3} = -\frac{16}{5775}\left(231 + 217f + 60f^2\right)$$

$$A^{4,1}_{5,1} = -\frac{16}{3465}\left(121 + 109f + 30f^2\right)$$

$$A^{4,1}_{5,3} = \frac{32}{105105}\left(429 + 416f + 120f^2\right)$$

$$A^{4,2}_{2,2} = \frac{8}{735}\left(61 + 56f + 15f^2\right)$$

$$A^{4,2}_{4,0} = \frac{8}{1155}\left(55 + 52f + 15f^2\right)$$

$$A^{4,2}_{4,2} = -\frac{32}{17787}\left(143 + 119f + 30f^2\right)$$

$$A^{4,2}_{6,2} = \frac{16}{33033}\left(143 + 130f + 30f^2\right)$$

$$A^{6,0}_{2,4} = -\frac{32}{539}(13 + 6f)$$

$$A^{6,0}_{4,4} = \frac{32}{8085}(15 + 8f)$$

$$A^{6,1}_{3,3} = -\frac{32}{2079}(43 + 20f)$$

$$A^{6,1}_{5,1} = -\frac{32}{1155}(13 + 6f)$$

$$A^{6,1}_{5,3} = \frac{64}{1485}(2 + f)$$

$$A^{6,2}_{4,2} = -\frac{16}{2541}(32 + 15f)$$

$$A^{6,2}_{6,0} = -\frac{16}{693}(2 + f)$$

$$A^{6,2}_{6,2} = \frac{32}{5445}(5 + 2f)$$

$$A^{8,0}_{4,4} = \frac{128}{2145}$$

$$A^{8,1}_{5,3} = \frac{512}{6435}$$

$$A^{8,2}_{6,2} = \frac{128}{6435}$$

Appendix C

The Redshift-space 3-point Correlation Function

The redshift-space correlation function, $\zeta_s(\mathbf{s}_1, \mathbf{s}_2, \mathbf{s}_3)$ can be written as a function of the lengths of the 3 sides of the triangle defined by the redshift-space positions $\mathbf{s}_1$, $\mathbf{s}_2$, and $\mathbf{s}_3$, as well as 2 orientation angles, α and β:

$$\zeta_s(\mathbf{s}_1, \mathbf{s}_2, \mathbf{s}_3) = \zeta_s(r_1, r_2, r_3, \alpha, \beta) \ , \tag{C.1}$$

where $\mathbf{r}_1 = \mathbf{s}_1 - \mathbf{s}_3$, $\mathbf{r}_2 = \mathbf{s}_2 - \mathbf{s}_1$, and $\mathbf{r}_3 = \mathbf{s}_3 - \mathbf{s}_2$. The angle α describes the angle between the face of the triangle and the line-of-sight direction, $\hat{z}$ (so $\alpha = 0$ describes triangles on the plane of the sky). The angle β describes the orientation of the triangle within the plane of the triangle.

Because we are more interested in the dependence on α (and we expect the

dependence on β to be weaker), we marginalize over β:

$$\zeta_\alpha(r_1, r_2, r_3, \alpha) = \frac{1}{2\pi}\int_0^{2\pi} \zeta_s(r_1, r_2, r_3, \alpha, \beta) d\beta \tag{C.2}$$

The tree-level expression for $\zeta_\alpha(r_1, r_2, r_3, \alpha)$ can be written in the following way:

$$\zeta_\alpha(r_1, r_2, r_3, \alpha) = \sum_{\ell=0}^{8}\sum_{m=-1}^{1}\sum_{n_1,n_2=0}^{5} f^{\ell/2} A^{\ell,m}_{n_1,n_2}(f,x)\xi^m_{n_1}(r_1)\xi^{-m}_{n_2}(r_2)\mathcal{P}_\ell(\cos\alpha) + (2 \text{ cyclic}) \tag{C.3}$$

where x is the cosine of the inner-angle of the triangle between r_1 and r_2, f is the logarithmic derivative of the growth function, and $\xi^m_n(r)$ are the linear correlation functions, defined as:

$$\xi^m_n(r) \equiv \frac{1}{2\pi^2}\int P_L(k) j_n(kr) k^{m+2} dk \tag{C.4}$$

Here we list the non-vanishing coefficients $A^{\ell,m}_{n_1,n_2}$, grouped by multipole (ℓ) in α:

Monopole term ($\ell = 0$):

$$A^{0,0}_{0,0} = \tfrac{34}{21} + \tfrac{136f}{63} + \tfrac{6932f^2}{4725} + \tfrac{2392f^3}{4725} + \tfrac{2f^4}{25}$$

$$A^{0,0}_{2,0} = A^{0,0}_{0,2} = \tfrac{2f}{63} + \tfrac{124f^2}{6615} + \tfrac{106f^3}{33075}$$

$$A^{0,0}_{4,0} = A^{0,0}_{0,4} = -\left(\tfrac{f^2}{735} + \tfrac{f^3}{1225}\right)$$

$$A^{0,0}_{2,2} = -\left(\tfrac{4}{21} + \tfrac{8f}{21} + \tfrac{3362f^2}{6615} + \tfrac{14494f^3}{46305} + \tfrac{16f^4}{245}\right) + \left(\tfrac{4}{7} + \tfrac{20f}{21} + \tfrac{152f^2}{105} + \tfrac{1608f^3}{1715} + \tfrac{48f^4}{245}\right)x^2$$

$$A^{0,0}_{4,2} = A^{0,0}_{2,4} = \tfrac{4f^2}{735} + \tfrac{32f^3}{25725} - \left(\tfrac{2f^2}{147} + \tfrac{4f^3}{1029}\right)x^2$$

$$A^{0,0}_{4,4} = \tfrac{8f^2}{1225} + \tfrac{8f^3}{1029} + \tfrac{16f^4}{3675} - \left(\tfrac{16f^2}{245} + \tfrac{356f^3}{5145} + \tfrac{32f^4}{735}\right)x^2 + \left(\tfrac{8f^2}{105} + \tfrac{8f^3}{105} + \tfrac{16f^4}{315}\right)x^4$$

$$A^{0,1}_{1,1} = A^{0,-1}_{1,1} = -\left(1 + \tfrac{4f}{3} + \tfrac{226f^2}{375} + \tfrac{44f^3}{525} - \tfrac{27f^4}{6125}\right)x - \left(\tfrac{64f^2}{375} + \tfrac{128f^3}{875} + \tfrac{192f^4}{6125}\right)x^3$$

$$A_{1,3}^{0,1} = A_{3,1}^{0,-1} = \left(\frac{8f^2}{125} + \frac{16f^3}{525} + \frac{72f^4}{6125}\right)x + \left(\frac{16f^2}{375} + \frac{32f^3}{875} + \frac{48f^4}{6125}\right)x^3$$

$$A_{3,1}^{0,1} = A_{1,3}^{0,-1} = \left(\frac{64f^2}{375} + \frac{64f^3}{525} + \frac{512f^4}{23625}\right)x + \left(\frac{16f^2}{375} + \frac{32f^3}{875} + \frac{464f^4}{70875}\right)x^3$$

$$A_{5,1}^{0,1} = A_{1,5}^{0,-1} = \frac{256f^4x}{33075} - \frac{256f^4x^3}{19845}$$

$$A_{3,3}^{0,1} = A_{3,3}^{0,-1} = -\left(\frac{12f^2}{125} + \frac{8f^3}{75} + \frac{668f^4}{23625}\right)x - \left(\frac{4f^2}{375} + \frac{8f^3}{875} + \frac{116f^4}{70875}\right)x^3$$

$$A_{5,3}^{0,1} = A_{3,5}^{0,-1} = -\frac{64f^4x}{33075} + \frac{64f^4x^3}{19845}$$

Quadrupole term ($\ell = 2$):

$$A_{0,0}^{2,0} = \frac{32f}{945} + \frac{32f^2}{4725}$$

$$A_{2,0}^{2,0} = A_{0,2}^{0,0} = \frac{388}{315} + \frac{1804f}{1323} + \frac{29068f^2}{46305} + \frac{4f^3}{35}$$

$$A_{4,0}^{2,0} = A_{0,4}^{0,0} = \frac{f}{105} + \frac{f^2}{8575}$$

$$A_{2,2}^{2,0} = \frac{64}{441} + \frac{73210f}{64827} + \frac{56606f^2}{64827} + \frac{64f^3}{343} - \left(\frac{32}{147} + \frac{12316f}{7203} + \frac{3132f^2}{2401} + \frac{96f^3}{343}\right)x^2$$

$$A_{4,2}^{2,0} = A_{2,4}^{0,0} = -\left(\frac{4}{245} + \frac{320f}{7203} + \frac{1124f^2}{36015} + \frac{16f^3}{1715}\right) + \left(\frac{4}{49} + \frac{914f}{7203} + \frac{992f^2}{7203} + \frac{16f^3}{343}\right)x^2$$

$$A_{4,4}^{2,0} = -\left(\frac{32f}{2401} + \frac{2456f^2}{180075} + \frac{128f^3}{11319}\right) + \left(\frac{272f}{2401} + \frac{796f^2}{7203} + \frac{1088f^3}{11319}\right)x^2 - \left(\frac{16f}{147} + \frac{16f^2}{147} + \frac{64f^3}{693}\right)x^4$$

$$A_{1,1}^{2,1} = A_{1,1}^{0,-1} = \left(\frac{11}{15} + \frac{299f}{525} + \frac{59f^2}{525} - \frac{3f^3}{1225}\right)x + \left(\frac{128f}{525} + \frac{832f^2}{3675} + \frac{64f^3}{1225}\right)x^3$$

$$A_{1,3}^{2,1} = A_{3,1}^{0,-1} = -\left(\frac{1}{5} + \frac{37f}{175} + \frac{397f^2}{3675} + \frac{33f^3}{1225}\right)x - \left(\frac{32f}{525} + \frac{208f^2}{3675} + \frac{16f^3}{1225}\right)x^3$$

$$A_{3,1}^{2,1} = A_{1,3}^{0,-1} = -\left(\frac{2}{5} + \frac{38f}{75} + \frac{1054f^2}{4725} + \frac{1858f^3}{51975}\right)x - \left(\frac{32f}{525} + \frac{16f^2}{225} + \frac{2768f^3}{155925}\right)x^3$$

$$A_{5,1}^{2,1} = A_{1,5}^{0,-1} = \left(\frac{16f^2}{945} - \frac{848f^3}{72765}\right)x + \left(\frac{16f^2}{2205} + \frac{976f^3}{43659}\right)x^3$$

$$A_{3,3}^{2,1} = A_{3,3}^{0,-1} = \left(\frac{8f}{175} + \frac{68f^2}{675} + \frac{604f^3}{17325}\right)x + \left(\frac{8f}{525} + \frac{4f^2}{225} + \frac{692f^3}{155925}\right)x^3$$

$$A^{2,1}_{5,3} = A^{0,-1}_{3,5} = -\left(\frac{68f^2}{6615} + \frac{76f^3}{24255}\right)x - \left(\frac{4f^2}{2205} + \frac{244f^3}{43659}\right)x^3$$

Octopole term ($\ell = 4$):

$$A^{4,0}_{2,0} = A^{0,0}_{0,2} = \frac{32f}{25725}$$

$$A^{4,0}_{4,0} = A^{0,0}_{0,4} = \frac{218}{1225} + \frac{1028f}{8575} + \frac{6f^2}{175}$$

$$A^{4,0}_{2,2} = \frac{2624}{12005} + \frac{6752f}{36015} + \frac{72f^2}{1715} + \left(\frac{5248}{12005} + \frac{4544f}{12005} + \frac{144f^2}{1715}\right)x^2$$

$$A^{4,0}_{4,2} = A^{0,0}_{2,4} = \frac{32}{2401} + \frac{84582f}{660275} + \frac{192f^2}{3773} - \left(\frac{48}{2401} + \frac{5056f}{26411} + \frac{288f^2}{3773}\right)x^2$$

$$A^{4,0}_{4,4} = \frac{436}{60025} + \frac{128f}{60025} + \frac{15696f^2}{1226225} - \left(\frac{436}{12005} + \frac{356f}{12005} + \frac{15696f^2}{245245}\right)x^2 + \left(\frac{8}{245} + \frac{8f}{245} + \frac{288f^2}{5005}\right)x^4$$

$$A^{4,1}_{1,1} = A^{0,-1}_{1,1} = -\left(\frac{116}{875} + \frac{24f}{385} + \frac{612f^2}{67375}\right)x - \left(\frac{64}{875} + \frac{6144f}{67375} + \frac{1728f^2}{67375}\right)x^3$$

$$A^{4,1}_{1,3} = A^{0,-1}_{3,1} = \left(\frac{59}{875} + \frac{174f}{2695} + \frac{1143f^2}{67375}\right)x + \left(\frac{16}{875} + \frac{1536f}{67375} + \frac{432f^2}{67375}\right)x^3$$

$$A^{4,1}_{3,1} = A^{0,-1}_{1,3} = \left(\frac{46}{375} + \frac{512f}{5775} + \frac{4546f^2}{375375}\right)x + \left(\frac{16}{875} + \frac{64f}{1375} + \frac{2448f^2}{125125}\right)x^3$$

$$A^{4,1}_{5,1} = A^{0,-1}_{1,5} = -\left(\frac{1}{21} + \frac{38f}{1155} - \frac{743f^2}{525525}\right)x - \left(\frac{32f}{2695} + \frac{432f^2}{35035}\right)x^3$$

$$A^{4,1}_{3,3} = A^{0,-1}_{3,3} = -\left(\frac{26}{875} + \frac{8f}{275} + \frac{4094f^2}{375375}\right)x - \left(\frac{4}{875} + \frac{16f}{1375} + \frac{612f^2}{125125}\right)x^3$$

$$A^{4,1}_{5,3} = A^{0,-1}_{3,5} = \left(\frac{8f}{2695} + \frac{3308f^2}{525525}\right)x + \left(\frac{8f}{2695} + \frac{108f^2}{35035}\right)x^3$$

$\ell = 6$ term:

$$A^{6,0}_{4,2} = A^{0,0}_{2,4} = \frac{4}{231} + \frac{4f}{539} + \left(\frac{16}{231} + \frac{16f}{539}\right)x^2$$

$$A^{6,0}_{4,4} = \frac{64f}{8085} + \frac{32fx^2}{8085} - \frac{64fx^4}{3465}$$

$$A^{6,1}_{1,1} = A^{0,-1}_{1,1} = \left(\tfrac{32}{1925} + \tfrac{96f}{13475}\right) x + \left(\tfrac{64}{5775} + \tfrac{64f}{13475}\right) x^3$$

$$A^{6,1}_{1,3} = A^{0,-1}_{3,1} = -\left(\tfrac{8}{1925} + \tfrac{24f}{13475}\right) x - \left(\tfrac{16}{5775} + \tfrac{16f}{13475}\right) x^3$$

$$A^{6,1}_{3,1} = A^{0,-1}_{1,3} = -\left(\tfrac{736}{51975} - \tfrac{16f}{51975}\right) x - \left(\tfrac{208}{17325} + \tfrac{1648f}{155925}\right) x^3$$

$$A^{6,1}_{5,1} = A^{0,-1}_{1,5} = \left(\tfrac{67}{10395} + \tfrac{197f}{72765}\right) x + \left(\tfrac{16}{3465} + \tfrac{688f}{218295}\right) x^3$$

$$A^{6,1}_{3,3} = A^{0,-1}_{3,3} = \left(\tfrac{62}{7425} + \tfrac{82f}{17325}\right) x + \left(\tfrac{52}{17325} + \tfrac{412f}{155925}\right) x^3$$

$$A^{6,1}_{5,3} = A^{0,-1}_{3,5} = -\left(\tfrac{23}{10395} + \tfrac{31f}{24255}\right) x - \left(\tfrac{4}{3465} + \tfrac{172f}{218295}\right) x^3$$

$\ell = 8$ term:

$$A^{8,0}_{4,4} = \tfrac{2}{2145} + \tfrac{16x^2}{2145} + \tfrac{16x^4}{6435}$$

$$A^{8,1}_{3,1} = A^{0,-1}_{1,3} = \tfrac{32x}{19305} + \tfrac{128x^3}{57915}$$

$$A^{8,1}_{5,1} = A^{0,-1}_{1,5} = -\tfrac{4x}{19305} - \tfrac{16x^3}{57915}$$

$$A^{8,1}_{3,3} = A^{0,-1}_{3,3} = -\tfrac{8x}{19305} - \tfrac{32x^3}{57915}$$

$$A^{8,1}_{5,3} = A^{0,-1}_{3,5} = \tfrac{x}{19305} + \tfrac{4x^3}{57915}$$

Bibliography

Anderson, L., et al. 2012, MNRAS, 427, 3435

—. 2014, MNRAS, 439, 83

Baldauf, T., Seljak, U., & Senatore, L. 2011, JCAP, 4, 6

Bernardeau, F., Colombi, S., Gaztañaga, E., & Scoccimarro, R. 2002, Phys. Rep., 367, 1

Blake, C., et al. 2011a, MNRAS, 418, 1707

—. 2011b, MNRAS, 415, 2876

Bond, J. R., & Efstathiou, G. 1984, ApJ, 285, 45

Bouchet, F. R., Colombi, S., Hivon, E., & Juszkiewicz, R. 1995, A&A, 296, 575

Carron, J. 2011, ApJ, 738, 86

Carron, J., & Neyrinck, M. C. 2012, ApJ, 750, 28

Cole, S., et al. 2005, MNRAS, 362, 505

BIBLIOGRAPHY

Coles, P., & Jones, B. 1991, MNRAS, 248, 1

Crocce, M., Pueblas, S., & Scoccimarro, R. 2006, MNRAS, 373, 369

Crocce, M., & Scoccimarro, R. 2006, Phys. Rev. D, 73, 063519

—. 2008a, Phys. Rev. D, 77, 023533

—. 2008b, Phys. Rev. D, 77, 023533

de Bernardis, P., Ade, P. A. R., Bock, J. J., Bond, J. R., et al. 2000, Nature, 404, 955

de la Torre, S., et al. 2013, A&A, 557, A54

Dodelson, S. 2003, Modern cosmology

Eisenstein, D. J., Seo, H.-J., Sirko, E., & Spergel, D. N. 2007, ApJ, 664, 675

Eisenstein, D. J., Zehavi, I., Hogg, D. W., Scoccimarro, R., et al. 2005, ApJ, 633, 560

Falck, B. L., Neyrinck, M. C., Aragon-Calvo, M. A., Lavaux, G., & Szalay, A. S. 2012, ApJ, 745, 17

Fry, J. N. 1984, ApJ, 279, 499

Fry, J. N., & Gaztanaga, E. 1994, ApJ, 425, 1

Gaztañaga, E., Norberg, P., Baugh, C. M., & Croton, D. J. 2005, MNRAS, 364, 620

BIBLIOGRAPHY

Gil-Marín, H., Wagner, C., Fragkoudi, F., Jimenez, R., & Verde, L. 2012, JCAP, 2, 47

Grinstein, B., & Wise, M. B. 1987, ApJ, 320, 448

Hamilton, A. J. S. 1992, ApJ, 385, L5

Hamilton, A. J. S. 1998, in Astrophysics and Space Science Library, Vol. 231, The Evolving Universe, ed. D. Hamilton, 185

Hamilton, A. J. S., & Culhane, M. 1996, MNRAS, 278, 73

Hanany, S., Ade, P., Balbi, A., Bock, J., et al. 2000, ApJLetters, 545, L5

Jain, B., & Bertschinger, E. 1994, ApJ, 431, 495

Jenkins, A., et al. 1998, ApJ, 499, 20

Jeong, D., & Komatsu, E. 2009, ApJ, 703, 1230

Kaiser, N. 1986, MNRAS, 222, 323

—. 1987, MNRAS, 227, 1

Kitaura, F.-S., & Angulo, R. E. 2012, MNRAS, 425, 2443

Kofman, L., Bertschinger, E., Gelb, J. M., Nusser, A., & Dekel, A. 1994, ApJ, 420, 44

Komatsu, E., et al. 2009, ApJS, 180, 330

BIBLIOGRAPHY

Lavaux, G., Mohayaee, R., Colombi, S., Tully, R. B., Bernardeau, F., & Silk, J. 2008, MNRAS, 383, 1292

Lewis, A., Challinor, A., & Lasenby, A. 2000, ApJ, 538, 473

Liddle, A. R., & Lyth, D. H. 2000, Cosmological Inflation and Large-Scale Structure

Marín, F. 2011, ApJ, 737, 97

Marín, F. A., et al. 2013, MNRAS, 432, 2654

Matsubara, T. 2008a, Phys. Rev. D, 78, 083519

—. 2008b, Phys. Rev. D, 77, 063530

McBride, C. K., Connolly, A. J., Gardner, J. P., Scranton, R., Newman, J. A., Scoccimarro, R., Zehavi, I., & Schneider, D. P. 2011a, ApJ, 726, 13

McBride, C. K., Connolly, A. J., Gardner, J. P., Scranton, R., Scoccimarro, R., Berlind, A. A., Marín, F., & Schneider, D. P. 2011b, ApJ, 739, 85

Mehrem, R., Londergan, J. T., & Macfarlane, M. H. 1991, Journal of Physics A: Mathematical and General, 24, 1435

Mehta, K. T., Seo, H.-J., Eckel, J., Eisenstein, D. J., Metchnik, M., Pinto, P., & Xu, X. 2011, ApJ, 734, 94

Mohayaee, R., Mathis, H., Colombi, S., & Silk, J. 2006, MNRAS, 365, 939

BIBLIOGRAPHY

Neyrinck, M. C. 2011, ApJ, 742, 91

Neyrinck, M. C., Szapudi, I., & Szalay, A. S. 2009a, ApJL, 698, L90

—. 2009b, ApJ, 698, L90

Nichol, R. C., et al. 2006, MNRAS, 368, 1507

Nishimichi, T., Kayo, I., Hikage, C., Yahata, K., Taruya, A., Jing, Y. P., Sheth, R. K., & Suto, Y. 2007, PASJ, 59, 93

Padmanabhan, N., Schlegel, D. J., Seljak, U., Makarov, A., et al. 2007, MNRAS, 378, 852

Padmanabhan, N., & White, M. 2009, Phys. Rev. D, 80, 063508

Padmanabhan, N., Xu, X., Eisenstein, D. J., Scalzo, R., Cuesta, A. J., Mehta, K. T., & Kazin, E. 2012, MNRAS, 427, 2132

Parkinson, D., et al. 2012, Phys. Rev. D, 86, 103518

Peebles, P. J. E. 1980, The large-scale structure of the universe

Peebles, P. J. E., & Yu, J. T. 1970, ApJ, 162, 815

Percival, W. J., Cole, S., Eisenstein, D. J., Nichol, R. C., Peacock, J. A., Pope, A. C., & Szalay, A. S. 2007, MNRAS, 381, 1053

Percival, W. J., et al. 2010, MNRAS, 401, 2148

BIBLIOGRAPHY

Perlmutter, S., Aldering, G., Goldhaber, G., Knop, R. A., The Supernova Cosmology Project, et al. 1999, ApJ, 517, 565

Reid, B. A., et al. 2012, MNRAS, 426, 2719

Riess, A. G., Filippenko, A. V., Challis, P., Clocchiatti, A., et al. 1998, AJ, 116, 1009

Rubin, V. C., & Ford, Jr., W. K. 1970, ApJ, 159, 379

Scoccimarro, R. 1998, MNRAS, 299, 1097

Scoccimarro, R. 2001, in Annals of the New York Academy of Sciences, Vol. 927, The Onset of Nonlinearity in Cosmology, ed. J. N. Fry, J. R. Buchler, & H. Kandrup, 13–23

Scoccimarro, R., Colombi, S., Fry, J. N., Frieman, J. A., Hivon, E., & Melott, A. 1998, ApJ, 496, 586

Scoccimarro, R., & Couchman, H. M. P. 2001, MNRAS, 325, 1312

Scoccimarro, R., Couchman, H. M. P., & Frieman, J. A. 1999, ApJ, 517, 531

Scoccimarro, R., Feldman, H. A., Fry, J. N., & Frieman, J. A. 2001, ApJ, 546, 652

Scoccimarro, R., & Frieman, J. 1996, ApJS, 105, 37

Sefusatti, E., & Komatsu, E. 2007, Phys. Rev. D, 76, 083004

Seljak, U., & Zaldarriaga, M. 1996, ApJ, 469, 437

BIBLIOGRAPHY

Seo, H.-J., & Eisenstein, D. J. 2003, ApJ, 598, 720

Seo, H.-J., Siegel, E. R., Eisenstein, D. J., & White, M. 2008, ApJ, 686, 13

Seo, H.-J., et al. 2012, ApJ, 761, 13

Shandarin, S. F., & Zeldovich, Y. B. 1989, Reviews of Modern Physics, 61, 185

Sherwin, B. D., & Zaldarriaga, M. 2012, Phys. Rev. D, 85, 103523

Silk, J. 1968, ApJ, 151, 459

Smith, R. E., Scoccimarro, R., & Sheth, R. K. 2008, Phys. Rev. D, 77, 043525

Sunyaev, R. A., & Zel'dovich, Y. B. 1970, APSS, 9, 368

Taruya, A., Nishimichi, T., & Saito, S. 2010, Phys. Rev. D, 82, 063522

Taruya, A., Nishimichi, T., Saito, S., & Hiramatsu, T. 2009, Phys. Rev. D, 80, 123503

Tassev, S., & Zaldarriaga, M. 2012, JCAP, 10, 6

Tegmark, M., et al. 2006, Phys. Rev. D, 74, 123507

Tian, H. J., Neyrinck, M. C., Budavári, T., & Szalay, A. S. 2011, ApJ, 728, 34

Valageas, P. 2011, A&A, 526, A67

Verde, L., et al. 2002, MNRAS, 335, 432

BIBLIOGRAPHY

Vishniac, E. T. 1983, MNRAS, 203, 345

Zel'dovich, Y. B. 1970, Astron. Astrophys., 5, 84

Zwicky, F. 1937, ApJ, 86, 217

Vita

Nuala McCullagh was born on April 29, 1985 in Summit, NJ. She grew up in Hyde Park, a neighborhood in Chicago, IL. From 2003-2007, she attended the University of Pennsylvania, where she worked with Dr. Mark Devlin. She graduated *summa cum laude* with a B.A. in Physics, and a minor in Mathematics. She enrolled in the Physics and Astronomy Ph.D. program at Johns Hopkins University in 2008, where she worked with Dr. Charles Bennett until 2010. She then began her work with Dr. Alex Szalay on theoretical and numerical modeling of large-scale structure. In October 2014 she will take up a postdoctoral position in the Institute for Computational Cosmology at Durham University in England.